UNIVERSITÀ
DEGLI STUDI
FIRENZE

DOTTORATO DI RICERCA IN SCIENZE CHIMICHE

CICLO XXIX

COORDINATORE Prof. PIERO BAGLIONI

NUOVE PROSPETTIVE NELLA SINTESI E FUNZIONALIZZAZIONE DI MATERIALI MESOPOROSI NANOSTRUTTURATI DI SILICIO E LORO APPLICAZIONE NELLA CATALISI

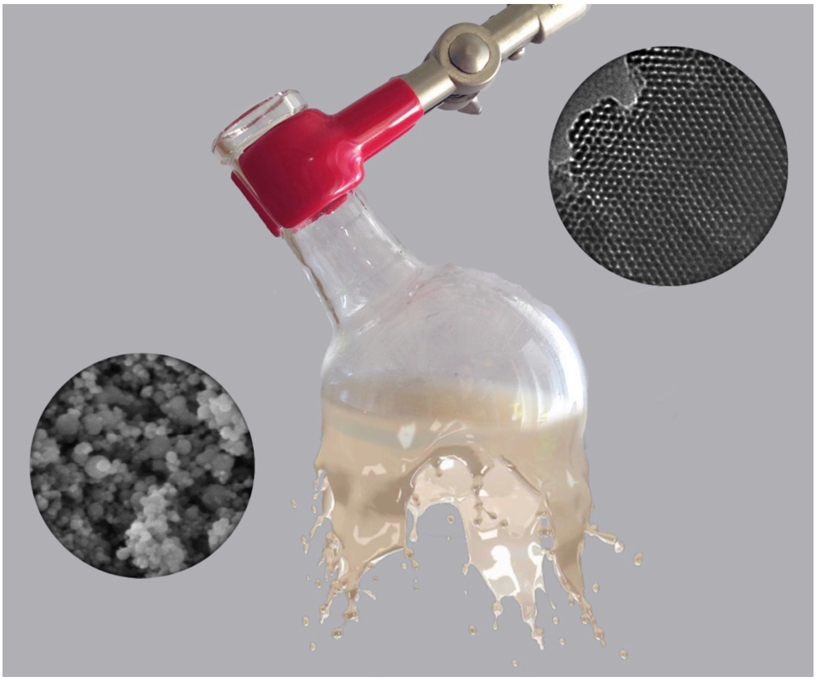

Dottorando
Dott. Jorge Tovar Rodríguez

Tutore
Prof. Emiliano Fratini

UNIVERSITÀ
DEGLI STUDI
FIRENZE

DOTTORATO DI RICERCA IN SCIENZE CHIMICHE

CICLO XXIX

COORDINATORE Prof. PIERO BAGLIONI

NEW PERSPECTIVES ON THE SYNTHESIS AND FUNCTIONALIZATION OF NANOSTRUCTURED MESOPOROUS SILICON-BASED MATERIALS AND THEIR USE IN CATALYSIS

NUOVE PROSPETTIVE NELLA SINTESI E FUNZIONALIZZAZIONE DI MATERIALI MESOPOROSI NANOSTRUTTURATI DI SILICIO E LORO APPLICAZIONE NELLA CATALISI

Settore Scientifico Disciplinare CHIM/02

Dottorando
Dott. Jorge Tovar Rodríguez

Tutore
Prof. Emiliano Fratini

Coordinatore
Prof. Piero Baglioni

Anni 2014/2017

Contents

Part I

Abstract

Abstract

The aim of the present thesis work is the development of methodologies for the synthesis and functionalization of nanostructured silicon-based mesoporous materials. By coupling innovative synthesis approaches such as microwaves irradiation for thermal activation, ultrasounds for micromixing and the use of a non-conventional silicon source as building block, the overall synthesis time was reduced, the dispersion of the functionalizing agent was enhanced and a synthesis procedure for the preparation of hexagonally ordered silica sieves using a geothermal waste was disclosed. The time reduction and the decrease in the number of synthesis steps poses significant advantages from an economic point of view and favors the development of green chemical processes. The prepared materials were used as catalytic supports to produce sustainable energy sources and to valorize glycerol as potential raw material for the synthesis of value-added chemical reagents.

Cerium promoted mesoporous silica supports were prepared following two different methodologies: I) Direct *in situ* modification of hexagonally ordered MCM-41 under solvothermal synthesis, using a cationic surfactant as structure-directing agent and II) Post synthesis cerium oxide grafting of mesoporous SBA-15, prepared with a non-ionic triblock poloxamer and a swelling agent to control the pore diameter and surface area.

Direct synthesis of MCM-41 silica sieves was achieved by ultrasound-assisted solvothermal synthesis to obtain highly dispersed Ce into the silica framework. The explored Ce/Si molar ratios for the synthesis of the mesoporous materials ranged from 0.02 to 0.08. Microwave irradiation applied by a coaxial antenna was used for thermal activation to reduce the overall hydrothermal synthesis time. The hexagonal ordering of the materials decreased by Ce direct incorporation in the structure. As the amount of Ce/Si increased, two different mechanisms of Ce incorporation were observed: isomorphic substitution and ceria particles deposition outside the silica framework. The mesoporous sieves were used as catalytic supports for a Ni active phase (10 wt.% of metal loading). Their catalytic activity was evaluated in the ethanol steam reforming reaction to produce hydrogen. The new catalysts featured complete ethanol conversion, and higher H_2 selectivity (compared to the same Ni catalyst over bare silica) ranging from 60 to 65%. The main product distribution was not dependent on Ce content, these materials did not exhibit catalyst deactivation after 6h on stream and were selective towards H_2, CO_2, CO and CH_4 as sole reaction products.

Post synthesis modification of silicon-based SBA-15 was performed over large pore mesoporous sieves, prepared by solvothermal methodology using

a non-ionic triblock copolymer as structure directing agent. By modifying the 1,3,5 trimethylbenze/Pluronic 123 mass ratio and the solvothermal ageing temperature, it is possible to obtain hexagonally ordered mesophases in the pore size interval from 4 to 20nm. Selected samples of variable pore diameter were selected as support for the preparation of CeO_2/SiO_2 composites. The surface grafting methodology enabled the formation of well-dispersed ceria particles that do not match the pore size and therefore do not produce pore blocking.

Finally, a green methodology for the preparation of mesoporous silica was developed using a non-conventional silicon-source. A series of template-based mesoporous molecular silicas were prepared using a geothermal waste. Microwaves irradiation was provided by the coaxial applicator for thermal activation. All prepared materials feature hexagonal ordering, narrow pore size distribution and high surface areas (over $500m^2/g$). By changing the parameters of the solvothermal synthesis, it is possible to tune the ordering and textural properties of the mesophases and reduce the reaction time. These materials were successfully used as a Zn catalytic support for the solventless MW-assisted conversion of glycerol to glycerol carbonate.

The promising results obtained by the presented synthesis approaches enable the realistic projection of other types of green chemical processes that may include the design of semi-batch, continuous reaction schemes and the simultaneous use of ultrasounds and microwaves. The enhanced hydrothermal synthesis here discussed could also be extended to the preparation of other type of mesoporous solids in soft-template approaches with a pertinent selection of microwave-responsive solvents or reaction media.

Part II

Introduction

Chapter 1

Theoretical background

Ordered mesoporous molecular sieves are a versatile class of template-based materials that can find multiple applications in catalysis[90], fuel cell applications[50], gas[22,23] or heavy metals adsorption[43], as stationary phases in chromatographic applications[73] and as matrices for drug delivery[119]. In particular, silicon-based mesophases[59,121] exhibit hexagonal ordering, high surface area and a narrow pore size distribution[60], but they are seldom used as such since they lack any catalytic activity or surface functionality.

These applications are feasible due to the possibility of tailoring their textural properties by an adequate control of the reaction parameters involved in the surfactant-based solvothermal methodology. The synthesis of mesoporous materials is a complex area where fundamental aspects for materials design converge. The traditional synthesis approach assisted by amphiphilic molecules involves three well-defined steps: I) An initial stage for nucleation, ageing, growth and crystallization of precursors in hydrothermal synthesis; II) Surfactant removal at high temperature levels to provide porosity and III) Post-synthesis functionalization or grafting. In every step, the synthesis parameters may be modified to obtain a material with the adequate and desired characteristics.

Nevertheless, to fulfill the growing requirement of sustainable and eco-friendly processes, it is mandatory to develop new methodologies and synthesis routes that involve a reduction in the synthesis steps, elimination of wastes, minimum generation of pollutants and a more efficient use of the resources employed in the preparation of mesoporous sieves. This will invariably result in an overall reduction of the production cost.

To address these drawbacks, hydrothermal synthesis can be enhanced by the incorporation of non-conventional technologies to obtain the desired mesoporous structures. In this sense, the acoustic cavitation produced by ultrasound (US) has demonstrated to improve the nucleation and crystallization steps during the solvothermal synthesis of template-based micro and mesoporous materials such as zeolites or zeotypes[4]. Still, the sonochemical synthesis of metal-modified mesoporous silica is scarcely reported. On the other hand, microwave assisted chemistry (MW) is a useful tool for thermal activation to reduce the long synthesis time typically required to produce ordered nanostructured materials[98]. Depending on the dielectric properties of the reaction medium and solvent, it is possible to achieve shorter synthesis times by a more effective heating and temperature profile produced by MW irradiation. Nonetheless, most of the commercially available reactors for MW-synthesis have a traditional closed-box configuration, which makes them particularly unsuitable for scaling-up and may limit their operative conditions or coupling with other techniques[68].

The solvothermal synthesis parameters can be modified and adapted to achieve costs and energy consumption reductions. Therefore, the study and optimization of these parameters remains a key factor in the innovation and development of new synthesis routes. Recent research efforts are focused on novel approaches, production of surfactants from renewable sources, obtainment of low environmental impact silica sources and raw materials, with the purpose of reducing the toxicity associated to their synthesis and enabling the production of mesoporous materials at an industrial scale.

The main interest and widespread applications of silicon-based mesoporous materials is found in catalysis. To modify their catalytic properties, it is possible to incorporate different atoms into the hexagonal structure. Several examples can be found in the literature concerning the structural modification of mesoporous silica, either by direct or post-synthesis functionalization, in order to provide catalytic activity[95].

Ordered mesoporous silica has been modified with transition metals and has been used for oxidative catalysis[36], acid-base catalysis[3] photocatalysis or as catalytic support for a metal active site[83,87,96] Therefore, it is important to develop synthesis methodologies that make possible structure modification and tailoring its characteristics in a minimum number of steps while preserving the high surface area, ordering and other features of the parent material. Because of the high versatility for the synthesis and modification of mesoporous silica, it is possible to obtain very specific silicates or composite materials with *ad hoc* structural and surface properties. More specific applications are oriented towards the generation of value-added chemicals and alternative energy sources to reduce the dependence on non-renewable fossil fuels.

In recent years, the interest placed on hydrogen production for fuel cells application has increased considerably. Hydrogen is primarily used in the chemical industry, but it has been foreseen as the main energy vector of the near future. Several hydrocarbons have been used as feedstock for reforming reactions to produce hydrogen[32,40] whereas the usage of a renewable feedstock such as ethanol[69] or glycerol[42] is always preferred due to their lower environmental impact.

The cleavage of fatty acids to produce esters that can be used as biodiesels by transesterification reactions produces a significant amount of glycerol as by-product. Through catalyzed selective reactions, it is possible to valorize the glut of glycerol that results from biodiesel production since it represents a good candidate as raw material to produce value-added chemicals and monomers[93]. Glycerol obtained as by-product of fatty acids transesterification to produce biodiesel has a huge potential to become an important feedstock and raw material to obtain chemical intermediates since it can undergo oxidation, dehydration, carboxylation, esterification, hydrogenolysis, and dehydration reactions, depending on the catalytic active phase or support.

Outline

The main scope of the present research subject is the development of novel synthesis strategies for the preparation of silicon-based mesoporous materials to be used as catalytic supports.

In the first part of this work, a synthesis methodology for the incorporation of cerium into the hexagonal framework of mesoporous silica is presented. By means of acoustic cavitation, it is possible to obtain a hexagonally ordered material with good Ce dispersion. The solvothermal synthesis time was then reduced by using microwaves irradiation for thermal activation. The prepared materials were used as catalytic support for a Ni active phase in the ethanol steam reforming reaction to produce hydrogen. The new catalyst presented complete ethanol conversion, did not show catalyst deactivation after 6h on stream and were selective towards hydrogen, CO, CO_2 and CH_4 as main reaction products.

Based on the catalytic results obtained for the Ni/Ce-MCM-41 materials, a series of nanocomposites with a Ce/Si molar ratio of 0.04 were prepared by post-synthesis grafting of mesoporous silica of different pore size. To tune the pore size and surface area of mesoporous SBA-15, trimethylbenzene was used as micelle expander and a triblock copolymer Pluronic P123 was used as structure directing agent. By modifying the amount of swelling agent, it is possible to tailor the pore size in the interval from 4 to 20nm.

Selected samples were used for post-synthesis grafting with cerium oxide, using ultrasounds acoustic cavitation for Ce dispersion. These materials will be used as Ni catalytic supports for the ESR reaction. The product distribution and Ni dispersion on the catalytic support will be discussed in terms of the pore size and surface area.

In the last part of this work, a novel and green methodology for the preparation of mesoporous silica using a non-conventional silicon source is disclosed. Solvothermal synthesis was enhanced and the overall synthesis time was reduced by means of a coaxial applicator for *in situ* microwaves irradiation. By controlling the synthesis parameters, it is possible to tune the hexagonal ordering, surface area and textural properties of mesoporous silica prepared using a cationic surfactant as structure directing agent. These materials were tested as Zn catalytic supports for the solventless carbonylation of glycerol.

1.1 Amphiphilic Molecules

Amphiphilic molecules are compounds that possess both hydrophilic and lipophilic properties. The duality of this behavior renders them capable of modifying the interface between two liquids or one liquid phase and a gaseous phase. Structurally, the lipophilic portion of the amphiphilic molecule consists of a long (saturated or unsaturated) hydrocarbon chain, while the hydrophilic head can have a specific polarity.

Considering the nature of the polarity of the hydrophilic group, these surface-active molecules can be classified as nonionic, cationic, anionic or zwitterionic surfactants. Hereafter, the terms surfactant and amphiphile will be used as exchangeable synonyms to refer to this specific type of molecules, which can find broad applications as detergents[115], as chemical additives in the food industry[58], in the remediation of contaminated soils[72], as corrosion inhibitors[70] and as building blocks for the synthesis of ordered nanostructured mesoporous materials[28,106]. Figure 1.1 shows some recurring examples of surfactants.

Nonionic surfactants consist generally of a hydrophilic poly(ethylene oxide) chain, often called ethoxylates, connected with a hydrophobic alkyl chain, and are generally used in cleaning applications, like surfactants based on polyoxyethylene alkyl ethers (figure 1.1a). Other type of non-ionic commercial surfactants are the poloxamer family, which are tri-block copolymers used for the synthesis of mesoporous silicates[71]. These symmetric copolymers typically consist of a central chain of polypropylene oxide (PPO), flanked by two side chains

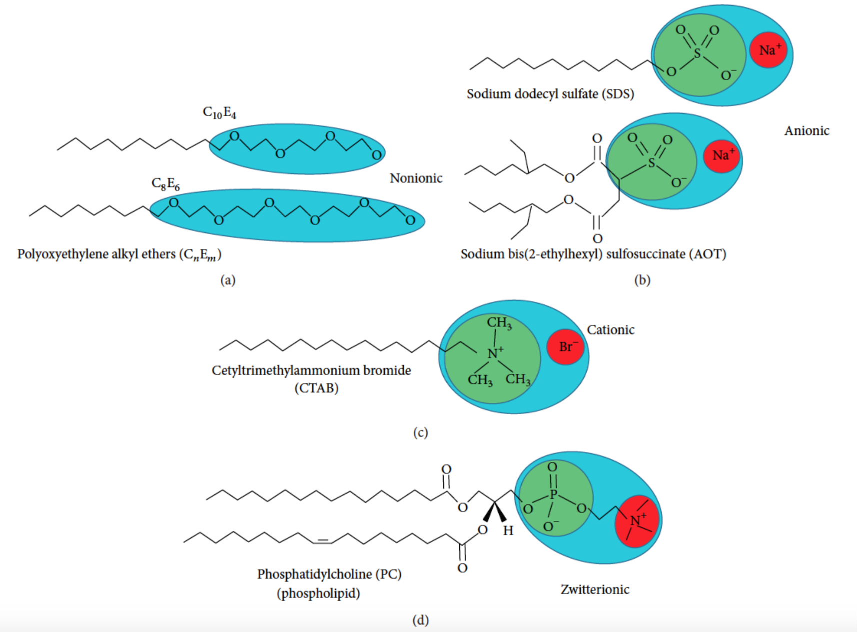

Figure 1.1: A few examples of common nonionic (a), anionic (b), cationic (c), and zwitterionic (d) amphiphilic molecules (Reprinted from Ref.[67])

of polyethylene oxide (PEO). Their nominal chemical formula is $HO(CH_2CH_2O)_x(CH_2CH(CH_3)O)_y(CH_2CH_2O)_zH$, where x, y and z denote the chain length for each portion of the molecule.

On the other hand, anionic surfactants are negatively charged headgroups and positively charged counterions, namely $K^{[+]}$, $Na^{[+]}$ or $NH^{[4+]}$. Carboxylate, sulfate, sulphonate, and phosphate for instance are the commonly used polar groups for capillary electrophoresis applications[1].

Cationic surfactants consist of positively charged headgroups such as a quaternary ammonium and a halide ion as a counterion. For example, cetyltrimethylammonium bromide (CTAB) is one of the most employed cationic amphiphiles for the preparation of ordered mesophases[60] (figure 1.1c). Zwitterionic amphiphilic molecules bear headgroups which can possess both a positive and negative charge, as it happens, for example, in the vesicle-forming phospholipid phosphatidylcholine (figure 1.1d). These interesting type of surfactant is usually employed in binary or ternary mixtures and their dual behavior is dependent on parameters like pH, temperature and concentration[44,91].

In aqueous dissolutions, the amphiphiles polar headgroup interacts with the water while the nonpolar lipophilic chain will migrate above the interface (either in the air or in a nonpolar liquid), because of their amphiphilicity.

In this case the disruption of the cohesive energy at the interface favors a microphase separation between the selective solvent and the dispersed phase of the amphiphile with the formation of many smaller closed interfaces or micelles-like aggregates. These thermodynamically controlled interactions may be regarded as the base of their self-assembly behavior[74].

1.1.1 Amphiphiles soft-interactions in solvent media

To fully explain the nature of self-assembly, the involved driving forces, the kinetics and the most important parameters controlling the spontaneous arrangement of amphiphilic molecules, several attempts have been made and a good deal of review articles have been published to address these issues[21,92,94]. Concerning the driving forces, Table 1.1 compares the energy bonding and interaction type of the most recurrent. Even though self-assembly molecular binding is weak in principle, these soft interactions will collectively produce an overall effect that is strong enough to hold different amphiphile molecules together as well as to ensure their stability in solution[26]. Moreover, the degree of strength of the involved interactions makes the structure more flexible enabling the system to withstand minor perturbations while preserving the reversibility of the self-assembled structure. Aside from the strength, the distance at which these interactions occur is of significance as well. For instance, the hydrogen bonding energy found in CH_4 is in the order of 10kJ/mol and can be considered significant in the range from a few to hundreds of Armstrong, whereas the ionic bond energy in LiF is 1004.1kJ/mol acting in a distance of 2Å.

Bonding and interaction type	Energy, kJ/mol
Covalent bond	100 –400
Ion-ion/ion-dipole/dipole-dipole	200 –300 / 50 –200 / 5 –50
Hydrogen bond	4 –120
Cation-n interaction	5 –80
pi - *pi* interaction	0 –50
van der Waals interaction	<5kJ/mol

Table 1.1: Nature and strength of the main noncovalent interaction involved in amphiphiles self-assembly[67]

The main weak noncovalent forces mediating in the self-assembly of amphiphilic molecules are hydrogen bonding, hydrophobic effects, electrostatic interaction, and the van der Waals forces.

Hydrogen bondings are ionic associations between an electronegative atom and a hydrogen atom attached to a second, relatively electronegative atom. In water solvent, nonbonding electrons are the H-bond acceptors and the hydrogen atoms are the H-bond donors. Hydrogen bonding interactions exhibit greater thermoreversibility and specificity, allowing reversible attachment of guest molecules. In addition, the strength of hydrogen bonding associations is further tunable via variation of structural parameters and molecular design of the hydrogen bonding sites[62].

Along with the hydrogen bond, the hydrophobic effect is the second main driving force of amphiphile self-assembly into various supramolecular structures. The hydrophobic effect, which is the tendency for oil and water to segregate, is important in diverse phenomena, from the cleaning of laundry, to the creation of micro-emulsions to make new materials, to the assembly of proteins into functional complexes. This effect is multifaceted depending on whether hydrophobic molecules are individually hydrated or driven to assemble into larger structures[18]. This is an important implication when selecting adequate co-solvents for the preparation of stable micellar emulsions using surfactants. Stability in solution of the amphiphiles within the aggregates is a result of both the hydration of the hydrophilic polar headgroups and the insertion of the hydrophobic apolar tails in the solvent. The first is an enthalpy gain in solvation due to hydrogen bond formation while the second, called the hydrophobic effect which is a gain in entropy of the bulk water[67].

In the case of cationic and anionic surfactants, the balance between electrostatic interactions and van der Waals forces plays a significant role and can be explained by the Derjaguin, Landau, Vervey, and Overbeek (DLVO) theory of charged colloids[77] which can in turn be extended to the case of charged amphiphilic molecules. In the case of surface active molecules that do not bear a permanent dipole, such as block copolymers, van der Waals along with H-bonding interactions are the dominant forces. The polarity of the surfactant is an important parameter to consider when amphiphilic molecules are used as structure directing agents since this can determine the selection of a suitable set of ionic or metallic precursors.

1.1.2 Micellar formation, packing factors and micellar morphology

The conditions for surfactant self-assembly are thus governed by the concentration of the amphiphiles in solution, the concentration at which the first aggregation process occurs being known as the critical micelle concentration (CMC) and subsequent aggregation occurring at the critical aggregation concentration (CAC)[80].

These aforementioned parameters are relevant for the design of a synthesis methodology. Therefore, for a specific amphiphilic molecule a minimum surfactant concentration (CMC), will be required for the spontaneous formation of micellar aggregates. For the case of charged systems, electrostatic interactions mediate further bulk and particle aggregation that occurs above the CAC value[48]. This is of particular interest since bulkier aggregates behave differently than single micelles by modifying the rheology of the system. The CAC depends on the type of surfactant and the polarity of the reaction medium[5].

Although the process of micelle formation can be described with accuracy using a molecular thermodynamic theoretical approach in which the free Gibbs energy can be expressed as the sum of at least six different energy contributions[74], in its simplest form, a valid approximation for the free Gibbs energy of spontaneous formation of micellar aggregates is given in terms of the CMC:

$$\Delta G^{\circ}{}_{M} \approx RT * ln(CMC) \tag{1.1}$$

Where R is the ideal gas constant. Most commonly used surfactants have a CMC of less than 0.01M. For instance, hexadecyltrimethylammonium bromide (CTABr) has a CMC of 0.92mM in the temperature interval from 20 to 25°C.

The shape and size of given micellar aggregates depend on the molecular geometry of its component surfactant molecules and the solution conditions such as surfactant concentration, temperature, pH, and ionic strength[67]. Concerning the micellar morphology[21], the structure of the aggregate can be predicted from the dimensionless critical packing parameter $\mathrm{C_{pp}}$:

$$C_{pp} = \frac{V_0}{A_{mic} * l_c} \tag{1.2}$$

Where $\mathrm{V_0}$ is the effective volume occupied by hydrophobic chains in the aggregate core, $\mathrm{l_c}$ is the maximum effective length (critical chain length), and $\mathrm{A_{mic}}$ is the effective hydrophilic headgroup surface area at the aggregate-solution interface. With the increment of Cpp value, the structure of aggregates can be spherical (for Cpp $<$ 1/3), cylindrical (1/3 $<$ Cpp $<$ 1/2), and lamellar (Cpp = 1). For 1/2 $<$ Cpp $<$ 1, vesicles are generally generated, which correspond to spherical (or ellipsoidal) closed amphiphile bilayer structures with an internal cavity containing the dispersion solution. A summary of the aggregate structures that can be predicted from the critical packing parameter is reported in figure 1.2

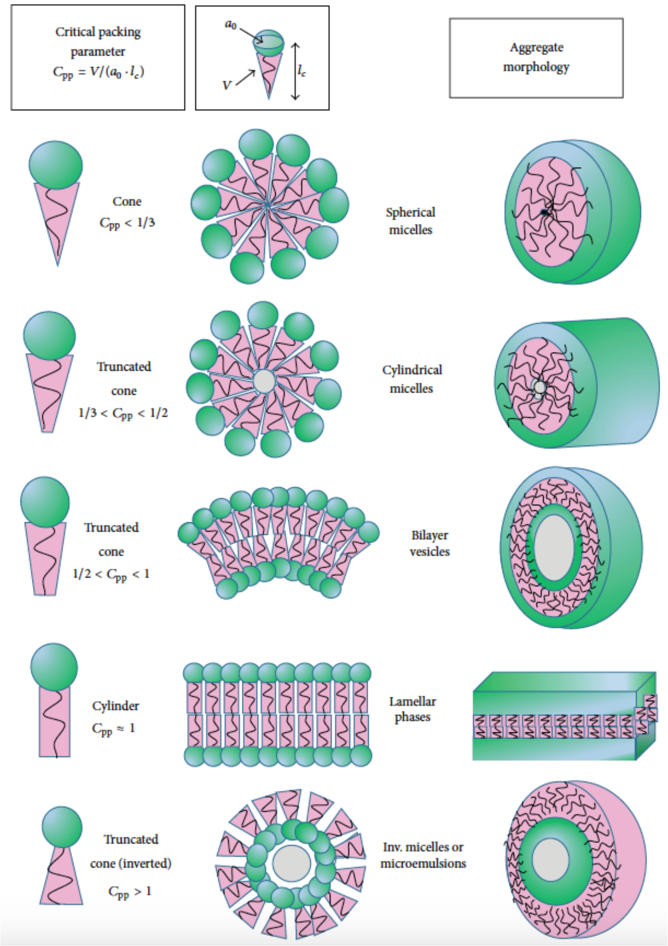

Figure 1.2: Amphiphile shape factors and summary of the aggregate structures that can be predicted from the critical packing parameter (Reprinted from Lombardo et. al.[67])

1.2 Soft-template synthesis of nanostructured materials

Solvothermal processing is a well-known method to synthesize materials with very specific features such as shape, size, distribution and ordering, and it has been widely used to prepare metallic oxides, nanoparticles and nanostructures. The use of amphiphiles as structure directing agents has been an effective bottom-up approach to form supramolecular architectures given their self-assembly properties.

The synthesis of a silicon-based family of structures M41S, using a cationic surfactant molecule as structure-directing agent was initially reported by researchers at Mobil Corporation[8,59]. By means of a quaternary ammine as template under solvothermal conditions and the use of optional co-surfactants, the dimensions of the mesoporous silica network can be tailored in various ranges. Figure 1.3 shows the proposed reaction mechanism for the silica frameworks.

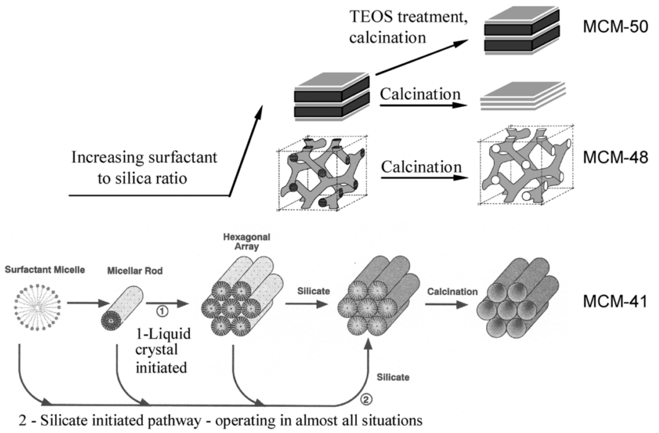

Figure 1.3: Liquid crystal template mechanism of formation pathways and its further additions, for the M41S family of mesoporous silicas (Reprinted from Kresge et. al.[60])

Later, the use of poloxamers, such as amphiphilic triblock copolymers was investigated[121]. These materials were named SBA-X (Santa Barbara Amorphous), where X is a number corresponding to a specific pore structure and surfactant. For example, SBA-15, the most extensively studied mesoporous silica, has hexagonally ordered cylindrical pores synthesized using Pluronic P123 as a surfactant template. Under strong acidic conditions, non-ionic surfactant templated mesoporous silica SBA can be synthesized with highly ordered hexagonal mesophases and higher hydrothermal stability.

In general, the synthesis methodology for the preparation of mesoporous silica using amphiphiles as templates has well-defined steps: A colloidal solution system is composed of the surfactant micelles dispersed in an aqueous solution. When an appropriate silicon precursor is added to the surfactant solution it interacts with the micelles and hydrolyzes while a silica network is gradually formed. Finally, the resulting framework is heated and the surfactant is decomposed or oxidized under oxygen or air atmospheres, while the porous silica network remains. The whole process is also referred to as "$soft - templating$", given the use of an organic material as structure directing agent, or $cooperative\ self - assembly$ as the amphiphile and the silica precursor assembly are simultaneous[67].

The self-assembly synthesis has been expanded and is not limited exclusively to hexagonally ordered structures, but also to various types of mesoporous materials. The soft-template approach yields nanostructured silicas with tunable structure and properties, by a combination of synthesis parameters, such as nature of the surfactant, pH, solvothermal treatment temperature, use of co-solvents, and template removal protocol. Figure 1.4 shows a schematic representation of the possible structures obtained by block copolymers as structure directing agents.

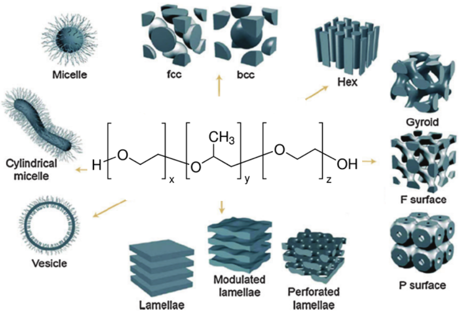

Figure 1.4: Phase diagram of the various morphologies formed by triblock copolymers, including spherical and cylindrical micelles, vesicles, spheres with face centered cubic, body centered cubic structures, hexagonally packed cylinders, bycontinous gyroid, F and P surfaces and lamella (Adapted from Deng et. al.[28])

1.3 Structural modification and functionalization of mesoporous silica

Despite the distinctive characteristics that ordered mesoporous sieves exhibit, silicon-based materials are rarely employed as catalysts or as adsorbents since silica lacks of any active sites of interest and their surface charge density is not significant. Therefore, to improve the catalytic properties of mesoporous silica, it is necessary to incorporate active phases either by direct synthesis (co-condensation) or by grafting (post-synthesis modification) to achieve a desired functionality[19,95,104].

Concerning the direct synthesis modification, it is possible to find reports on the successful incorporation of several transition metals (Fe, Co, Ni, Mo, Mn)[51,85,89,118], alkali earth mteals (Mg[102]), alkali metals (Na, Cs) and noble metals (Pt, Pd, Ru, Rh)[20,32,37,109,123], metallic oxides (TiO_2, VO_x, ZrO_2, Fe_2O_3, Cr_2O_3,)[30,56,114,117], rare earths (La, Ce)[12,63,116], substitution of trivalent heteroatoms to provide acidity (Al^{3+}, B^{3+}, Y^{3+}, Fe^{3+})[54,99], both within the hexagonal structure and on its surface[10,46].

On the other hand, organic molecules functionalization is performed by co-condensation and post-synthesis grafting as well. Regarding the direct approach, mesoporous silica has been functionalized with thiol[105], ammine[47], carboxylic acid groups[112] or aliphatic and aromatic carbon moieties, and they have been successfully used for heavy metals removal[78] and chromatographic applications[88]. Post synthesis grafting has been achieved by adsorption of guest molecules, surface grafting and covalently attached alkyl silanes[11].

The design of materials with specific applications like the ones mentioned before requires an adequate control of the surface chemistry and structure geometry, mainly in micro and mesoscale. Thus, the modification and control of all the synthesis parameters involved will result in a catalytic or adsorbent support with the desired properties. Figure 1.5 shows a schematic representation of the possible reaction strategies and types of functionalization to introduce novel functions in mesoporous materials.

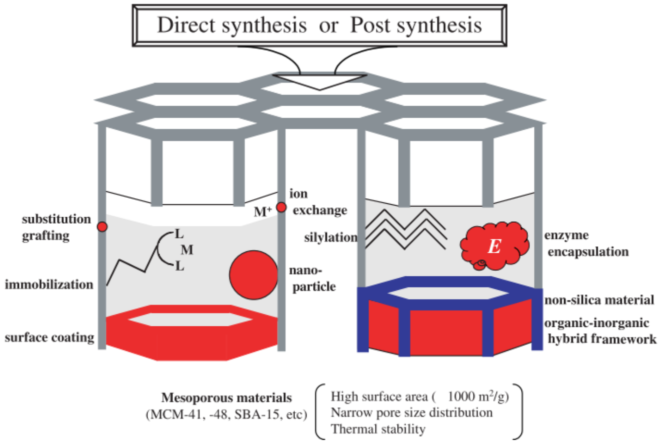

Figure 1.5: Direct and post-synthesis types of mesoporous silica functionalization (Reprinted from Taguchi et. al.[95])

1.4 Catalytic evaluation of modified mesoporous silicas

1.4.1 Steam reforming of ethanol to produce hydrogen

The growing interest in hydrogen as an alternative energy carrier is based on its non-polluting nature and several noble metals such as Ru, Pd, Ag[16], Pt[81] and Rh[37] have demonstrated to be adequate catalysts for the ethanol steam reforming reaction. However, their widespread use still faces the high costs and limited availability associated to the materials based on noble metals. To address this issue, transition metal catalysts like Ni and Cu[12] may result of more practical application due to their high availability and lower economic cost. Nonetheless, Ni catalysts tend to deactivate swiftly, as they seem to promote ethylene, acetaldehyde and acetone formation, all of which have been identified as coke precursors[103]. For this reason, it is necessary to design catalytic supports that enhance the synergy between the active phase and the support to improve hydrogen yields, inhibit carbon deposition and avoid metallic sintering at high operative temperatures.

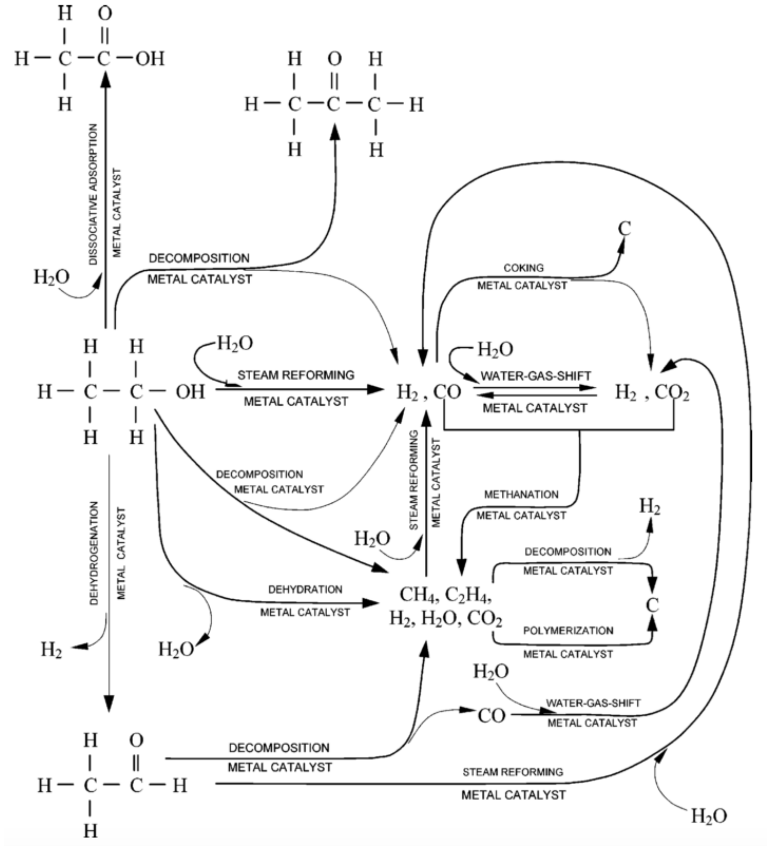

Figure 1.6: Reaction pathways that can occur during ethanol steam reforming over metal catalysts (Reprinted from Haryanto et. al.[42])

Some of the most important reactions occurring when ethanol is reformed by steam are the ethanol dehydrogenation reaction to produce acetaldehyde, methane formation, followed by steam reforming of hydrocarbons to produce H_2 and CO_2, along with the water gas shift reaction (WGS), and a complex network of side-reactions. Figure 1.6 features some of the possible reaction pathways for the ESR reaction over metal catalysts[42]. Thus, the surface chemistry of the catalyst is very important since it can affect the product selectivity. An acidic support can lead to ethanol dehydration, coke formation and coke surface deposition. To avoid catalyst deactivation, basic or neutral oxides and supports are preferred since they do not catalyze hydrocarbon dehydration reactions and could promote the oxidation of deposited coke, increasing the catalyst stability and selectivity towards H_2. Catalysts based on metallic active sites along with redox supports have shown an enhanced catalytic activity and selectivity compared to acid supports (Al modified structures or pure Al_2O_3[17]).

Given its oxygen vacancies and oxygen storage capacity[14], cerium oxide and cerium-based composite materials are a well-known and preferred catalyst for oxidation of reagents. For instance, cerium modified mesoporous silicas have been successfully employed for the selective oxidation of organic compounds[2], exhibiting negligible pore diffusion resistance, higher selectivity, improved catalytic activity and good catalyst reusability[113], compared to Ce over amorphous SiO_2, CeO_2 or other cerium-based supports. Furthermore, Ce-promoted hexagonally ordered materials have also been used as catalytic supports for metallic active phases in the reforming reactions of hydrocarbons to produce hydrogen, since their oxidation capacity makes them less prone to carbon deposition, carbon poisoning and consequent catalyst deactivation[31,40,64].

1.4.2 Carbonylation of glycerol to produce glycerol carbonate.

The always growing concern in finding suitable energy sources to reduce the oil dependency for economic and environmental reasons has seen a growing interest in biodiesel production. This is associated by stoichiometry to an inherent glycerol production as undesired product. Given its low toxicity and biodegradability, glycerol has the potential to be both an excellent renewable solvent in modern chemical processes and a versatile building block in biorefineries. Figure 1.7 exemplifies the use of glycerol as starting material for the synthesis of value-added chemicals[24]. These potential applications may be made easier and more convenient as adequate catalyst are developed for a specific synthesis route or application.

In this context, the synthesis of glycerol carbonate (glycerin carbonate or 4-hydroxymethyl-2-oxo-1,3-dioxolane) to revalorize glycerol crudes is an effective alternative. Glycerol carbonate is a promising molecule bearing both a hydroxyl group and a 2-oxo-1,3-dioxolane group which provides it with adequate reactivity for the preparation of other added-value compounds. Glycerol carbonate can find several applications as solvent or curing agent, for cosmetics synthesis, in lithium batteries, as liquid membrane for gas separation and as blowing agent[93].

Among the most frequent synthesis routes, glycerol carbonylation is

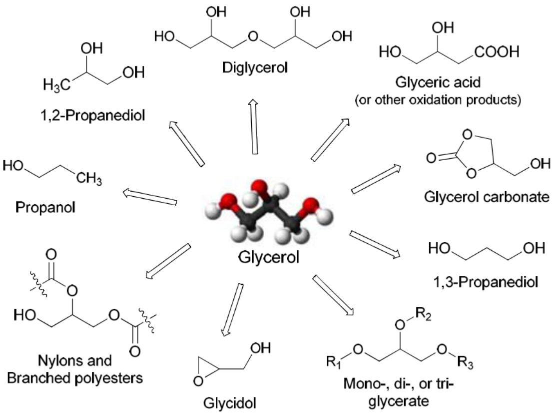

Figure 1.7: Glycerol derivatives and potential applications (Reprinted from Cintas et. al.[24])

typically run with carbonylating agents, by reaction of glycerol with CO_2 under supercritical conditions, dimethyl carbonate[79], and urea[57], under milder reaction conditions. Among these reagents, urea is a particularly attractive carbonylating agent due to the mild reaction conditions and high selectivity. Therefore, developing a heterogeneous catalyst for this process has strategic and environmental benefits[13].

1.5 Green synthesis of mesoporous silica

1.5.1 Microwave and ultrasound assisted chemistry

Nowadays microwave assisted chemistry is an invaluable tool within chemistry research. The number of applications of microwaves is increasing since substantial reduction of the reaction time is often achieved. Selective heating, superheating, thermal runaway capability, solvent-free reactions and other remarkable advantages make this methodology very attractive[68]. Microwave-enhanced chemistry is based on the efficient heating of materials by microwave dielectric heating effects. For this reason, thermal activation by means of microwaves irradiation could be a promising alternative to conventional heating.

One of the main drawbacks of solvothermal synthesis is the large reaction time required to form ordered structures. In this sense, microwave-assisted synthesis has shown great benefits due to a reduction of crystallization times, lower energy consumption and more uniform temperature profiles. There are several reports of hydrothermal synthesis assisted by microwaves for MCM-41 type materials where crystallization times were reduced from 24 to 1 hour or less[107] and a reduction from 48 hours to periods of 1 to 2 hours for SBA-15[76], if compared to the hydrothermal treatment time originally reported[59,121]. This lowering of the time and associated cost would make more porous materials readily available for many chemical, environmental, and biological applications. Further, microwave syntheses have often proven to create more uniform (defect-free) products than conventional hydrothermal synthesis[98].

Nonetheless, the most typical and commercially available oven-type microwave reactors feature a closed-box geometry[29,39]. As a consequence, the shape and the size of the load are important because the microwave source and the oven cavity itself react differently to loads of the same volume placed in different vessels or in different positions. Moreover, hot spots, arching and unpredictable explosions of closed reactors are not rare events, particularly when looking for new reaction pathways. The use of metal sensors and other devices with metal parts is severely limited by the high amplitude of the microwave electric field at a resonance peak. The impossibility of direct manual, visual and/or instrumental access to the reaction vessel is another limitation for the operator. The use of auxiliary devices or glassware directly connected to the reactor, such as a reflux condenser or a water cooling bath is not straightforward and many other useful tools must be placed outside the oven[68]. Hence, a suitable reactor configuration for versatile operative conditions and efficient microwave application is still a challenge.

Ultrasounds on the other hand, are an effective and cheap tool that can improve the nucleation step, reduce the induction periods and enhance the dispersion of surfactants, silicon precursors or co-solvents that are involved in the synthesis of mesoporous solids. Application of ultrasound can influence the size and morphology of the crystals, crystallization rate and the crystallinity of another type of surfactant-based material, such as zeolites and zeotypes[4].

The use and application of ultrasounds in the preparation of emulsions and dispersion of surfactants in the synthesis of mesoporous structures using surface-active agents as templates, could result in considerable improvements in the textural properties of the particles, compared to magnetic stirring or stirring produced by propellers. The micromixing effect produced by acoustic cavitation can result in better dispersion and more uniform distribution of the synthesis colloid.

1.5.2 Alternative silica sources for the synthesis of micro and mesoporous materials

Regarding the silicon precursors, a high number of reported synthesis methodologies are based on the use of synthetic silica sources like silicon alkoxides or soluble silicates (sodium silicate, colloidal and fumed silica). However, these synthetic sources are normally obtained from toxic reagents and require energy intensive and expensive synthesis procedures or high pH values to reach the desired level of polymerization, in the case of soluble silica.

Considering these facts, the most logical option is to incorporate recycled silica sources from industrial wastes. Inexpensive coal fly ash can be used as raw material and silica source for the synthesis of MCM-41; Using ethyl acetate as mild acid hydrolyzer a highly ordered material can be obtained. Rice husk has also been used as silica source. An increasing application of rice husk as fuel generates rice husk ash, which is washed with acids or bases using thermal treatments at high temperatures to remove impurities and unburned carbon amounts. The main disadvantage of both silica sources is the pre-treatment required to either purify or mineralize the silicon source using acids and bases ranging from medium to strong conditions[33].

A very promising source of silica can be found in geothermal waters and geothermal wastes, arising from precipitation of solids that are found in the vapors used for energy generation. Still, the number of publications reporting its use as raw material is limited[6,7], which could be due to the restricted number of operative geothermal fields in the world. The accumulation of silica in geothermal power plants represents a serious problem because it limits the thermal efficiency of the global process and produces pipelines blockage when it is condensed in high quantities. Since most of this condensed silica must be disposed of and is not further treated or employed, it represents a potential starting material for the industrial production of mesoporous silicon-based materials.

Part III

Materials and Methods

Chapter 2

Experimental Methodology

2.1 Ultrasound and microwave assisted synthesis of cerium-modified mesoporous silica

Cerium isomorphic substitution in mesoporous silica was achieved in a direct synthesis approach. The structure-directing agent was the cationic amphiphilic molecule hexadecyltrimethylammonium bromide (CTABr, $CH_3(CH_2)_{15}N(Br)(CH_3)_3$ Sigma-Aldrich). Ammonium hydroxide was used as mineralizing agent (30% NH_3 wt/v Sigma); cerium nitrate was used as Ce precursor ($Ce(NO_3)_3{\bullet}6(H_2O)$, Sigma-Aldrich) and tetraethyl orthosilicate was used as silicon source (TEOS, $CH_3CH_2O)_4Si$ Sigma-Aldrich). All reagents were used without further purification. A series of materials with the following molar composition of the synthesis colloid were prepared:

$1.0(CH_3CH_2O)_4Si$: $xCe(NO_3)_3{\bullet}6H_2O$: $0.3CTABr$: $18NH_3$: $160H_2O$; x = 0.02, 0.04, 0.06 and 0.08.

The materials were named xCeMCM-41, where x indicates the Ce/Si nominal molar ratio. The MCM-41 hydrothermal synthesis reported by Kresge et al.[8], was modified by adding a Ce precursor and using ultrasound during the nucleation step to increase Ce dispersion in the mesoporous structure. Microwave assisted hydrothermal synthesis was carried out in a stainless steel high-pressure reactor using a coaxial antenna for in-situ MW application. Details concerning the design, construction of the reactor[34] and the technical specifications for the MW applicator can be found elsewhere[68]. Conventional hydrothermal synthesis was performed in a Teflon-lined stainless steel reactor using a heating mantle.

In a typical batch, 2.85g of CTABr were dissolved in 50ml of deionized water and 33.5ml of NH_4OH. The temperature of the solution was kept at 45°C and under vigorous stirring (500rpm) for 0.5h. A second solution containing the required amount of cerium nitrate dissolved in 12.5ml of deionized water was mixed with the surfactant solution. Then, 4.56ml of TEOS were added dropwise to the mixture. The colloidal solution was treated with ultrasounds for another 2.5h (Frequency 40kHz), before being aged for an additional 4h. The samples were treated hydrothermally at 100°C and autogenous pressure for 24h (conventional synthesis) and 1h (for MW-assisted synthesis). The precipitated product was separated by centrifugation, washed with deionized water and dried at 80°C overnight. The obtained powder was annealed at 550°C and atmospheric pressure under static air for 4h to remove the surfactant and to yield a porous material.

2.2 Synthesis of Ni catalyst over Ce-MCM-41

Ni catalysts were prepared by wet impregnation method to achieve a total loading of 10wt % of Ni over the catalyst, using a solution of $Ni(NO_3)_2 \bullet 6H_2O$ (Aldrich). The resulting solids were dried at room temperature for 24h and then calcined at 550°C for 2h. Hereafter, the catalysts containing 10wt % of Ni are referred to as Ni/xCeMCM-41, using the aforementioned values for x depending on the nominal amount of Ce molar load in the support.

2.3 Ethanol Steam reforming over Ni/Ce-MCM-41

The ethanol steam reforming reaction was performed in a reactor with 10mm of internal diameter and a length of 50cm. A catalyst sample of 50mg was placed in the reactor in a powder quartz bed. A thermocouple K-type was placed near the catalytic bed to control the reaction temperature. The catalysts were reduced in-situ at 550°C for 2 hours with a Hydrogen flow of 50cm^3/min and a heating rate of 10°C/min. After reduction, the system was flushed with 50cm^3/min of Argon for 15 min. The reforming reactions were performed at 450 and 500°C under atmospheric pressure. A liquid flow containing water and ethanol in a molar ratio of 3:1 was evaporated in argon and was fed at a rate of 0.01cm^3/min. The ethanol and water streams were mixed and adjusted with pure argon until a total flow of 100cm^3/min was measured. The composition of the reactor effluent was analyzed by two gas chromatographs Clarus 580 (Perkin Elmer): one equipped with a Q-plot capillary column and an FID detector, was used for the separation of CH_4, C_2H_5OH, CH_3CHO, C_2H_4, CH_3COOH, and CH_3COCH_3. The other gas chromatograph was equipped with a Molsieve capillary column and a TCD detector for the analysis of H_2, CO, CH_4, CO_2 and C_2H_4.

2.4 Synthesis of mesoporous SBA-15

Mesoporous silica, SBA-15 was synthesized by hydrothermal treatment, following the approach originally reported elsewhere[120]. The structure-directing agent used was a commercial triblock copolymer based on poly(ethylene glycol)-poly(propylene glycol)-poly(ethylene glycol) (Pluronic P123 $HO(CH_2CH_2O)_{20}(CH_2CH(CH_3)O)_{70}(CH_2CH_2O)_{20}H$ average molecular weight = 5800 Sigma Aldrich) and tetraethyl orthosilicate (TEOS 98% Sigma) was used as silicon source. In a typical synthesis, 6g of P123 were dissolved in 45.02ml of deionized water and 150ml of hydrochloric acid 2M, at a temperature of 35°C and vigorous stirring until complete surfactant dissolution was reached. Then, 13.8ml of TEOS were added dropwise to the solution. The synthesis colloid was aged under these conditions for 24 hours and was then transferred to a Teflon bottle to be hydrothermally treated at 80°C for another 24h. The precipitated product was centrifuged, washed with deionized water until the pH of the eluent was neutral and dried overnight at 80°C. The obtained white powder was annealed at 550°C in static air for 4h to remove the surfactant molecule.

2.5 Synthesis of large pore SBA-15

To produce SBA-15 solids with variable pore size and surface area, a swelling agent was employed during the micellar formation and nucleation step to tailor the micelle size. A derivative of benzene with three methyl substituents was used as organic co-surfactant molecule: 1,3,5 trimethylbenzene (Mesitylene, Sigma-Aldrich). In a typical synthesis, 6.0 g of Pluronic P123 were dissolved in 156ml of deionized water. Then, 28.4ml of concentrated HCl (28% Sigma) were added to the surfactant solution and it was vigorously stirred (400rpm) and kept at 35°C. The appropriate amount of swelling agent was added dropwise to form an emulsion with 0.08, 0.16, 0.33 and 1.0 as TMB/P123 mass ratios. After two hours of stirring 12.9g of tetraethylorthosilicate were added dropwise to the micellar emulsion, which was then aged for 24h at the same temperature. Solvothermal synthesis was then performed at 80°C and autogenous pressure for another 24h. Once the reaction was completed, a white solid was separated by centrifugation, washed with deionized water until neutral pH was reached and dried at 80°C overnight. To remove the occluded organic species, all materials were annealed at 550°C under static air for 4 hours to yield a porous material.

To study the effect of the solvothermal synthesis temperature, SBA-15 molecular sieves with the highest swelling agent/surfactant ratio were hydrothermally treated at two higher temperature levels (110 and 120°C) and autogenous pressure. After hydrothermal treatment, the white precipitate was separated following the previously detailed protocol to remove the soft template. The synthesized large pore samples were designated as LP-SBA-15-X-Y, where X indicates the temperature selected for the hydrothermal treatment and Y the TMB/P123 mass ratio. Selected samples with pore sizes ranging from 5 to 20nm were used for the preparation of CeO_2-SiO_2 nanocomposite catalytic supports.

2.6 CeO_2-LP-SBA15 mesoporous silica composite materials

Cerium promoted mesoporous catalytic supports with a Ce/Si molar ratio of 0.04 (for a 10% CeO_2 in the final material) were prepared by precipitation method using $Ce(NO_3)_3{\bullet}6H_2O$ as Ce precursor and tetramethylammonium hydroxide (TMAOH) as precipitating agent additive. In a typical synthesis, 1.0g of dried mesoporous silica was put in contact with 0.29g of Ce precursor previously dissolved in 5ml of deionized water. Then, an adequate amount of TMAOH ($Ce(NO_3)_3$:TMAOH, molar ratio 1:1) was added to catalyze the formation of insoluble Ce(III) hydroxide while the solution was kept under vigorous stirring. This mixture was transferred to an ultrasonic bath to be treated sonically for 1h (40kHz) to further disperse the Ce species along the silica matrix. The solvent excess was removed by centrifugation and the resulting powder was dried overnight at 80°C and annealed at 550°C under static air to obtain a CeO_2/SiO_2 composite material.

2.7 A geothermal silica waste as non-conventional Si precursor

A sample of inorganic geothermal waste was received from a geothermal field in the region of Los Azufres MX. This material was obtained from the condensation of the high-pressure vapors coming from a hot spring used in the electricity generation process. To adequate this sample to be used as a raw material for the synthesis of silica mesophases, the geothermal waste underwent the following treatment: 100g of this material were put in contact with 500ml of a HCl solution (0.5M) for 1h under atmospheric conditions and 300rpm of magnetic stirring. This aqueous dispersion was separated by centrifugation (3.5krpm) and the precipitated solid was dried at 90°C for 24h. Afterwards, the geothermal waste was crushed and sieved to yield a maximum particle size of 105μm (using a MESH grid, 150 nominal size). Then, the sample was calcined to remove any organic impurities at 550°C for 4h. This material is referred hereafter as geothermal waste (GeoWaste).

2.8 Synthesis of hexagonally ordered mesoporous geothermal silica

To yield a hexagonally ordered mesoporous material, the geothermal industrial waste (GeoWaste) was used as building block in a soft-template preparation approach. The green synthesis of the materials was performed by hydrothermal treatment, using a microwave-assisted Teflon-lined stainless steel high-pressure reactor. The microwaves were applied *in situ* by means of an innovative microwave coaxial antenna, which allows direct microwave application within the reaction system. The details concerning the construction and operation of the high-pressure reactor can be found elsewhere[34]. On the other hand, conventional hydrothermal synthesis was performed using a heating mantle. The structure-directing agent used was the quaternary cationic ammine hexadecyltrimethylammonium bromide (CTABr, Sigma-Aldrich) and ammonium hydroxide (NH_3 30% wt/v Sigma-Aldrich) was used as mineralizing agent. The molar composition for the synthesis colloid was as follows:

$1.0SiO_2 : 0.30CTABr : 20NH_3 : 210H_2O$.

In a typical synthesis, 1.43g of CTABr were dissolved in 25ml of deionized water. Then, 0.8g of geothermal waste (GeoWaste) were mixed with 17.5ml of NH_4OH and 14.13ml of deionized water. Both solutions were kept under vigorous stirring. Once the surfactant was completely dissolved, the GeoWaste emulsion was added dropwise and it was kept at 45°C for 24 or 48h, to allow silica polymerization around the micellar formations. Then, this mixture was transferred to the high-pressure reactor to be hydrothermally treated at 100°C for 2, 4 or 6 hours. For comparative purposes, a conventional silicon source (tetraethylortosilicate, TEOS $SiC_8H_{20}O_4$, 99% Sigma-Aldrich) was used for the preparation of hexagonally ordered mesoporous MCM-41 under hydrothermal treatment at 100°C and 24h, according to a previously reported methodology[35]. For the preparation of MCM-41, the aforementioned molar ratios were used:

$1.0(CH_3CH_2O)_4Si : 0.30CTABr : 20NH_3 : 210H_2O$.

After hydrothermal treatment was completed, all samples were washed with deionized water several times, dried overnight at 80°C and calcined at 550°C under static air to remove the surfactant occluded within the mesopores.

2.9 Synthesis of MGS-supported Zn catalyst

Selected mesoporous geothermal silica samples were used as support for a ZnO catalyst (5% ZnO in the final material). In a typical synthesis, 300mg of a Zn precursor ($ZnSO_4 \bullet 7H_2O$ Sigma-Aldrich) were dissolved in 7.5ml of methanol. Then, 1.45g of dried mesoporous solid was put in contact with the Zn precursor solution. This mixture was transferred to an ultrasonic bath operating at a maximum frequency of 40kHz and was sonically dispersed for 30 minutes. The solvent excess was removed using a rotovapor. The resulting powder was dried overnight at 80°C and annealed at 550°C under static air to yield the oxidized Zn form.

2.10 Solventless MW-assisted carbonylation of glycerol

The catalytic activity of mesoporous geothermal silica supported Zn (ZnO/MGS) catalysts was evaluated in the carbonylation of glycerol, using glycerol and carbamide as reagents ($C_3H_8O_3$ 98% Sigma-Aldrich; $CO(NH_2)_2$, 99% Sigma-Aldrich) and microwaves irradiation for thermal activation. A green solventless approach was developed to carry out the carbonylation reactions: The reaction was performed in an ordinary glassware triple-neck round-bottom flask, possessing an open ending tube to place an innovative microwave applicator for in-situ microwaves irradiation. The coaxial applicator ending was placed at three quarters of the total length of the flask inner tube and a choke section was used to minimize reflected power towards the MW source[68]. The source of microwave consisted in a magnetron oscillator equipped with forward and reflected power indicators (SAIREM, Mod. GMP 03 K/SM), operating at a maximum of 300 W of continuous MW irradiation power at a frequency of 2.45 GHz. A Faraday cage-type enclosure was made by covering the flask with a largely sieved metallic continuous grid, allowing visual control of the reaction and a safety operation by eliminating non-absorbed radiation escaping the boundaries of the reactor. For a reflux set-up, a condenser was mounted on the middle neck, leaving one neck for a thermometric well and another one for sampling. A typical reaction was performed by loading 0.2mol of glycerol, a stoichiometric amount of urea (1:1 glycerol to urea molar ratio) and 0.92g of dried catalyst (for a 5% wt of catalysts, referred to the glycerol mass). The reaction was performed at 160°C and samples were taken after 15, 30, 60, 90 and 120 minutes.

To determine glycerol conversion and product distribution, product samples were analyzed by means of gas chromatography coupled with mass spectrometry (GC-MS). An Agilent 6850 gas chromatograph, equipped with a split/splitless injector, was used in combination with an Agilent 5975c mass spectrometer. A CTC CombiPAL autosampler was employed for the liquid injections. A sample of 1μl was injected in split mode (split ratio 1:100) into the gas chromatograph. Then, the inlet liner (4mm internal diameter) was held at 250°C and the injection was performed in split mode. The column was kept under a constant helium flow rate of 1.2 mL/min). Compounds were then separated in a high polarity column (DB-FFAP; 60m length; consisting of terephtalic acid-modified carbowax stationary phase; 0.25 mm inner diameter; 0.5 m coating) using the following temperature program: 5 min at 150°C, 10°C/min up to 230°C held for 30 min (53 min total runtime). The temperature of the transfer line was set at 240°C. After GC separation, glycerol carbonate and glycerol were ionized in positive extracted ion (EI). The MS acquisition was performed in total ion chromatography (TIC) which allowed for the identification of glycerol and glycerol carbonate, whereas extracted ion was implemented for quantitative purposes by monitoring m/z of 61, 87, 43 and 45 (100ms dwell time). For the calibration of the instrumental response, 1 ml of a 200ppm primary standard solution of glycerol and glycerol carbonate were injected in 2 mL of methanol.

Chapter 3

Main characterization techniques

3.1 X-ray scattering techniques

X-ray scattering is a structural characterization tool that has impacted diverse fields of study. It is unique in its ability to examine materials in real time and under realistic sample environments, enabling to understand morphology at nanometer and angstrom length scales using complementary small and wide angle X-ray scattering (SAXS, WAXS), respectively[65]. X-ray scattering provides information concerning both form factor and structure factor, making possible the use of correlation functions which may be used to determine particle size, size distribution, shape, and organization into hierarchical structures.

3.1.1 Bragg Scattering

The so-called Bragg condition occurs when radiation, with wavelength comparable to atomic spacings, is scattered in a specular fashion by the atoms of a crystalline system, and undergoes constructive interference. Figure 3.1 shows a graphical representation of Bragg scattering:

For an ordered solid, the waves are scattered from lattice planes separated by the interplanar distance d. When the scattered waves interfere constructively, they remain in phase since the difference between the path lengths of the two waves is equal to an integer multiple of the wavelength. The path difference between two waves undergoing interference is given by:

$$2d\sin\theta = n\lambda \tag{3.1}$$

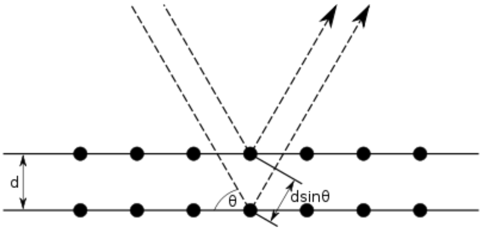

Figure 3.1: Two beams with identical wavelength and phase approach a crystalline solid and are scattered off two different atoms within it. The lower beam traverses an extra length of 2d sinθ. Constructive interference occurs when this length is equal to an integer multiple of the wavelength of the radiation

Where θ is the scattering angle.

SAXS measurements were carried out with a HECUS S3-MICRO camera (Kratky-type) equipped with a position-sensitive detector (OED 50M) containing 1024 channels of width 54 μm. Cu Kα radiation of wavelength λ = 1.542Å was provided by an ultra-brilliant point micro-focus X-ray source (GENIX-Fox 3D, Xenocs, Grenoble), operating at a maximum power of 50W (50kV and 1mA). The sample-to-detector distance was 281mm. The volume between the sample and the detector was kept under vacuum during the measurements to minimize scattering from the air. The Kratky camera was calibrated in the small angle region using silver behenate (d = 58.34Å)[9]. Scattering curves were obtained in the Q-range between 0.05 and 0.5Å^{-1}, if Q is the scattering vector.

$$Q = \frac{4}{\lambda}\sin\theta \tag{3.2}$$

Powder samples were placed into a 1 mm demountable cell having Kapton foils as windows. Liquid samples were mounted in a capillary tube (80mm length, 1.0mm diameter, wall thickness = 0.1mm). The temperature was set at 25°C and was controlled by a Peltier element, with an accuracy of 0.1°C. All scattering curves were corrected for the empty cell or capillary contribution considering the relative transmission factor.

Wide Angle X-Ray Diffraction measurements were performed in a Bruker-D8 Advance X-ray powder Diffractometer in the Bragg-Brentano -2 geometry. The X-ray source was Cu Kα radiation, operating at 40kV and 30mA with a wavelength of λ = 1.54Å. The detection was carried out using a Lynx-eye linear-type detector, in the 2θ interval from 1 to 70 degrees.

3.2 Nitrogen adsorption and desorption isotherms

Nitrogen gas sorption is the most widely and accurate method for total surface area measurements and pore sizes within the approximate range of 0.4 to 200nm in diameter. This method provides very high resolution data and has very wide applicability. Nitrogen adsorption and desorption isotherms were acquired using a Beckman Coulter SA-3100 Surface area analyzer. Calcined samples were outgassed prior to analysis in vacuum conditions at a temperature of 200°C until a pressure of 0.01mmHg was reached. If otherwise indicated, measurements were performed a single time. Random samples were measured for reproducibility purposes and were found to be within the instrumental margin of error (3%)

The gas sorption method may be defined simply as the physical characterization of material structures using a process where gas molecules of known size are condensed (or adsorbed) on unknown sample surfaces. The quantity of gas condensed and the resultant sample pressure are recorded and used for subsequent calculation. This data, when measured at a constant temperature, allows an isotherm to be constructed. Isotherm data is then subjected to a variety of calculation models to obtain surface area and pore size distribution results. The Brunauer-Emmett-Teller method is one model used for the determination of the sample specific surface area while the Barrett-Joyner-Halenda calculations yield the pore size distribution.

3.2.1 Measurement and calculation of isotherm data

The adsorption process is measured volumetrically with a static fully equilibrated procedure. From just a few to more than a hundred individual data points from all or part of the adsorption and desorption isotherms. The isotherm volume data (Y-axis or ordinate) is calculated by substracting the free space of the sample tube, which is that volume of the sample tube not occupied by the sample, from the total volume of gas dosed to the sample. An incremental data set is formed. Each data point is processed by calculating the volume adsorbed and measuring the sample pressure which is then divided by the saturation vapor pressure. This relative pressure is recorded as the X-axis or abscissa values.

The ideal gas law is used for the calculation of both the free space and the volume of adsorptive dosed. The quantity of a gas in moles n, dosed into the measurement manifold is given by the following equation, where P_M, V_M and T_M are the pressure, volume and temperature of the dose manifold and R is the Gas constant.

$$P_M V_M = nRT_M \tag{3.3}$$

The BET (Brunauer-Emmett-Teller) calculation was first introduced in 1938 and has continued to gain popularity since ever since. It is the most commonly used calculation method for the characterization of specific surface area. The BET area (which includes all internal structure) is calculated from a multilayer adsorption theory. The theory is based upon the assumption that the first layer of molecules adsorbed on the surface involves adsorbate-adsorbent energies, and subsequent layers of molecules adsorbed involve the energies of vaporization (condensation) of the adsorbate-adsorbate interaction.

The BET equation should produce a straight-line plot, the linear form of which is most often represented as:

$$\frac{P_S}{V_A(P_S - P_0)} = \frac{1}{V_M C} + \frac{C-1}{V_M C} * \frac{P_S}{P_0} \tag{3.4}$$

Where: V_M = Volume of the monolayer; V_A = Adsorbed volume; P_S = Sample pressure; P_0 = Reference pressure or saturation pressure; C = Constant related to the enthalpy of adsorption

A specified relative pressure range (usually 0.05 to 0.2) is chosen and the isotherm data is used to calculate the BET function which is plotted against relative pressure values to give a straight line having a slope (C-1)/V_M and intercept 1/V_MC.

The BET surface area is determined with the following expression:

$$S_{BET} = \frac{V_M * N_A * A_M}{M_V} \tag{3.5}$$

Where S_{BET} is the surface area, N_A is the number of Avogadro, A_M is the cross-sectional area occupied by each adsorbate molecule and M_V is the gram molecular volume (22414ml). For nitrogen BET determinations, the cross-sectional area of the adsorbate molecule is assumed to be 0.162nm^2.

3.3 Spectroscopic characterization: UV-vis diffuse reflectance and Fourier Transform Infrared Spectroscopy

Absorption spectroscopy such as FTIR and ultraviolet-visible UV-Vis spectroscopy, is used to measure how well a sample absorbs light at various wavelengths. In Attenuated total reflectance mode, a beam of infrared light is passed through the ATR crystal in such a way that it reflects at least once off the internal surface in contact with the sample. This reflection forms the evanescent wave which extends into the sample. The penetration depth into the sample is typically between 0.5 and 2 micrometers, with the exact value being determined by the wavelength of light, the angle of incidence and the indices of refraction for the ATR crystal and the medium being probed. This yields the spectrum of adsorption (or transmission) of a solid, liquid or gas.

Attenuated Total Reflectance Fourier Transform infrared spectra were obtained for samples, in the wavenumber interval from 600 to 4000cm^{-1} with an FT Infrared Spectrometer Thermo Nicolet Nexus 4700 FT-IR ATR.

UV-vis diffuse reflectance uses light in the visible and adjacent ranges. In this region of the electromagnetic spectrum, atoms and molecules undergo electronic transitions. Absorption spectroscopy is complementary to fluorescence spectroscopy, in that fluorescence deals with transitions from the excited state to the ground state, while absorption measures transitions from the ground state to the excited state.

UV-vis spectra of the Ce modified samples were acquired by using a UV-Vis Spectrometer (Perkin Elmer USA Lambda 3S) in the wavelength interval of 200 to 600nm, using MgO as reference.

3.4 Solid state nuclear magnetic resonance

Nuclear magnetic resonance (NMR) is a physical phenomenon in which nuclei in a magnetic field absorb and re-emit electromagnetic radiation. This energy is at a specific resonance frequency which depends on the strength of the magnetic field and the magnetic properties of the isotope of the atoms. NMR allows the observation of specific quantum mechanical magnetic properties of the atomic nucleus. Many scientific techniques exploit NMR phenomena to study molecular physics, crystals, and non-crystalline materials through nuclear magnetic resonance spectroscopy.

NMR spectroscopy is used to obtain physical, chemical, electronic and structural information about molecules due to either the chemical shift, Zeeman effect, or the Knight shift effect, or a combination of both, on the resonant frequencies of the nuclei present in the sample. It is a powerful technique that can provide detailed information on the topology, dynamics and three-dimensional structure of molecules in solution and the solid state. Thus, structural and dynamic information is obtainable (with or without magic angle spinning (MAS)) from NMR studies of quadrupolar nuclei (that is, those nuclei with spin $S > 1/2$) even in the presence of magnetic dipole-dipole interaction broadening (or simply, dipolar broadening), which is always much smaller than the quadrupolar interaction strength because it is a magnetic vs. an electric interaction effect.

The ^{29}Si and ^{1}H Solid-state Nuclear Magnetic Resonance spectra (MAS-NMR) of the powder samples were recorded using a Bruker AVANCE II NMR Spectrometer with a CPMAS H-X BB detector of 4mm, operating at a resonance frequency of 59MHz. The spin velocity of the sample was set at 5kHz and the recycling time between experiments was 10s using the High-Power Decoupling, Cross-Polarization technique (HPDEC).

3.5 Scanning and transmission electron microscopy

Scanning electron microscopes produce images by probing a sample with a focused electron beam that is scanned across a rectangular area of the specimen (raster scanning). When the electron beam interacts with the specimen, it loses energy by a variety of mechanisms. The lost energy is converted into alternative forms such as heat, emission of low-energy secondary electrons and high-energy backscattered electrons, light emission (cathodoluminescence) or X-ray emission, all of which provide signals carrying information about the properties of the specimen surface, such as its topography and composition. The image displayed by a SEM maps the varying intensity of any of these signals into the image in a position corresponding to the position of the beam on the specimen when the signal was generated.

Morphology and particle size of the catalysts were analyzed using a SIGMA Field Emission Scanning Microscope (Carl Zeiss Microscopy GmbH, Germany). The micrographs were acquired from uncoated samples, using the In-Lens Secondary Electron detector and the Electron Backscattered Diffraction (EBDS) simultaneously to yield Z-contrast micrographs of the catalysts.

Transmission electron microscopy uses a high voltage electron beam to illuminate the specimen and create an image. The electron beam is produced by an electron gun, commonly fitted with a tungsten filament cathode as the electron source. The electron beam is accelerated by an anode typically at 100 keV (40 to 400 keV) with respect to the cathode, focused by electrostatic and electromagnetic lenses, and transmitted through the specimen that is in part transparent to electrons and in part scatters them out of the beam.

When the beam emerges from the specimen, it carries information about the structure of the specimen that is magnified by the objective lens system of the microscope. The spatial variation in this information may be viewed by projecting the magnified electron image onto a fluorescent viewing screen coated with a phosphor or scintillator material such as zinc sulfide. Alternatively, the image can be photographically recorded by exposing a photographic film or plate directly to the electron beam, or a high-resolution phosphor may be coupled by means of a lens optical system or a fiber optic light-guide to the sensor of a digital camera. The image detected by the digital camera may be displayed on a monitor or computer.

High resolution Transmission Electron Microscopy (HR-TEM) was performed with a JEOL 2100F equipment, using a lighting source of 200kV of acceleration and a high vacuum system, to obtain both TEM and High Angle Annular Dark Field (HAADF) micrographs.

Part IV

Results and discussion

Chapter 4

Ce direct incorporation on MCM-41

4.1 US and MW-assisted synthesis of Ce-promoted mesoporous silica

4.1.1 SAXS and WAXRD characterization

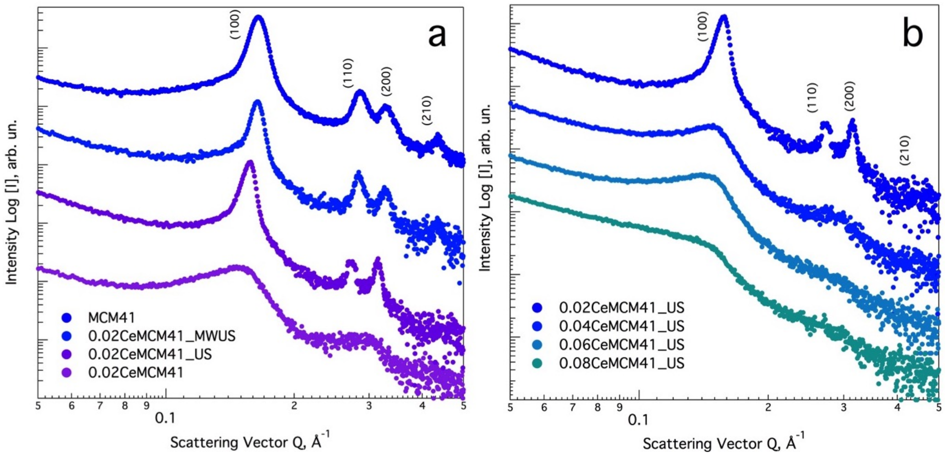

Figure 4.1: SAXS curves for a) MCM-41 and Ce-modified MCM-41 (Ce/Si = 0.02) prepared using ultrasound (US), microwaves irradiation (MW) and magnetic stirring (0.02CeMCM-41); b) SAXS curves for Ce-modified silica at different Ce/Si molar ratios. Curves are shifted arbitrarily on the y-axis for the sake of clarity.

To determine the structure and hexagonal ordering of the cerium modified silicas, Small Angle X-ray Scattering curves were recorded in the low Q interval from 0.05 to 0.5Å^{-1}. Figures 4.1a-b show the SAXS patterns for all the xCe-MCM-41 powder samples after calcination. Silicon-based mesoporous MCM-41 exhibits four well-defined diffraction peaks, centered at Q vector values of 0.165, 0.285, 0.329 and 0.435Å^{-1} that can be associated to the scattering of the first (*hlk*) planes, where hlk is equal to (100), (110), (200) and (210), indexed to the hexagonal system, space group $p6mm$[8].

Table 4.1 summarizes the interplanar distance d_{100}, and lattice cell constant a_0 for all materials. Once cerium is loaded into the hexagonal lattice, a shift towards lower reciprocal Q values is observed for all samples, which is indicative of larger d_{100} spacing values, as consequence of Ce direct incorporation (Table 4.1, d_{100} entry). In a previous publication, we demonstrated that the broadening of the d_{100} interplanar distance depends on the type of substituted heteroatom and the amount effectively incorporated in the silica framework[35]. A sample with a Ce/Si molar ratio equal to 0.02 features three well-resolved Bragg diffraction peaks (Figure 4.1-b 0.02CeMCM-41_US). Materials with higher cerium content exhibit a main scattering peak followed by secondary less resolved peaks. The interplanar spacing enlarges from 4.42nm to a maximum value of 5.04nm. This evolution towards less ordered sieves could be caused by the disparity of the covalent radii existing between Si (1.11Å) and Ce (2.04Å)[25]. Assuming that the nature of Ce incorporation into the silicon structure occurs in isomorphic manner, as the Ce/Si molar ratio increases the substitution of Si-O-Si bonding for its larger Si-O-Ce counterpart results in materials with less resolved diffraction curves. This covalent radius disproportion also accounts for larger lattice cell a_0 values (Table 4.1, a_0 entry). For the hexagonal structure, the cell constant can be estimated as:

$$a_0 = \frac{2d_{100}}{\sqrt{3}} \tag{4.1}$$

And its value ranges from 5.10 to 5.82nm (being the largest value for 0.08CeMCM-41_US).

Sample name	Ce/Si	d_{100}[a]	a_0[a]	S_{BET}, m^2/g	V_{pore} cm^3/g	D_{pore}[a]
MCM41	0	4.42	5.1	980	0.86	3.49
0.02CeMCM41[b]	0.02	4.46	5.15	967	0.94	3.88
0.02CeMCM41[c]	0.02	4.78	5.52	865	0.96	4.45
0.02CeMCM41[d]	0.02	4.63	5.35	806	0.77	3.84
0.04CeMCM41[d]	0.04	4.88	5.63	711	0.68	3.84
0.06CeMCM41[d]	0.06	4.98	5.75	629	0.65	4.14
0.08CeMCM41[d]	0.08	5.04	5.82	546	0.6	4.39

Table 4.1: Lattice cell parameters and textural properties for cerium modified mesoporous silica. [a]Units expressed in nm; [b]Synthesized using US for cerium dispersion and MW for hydrothermal synthesis; [c]Conventional hydrothermal synthesis without US ageing; [d]Synthesized using US for cerium dispersion

To better understand the formation mechanism of the hexagonal silica framework, SAXS curves for the synthesis colloid were measured in a capillary cell along the same Q interval (Fig. 4.2). Under the acquisition parameters (50W, t_{acq} = 1800s), the amphiphilic cationic surfactant solution in NH_4OH does not produce any scattering pattern typical of a hexagonal structure. Upon alkoxide addition, given the strong alkaline conditions (pH = 12.7), the tetraethyl orthosilicate molecules are rapidly hydrolyzed and interact with the positively charged cationic micelles. For the CTAB/TEOS/NH_4OH system, a main Bragg peak can be observed with secondary less-defined peaks, suggesting that micellar ordering into a hexagonal structure occurs immediately after TEOS hydrolysis and silica oligomer formation (TEOS/CTAB molar ratio 1:0.30). Therefore, for a successful cerium incorporation it is important to enhance dispersion of the Ce precursor before TEOS addition and silica polymerization.

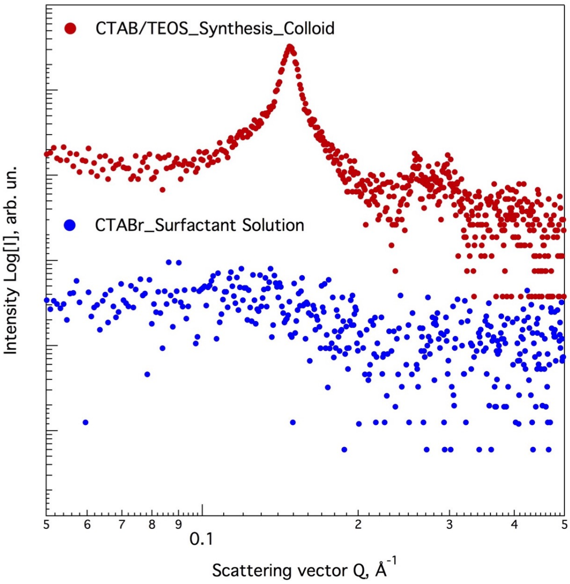

Figure 4.2: SAXS curves for CTABr/NH_4OH solution and CTAB/TEOS/NH_4OH Colloid (Ageing time, t = 0). Curves are arbitrarily shifted on the y-axis for the sake of clarity. Position of the main scattering peak for CTAB/TEOS is Q = 0.15Å^{-1}. Acquisition conditions: 50W, t = 1800 sec.)

A comparative study was performed to assess the hexagonal framework regularity of samples with a Ce/Si ratio of 0.02. It is noteworthy that a material prepared without US for Ce dispersion featured a broad d_{100} peak centered on Q = 0.152Å^{-1}; a second less resolved peak, which could be interpreted as the convolution of the d_{110} and d_{200} planes, is centered at Q = 0.297Å^{-1}. On the contrary, a sample prepared using ultrasounds (0.02CeMCM_US) featured three Bragg peaks in the explored low Q interval (d_{100} = 4.63nm). This suggests that the micromixing produced by acoustic cavitation effectively promoted better Ce dispersion and incorporation in the silica network during nucleation and micellar organization, compared to magnetic stirring. Considering that template-based mesoporous silica sieves with hexagonal ordering and high surface can be obtained within an hour using microwave ovens[107] or microwave digestion systems[76] (closed-box approach), the hydrothermal synthesis was enhanced by MW irradiation using a coaxial antenna for *in situ* application in a high pressure reactor[34]. A 0.02Ce/Si molar ratio mesoporous material was prepared using US during the nucleation step and MW for thermal activation during hydrothermal particle growth. Figure 4.3 shows the temperature profile for 0.02CeMCM-41_MWUS. Under this innovative synthesis approach, 100°C can be achieved within two minutes of applied power (operating at a maximum power of 240W); then, a PID controller keeps a variable supply of around 60W to maintain the desired operating temperature. Similarly, a well-defined SAXS diffraction pattern was recorded for the material prepared using MW irradiation. The interplanar distance calculated for this sample was the closest to the MCM-41 parent material (4.46nm).

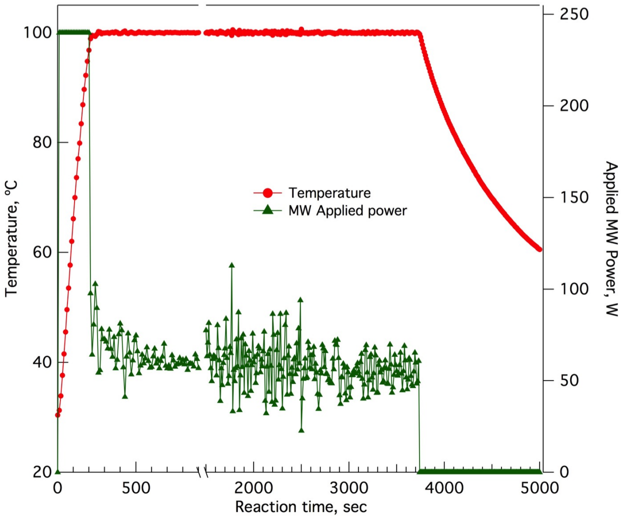

Figure 4.3: Temperature profile for the MW-assisted synthesis of Ce-mesoporous silica

Although US-enhanced mixing was helpful in achieving Ce distribution and substitution during silica self-assembly, at higher Ce/Si ratios the amount of cerium load and a larger concentration of counter ions (NO^{3-}) could be responsible for hindering the hexagonal ordering by modifying micelle aggregation and density numbers[38]. On a previous report[82], optimal values for surfactant/Si and Ce/Si molar ratios were found for Ce substituted MCM-41 (0.2 and 0.025 respectively) by analyzing the X-ray scattering and intensity of the d_{100} plane. A Ce-MCM41 sample prepared under magnetic stirring with a Ce/Si molar ratio of 0.025, exhibited only the scattering of the first two hlk planes. Taking into account the SAXS scattering curves (Bragg peaks for the (100), (110) and (200) planes for both 0.02CeMCM-41_MWUS and 0.02CeMCM-41_US), the ultrasound-assisted methodology here reported resulted in a material with better cerium dispersion along the hexagonal framework and a higher degree of hexagonal ordering.

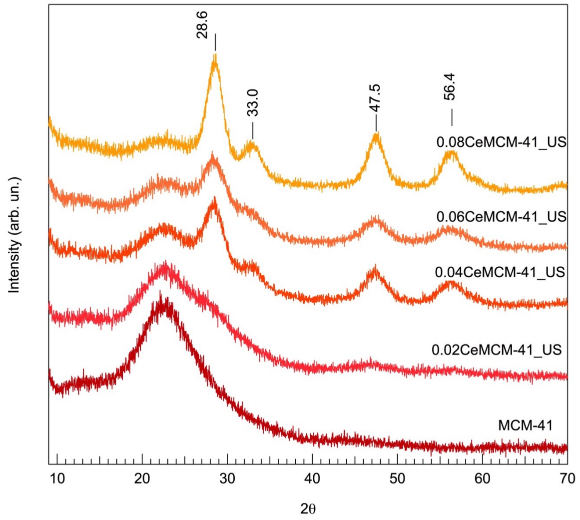

Figure 4.4: WAXRD curves for xCe-MCM-41_US materials

To further characterize the Ce content in all samples, wide angle XRD curves for the xCe-MCM-41_US materials were recorded in the 2θ interval from 10 to 70° (Figure 4.4). Unmodified mesoporous silica and the samples with lowest Ce/Si molar ratio exhibit a single broad peak, encompassing 2θ values from 18 to 26°. For Ce/Si values of 0.04 and higher, four diffraction peaks are observed at around 2θ values of 28.6, 33, 47.5 and 56.4°, indexed to the Bragg scattering of the (111), (200), (220) and (311) planes for the cubic phase in CeO_2. Sharper and more intense diffraction peaks were observed for the sample with the highest Ce content (0.08CeMCM-41_US). In conjunction with the SAXS analysis these findings lead to some conclusions concerning the possible mechanism of Ce incorporation into the hexagonally ordered mesoporous silica. For low metal loadings, the well preserved hexagonal structure is indicative of a successful Ce dispersion and isomorphic incorporation in the SiO_2 structure, promoted by the use of ultrasounds acoustic cavitation. Higher Ce/Si molar ratios could favor two different mechanisms of incorporation: isomorphic substitution within the hexagonal framework and the formation of cubic CeO_2 particles outside the silica sieve.

4.1.2 FT-IR and UV-Vis DR Spectroscopic characterization

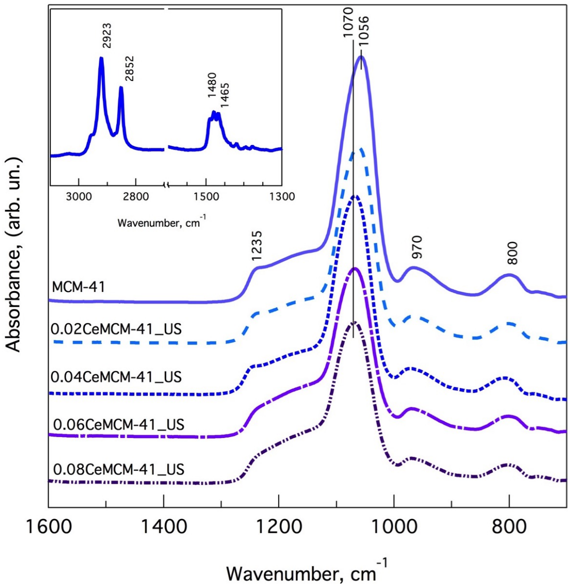

Figure 4.5: FT-IR ATR spectra for cerium-modified mesoporous silica (inset figure: as-synthesized MCM-41)

The FT-IR ATR spectra for all xCe-MCM-41_US materials are shown in Figure 4.5. Silica MCM-41 features three main bands that can be assigned to the asymmetrical stretching vibration (ν_{as}) of the Si-O-Si bond located at wavenumber values of 1235, 1056 and 970cm^{-1}. For all cerium modified materials the main band located at 1056 shifts to 1070cm^{-1} while the intensity of the band located at 1230cm^{-1} is reduced as the molar ratio Ce/Si increases, suggesting a lower recurrence of Si-O-Si that could be replaced by Si-O-Ce bonds. The signals at about 1465 and 1480cm^{-1} can be assigned to the $\delta(CH_2)$ and $\delta_{\mathrm{as}}(N\text{-}CH_3)$ bending modes of the surfactant molecule within the pores (scissoring region), whereas the bands at 2852 and 2923cm^{-1} belong to the symmetric and asymmetric ($\nu_{\mathrm{symm}}(CH_2)$ and $\nu_{\mathrm{as}}(CH_2)$) stretching modes of the surfactant chains[45] (inset figure 4.5). After calcination these bands are no longer present in the spectrum. The location and intensity of the band centered at 800cm^{-1}, attributed to the vibrations of the ν_{symm}(Si-O-Si) does not change as a consequence of cerium incorporation.

In order to determine the coordination of the Ce species in the hexagonal silica framework, the UV-visible Diffuse Reflectance Spectra for all calcined samples was recorded. Figure 4.6 shows a single broad band in the wavelength interval from 200 to 400nm for all samples with a maximum value at around 330nm. The intensity of this band increases with the amount of Ce introduced in the sample. For crystalline cerium oxide

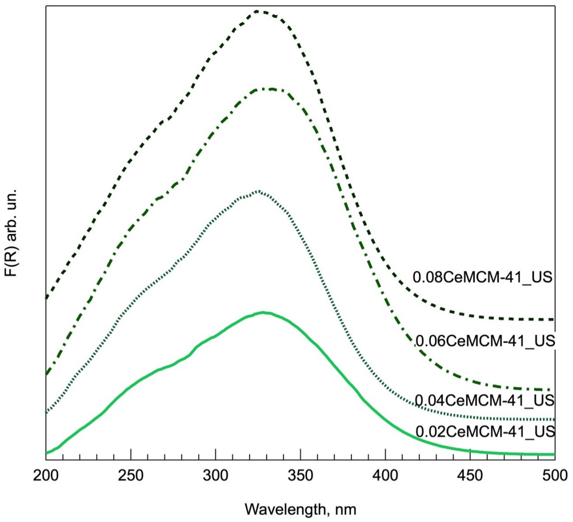

Figure 4.6: UV-visible Diffuse Reflectance spectra for x-Ce-MCM-41_US calcined materials

(CeO_2), there is a band gap of 3.1eV (3.7eV at 330nm for these materials). Since the electronic transitions in the hexa-coordinated atom (Ce^{3+}) require more energy than the transitions for the tetra-coordinated atom (Ce^{4+}), it is possible to assign this band to the transitions Ce-O for Ce^{4+},[63]. Regardless of the position and distribution of Ce in the hexagonal silicon structure, the nature of the cerium species is tetra-coordinated for all cases.

4.1.3 Transmission Electron Microscopy

High Resolution Transmission Electron micrographs shown in figure 4.7 provide supplementary evidence of the hexagonal arrangement characterizing the Ce modified mesoporous silica. For unmodified MCM-41, two different observation angles are featured: the cross sectional area offers a view of the hexagonal structure (Fig. 4.7-a). A second view along the channels of the mesoporous material (Fig. 4.7-b) confirms the interplanar d_{100} distance calculated by SAXS. As the material losses the degree of ordering, the interplanar distance and the pore size enlarges as a consequence of the amount of incorporated cerium in the sample. For all mesoporous solids, a honeycomb-like structure is observed. High-Angle Annular Dark-Field Imaging of the sample with the highest cerium contents (Fig. 4.7-g and 4.7-h) feature medium size CeO_2 domains condensed outside the silicon framework, which are not found in samples with lower Ce/Si ratios.

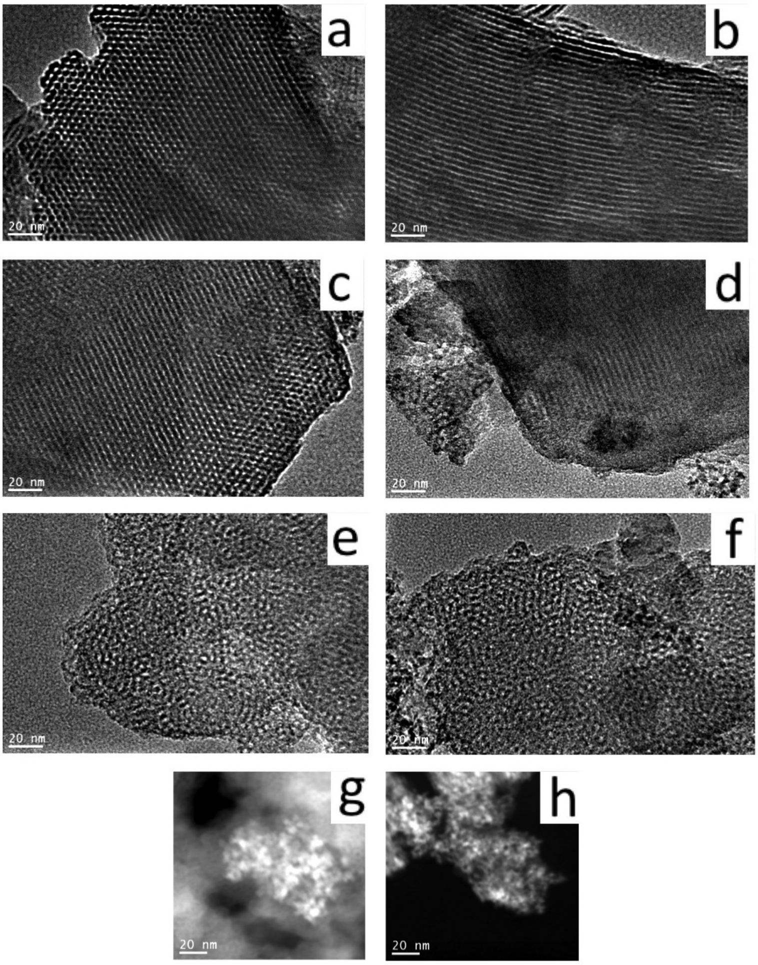

Figure 4.7: HR-TEM: a) Cross sectional area of the hexagonal structure and b) view along the channels for MCM-41; c) Hexagonal structure and d) interplanar distance for 0.02CeMCM-41_US; e) 0.04CeMCM-41_US and f) 0.06CeMCM-41_US; g) HAADF Imaging for CeO_2 particles in 0.08CeMCM-41_US and h) 0.06CeMCM-41_US. (Bar length = 20nm for all micrographs)

4.2 Ni supported on Ce-modified mesoporous silica

4.2.1 N_2 adsorption and desorption isotherms

The Ce-promoted silicas were used as catalytic support for a Ni active phase (10% metal content). Nitrogen adsorption-desorption isotherms were recorded for calcined powders before and after Ni loading. Figure 4.8 shows the N_2 isotherms and pore size distribution for selected samples. According to the classification made by IUPAC[97], all prepared materials exhibit a type IVa isotherm, characteristic of mesoporous materials ranging from 2 to 50nm in pore size. For all catalytic supports, four well-defined regions in the isotherm can be identified: a) A large nitrogen uptake at very low relative pressure values (P/P_0 up to 0.02), that can be associated to micropore filling and monolayer formation; b) An inflection point and slope change followed by a more linear region in the isotherm curve is indicative of unrestricted multilayer adsorption; c) A second inflection point at relative pressure values close to 0.30 with a significant amount of adsorbed nitrogen is due to capillary condensation. This relative pressure value is closely related to the pore diameter and; d) A final saturation plateau once the mesopores are filled is associated to adsorbed nitrogen on the outer surface of the material and in between particles.

After Ni loading, the isotherm form is kept and no significant area reductions occur, suggesting that Nickel is well distributed and does not produce pore blocking. For Ni/MCM-41 and Ni/0.02CeMCM-41 a final N_2 uptake at relative pressure values close to 1.0 could be indicative of inter-particle sintering and adsorption that does not contribute to the surface area calculations. The Barrett-Joyner-Halenda pore size distribution graphs (inset figures 4.8a-d), show a monomodal size for mesoporous solids prepared at low Ce/Si molar ratios.

A summary of the textural properties for all materials is reported in Table 4.1. The calculations for the surface area were performed with the BET method. Unmodified mesoporous MCM-41 features the highest surface area ($980 m^2/g$), the narrowest pore size estimated as 3.49nm (assuming a cylindrical pore with open endings), and pore volume ($0.86 cm^3/g$). For the cerium-promoted mesoporous silicas, the highest surface area was obtained when microwave irradiation was used for thermal activation during the hydrothermal synthesis, which could be attributed to a more efficient heating promoted by MW bulk heating. A more uniform temperature profile obtained with the use of microwaves for thermal activation could trigger a homogeneous particle growth during silica polymerization under solvothermal treatment. The sample with the highest Ce/Si molar ratio has a surface area of $546 m^2/g$.

Concerning the pore dimensions, the pore diameter broadens from 3.49nm for unmodified mesoporous silica, to the largest value of 4.39nm for 0.08CeMCM-41_US and the monolayer adsorptive capacity is reduced to $125 m^2/g$. Nonetheless, all synthesized materials exhibit areas well above the values reported elsewhere for ceria and ceria/silica as catalytic supports[41,66], or those obtained with sol-gel methodologies. Since the pore size tends to enlarge as a consequence of the increment in the amount of Ce in the sample, a reduction in the capillary forces in the material could occur, and the total pore volume decreases to $0.60 cm^3/g$, without implying a morphology change.

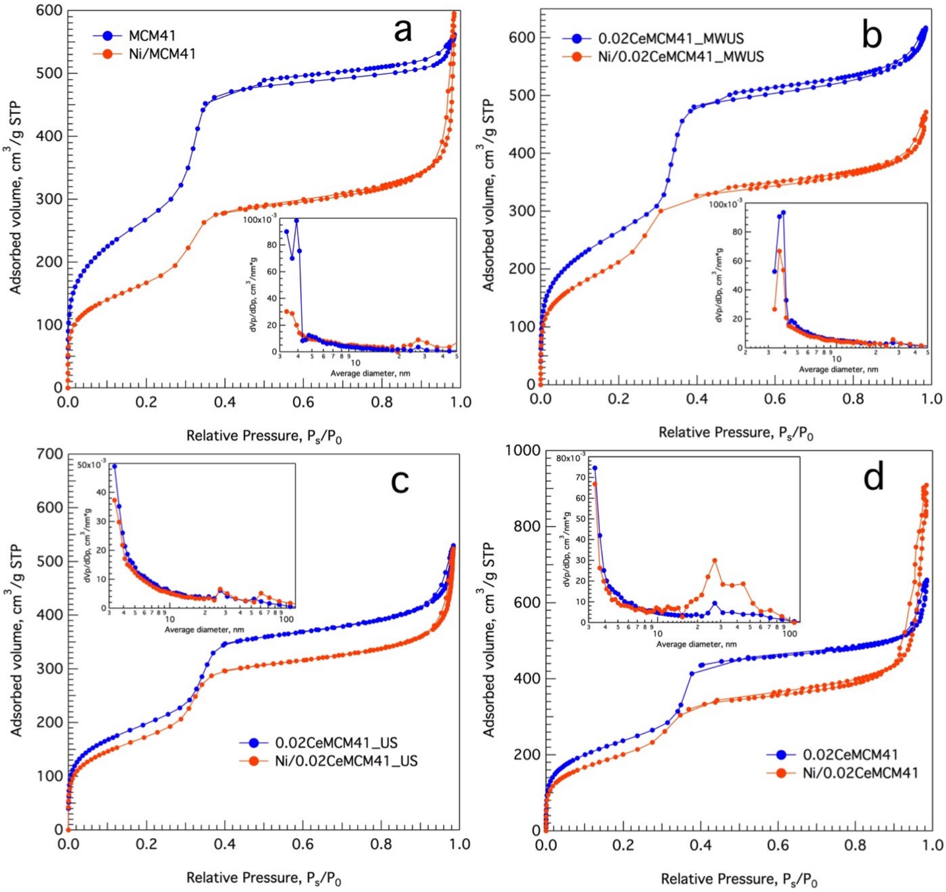

Figure 4.8: N_2 adsorption and desorption isotherms for a) MCM-41 and Ni/MCM-41; b) 0.02CeMCM-41_MWUS and Ni/0.02CeMCM-41_MWUS; c) 0.02CeMCM-41_US and Ni/0.02CeMCM-41_US; d) 0.02CeMCM-41 and Ni/0.02CeMCM-41

4.2.2 Scanning Electron Microscopy

To characterize the Ni deposition and particle morphology for the mesoporous MCM-41 materials, scanning electron micrographs were acquired using dual detection for secondary and backscattered electrons to yield Z-contrast images of the Ni active phase on the catalyst surface (Fig. 4.9-a and 4.9-b). The wet impregnation method enabled the formation of highly dispersed Ni clusters using cerium modified MCM-41 as catalytic support. Although the dispersion of Ni catalyst on pure siliceous MCM-41 was recently reported by co-condensation[108] and co-impregnation[84], the effect of cerium isomorphic incorporation on the particle size of the Ni clusters is still poorly understood. Nonetheless, the methodology here reported, resulted in catalyst with a very well distributed Nickel active phase. For MCM-41, elongated club-like particles can be observed with well-distributed Ni particles along the mesoporous structure.

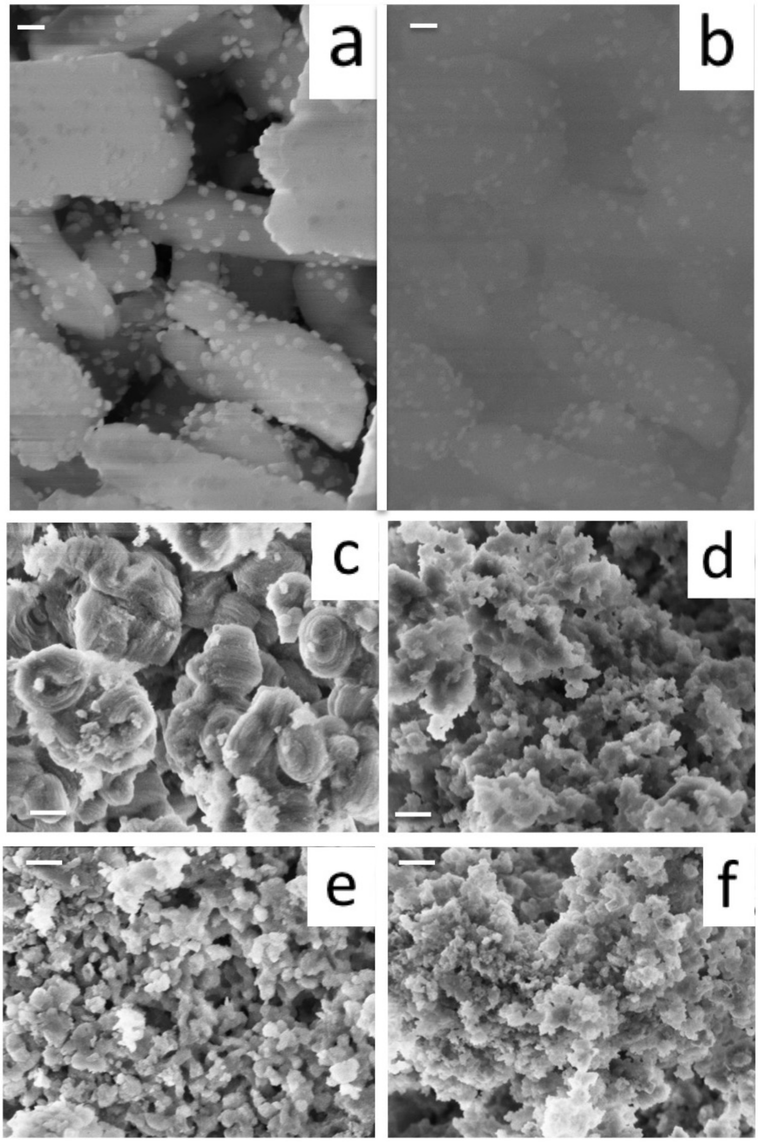

Figure 4.9: SEM Micrographs for 10%Ni/MCM-41: (a) Obtained using the In-lens detector. (b) Z-contrast image acquired using Backscattered Electron Diffraction. Particle morphology for: (c) Ni/0.02CeMCM-41_US, (d) Ni/0.04CeMCM-41_US, (e) Ni/0.06CeMCM-41_US and (f) Ni/0.08CeMCM-41_US catalysts. (Bar length = 200nm, magnification 100kX for all micrographs)

Concerning morphology, as the amount of cerium increases in the sample, the disruptive effect of Ce incorporation on the self-assembly of the micellar aggregates and particle growth produced a different morphology in MCM-41 resulting in shorter round-like particles (for intermediate Ce content) and flake-like morphologies (at higher Ce/Si ratios). Large Ni particles are easily observed in pure Si MCM-41 (Fig 4.9a and 4.9b) that were not distinguished in other materials, suggesting that the presence of the heteroatom results in a different synergy between Ni and the catalytic support by promoting the formation of smaller Ni clusters.

4.3 Catalytic evaluation of Ni/Ce-MCM-41

4.3.1 Hydrogen production through ethanol steam reforming (ESR)

The catalytic performance of Ni supported on xCe-MCM-41 was evaluated in the ethanol steam reforming reaction (ESR). The overall reaction is:

$C_2H_5OH + 3H_2O \Rightarrow 6H_2 + 2CO_2$ (1)

For the Ni/xCeMCM-41 catalyst series, figure 4.10 reports ethanol conversion and product distribution vs. reaction time. The molar composition for the individual species (y_i) was calculated in terms of all the formed products:

$$y_i = \frac{F_j}{\sum F_j} \tag{4.2}$$

The conversion of ethanol was obtained using the value of the fluxes at the entrance and exit of the reactor:

$$x_{EtOH} = \frac{(F_{in} - F_{out})}{F_{in}} * 100 \tag{4.3}$$

According to a proposed reaction mechanism[42], some of the side reactions that can occur during the ESR are ethanol decomposition or cracking to C1 products (Reac. 2), followed by steam reforming of CH_4 (Reac. 3)

$C_2H_5OH \Rightarrow CH_4 + CO + H_2$ (2)

$CH_4 + 2H_2O \Rightarrow 4H_2 + CO_2$ (3)

Concerning the reactions that produce catalyst deactivation by Carbon deposition, surface coking is produced by CH_4 decomposition (Reac. 4), Boudouard reaction (Reac. 5) and ethanol dehydration to ethylene (Reac. 6), followed by surface polymerization and carbon deposition.

$CH_4 \Rightarrow 2H_2 + C$ (4)

$2CO \Rightarrow CO_2 + C$ (5)

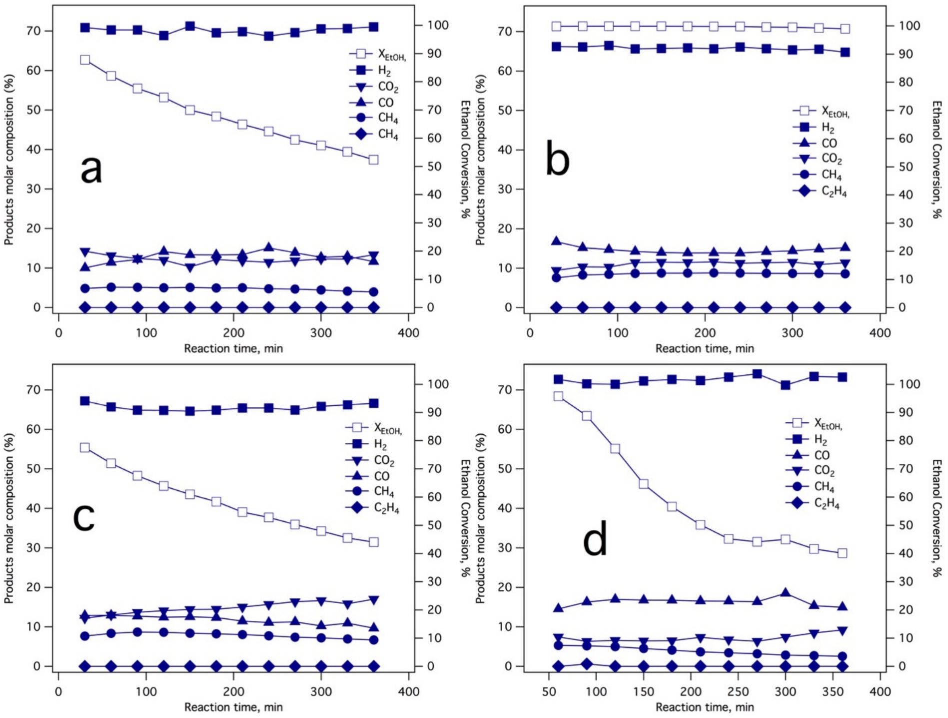

Figure 4.10: Ethanol conversion (right axis, open markers) and product distribution (left axis, dark markers) for Ni/xCe-MCM-41 catalyst in the ESR reaction: a) Ni/MCM-41 at 500°C; b) Ni/0.04CeMCM-41_MWUS at 500°C; c) Ni/0.02CeMCM-41_MWUS at 450°C d) Ni/0.02CeMCM-41 (Conventional synthesis, no US) at 500°C

$C_2H_5OH \Rightarrow C_2H_4 + H_2O$ (6)

When unmodified silica MCM-41 was used as catalytic support, the Ni/MCM-41 catalyst swiftly deactivated after 6h on stream, from a starting value of 88% to a final value of 52% in ethanol conversion. The molar fraction for all products remained constant and was 70% for H_2, 13% for CO_2, 12% for CO, 4% for CH_4 and traces of C_2H_4 (figure 4.10-a). On the other hand, cerium promoted silica (0.02CeMCM-41_MWUS, fig. 4.10b) resulted in complete hydrogen conversion at 500°C while product distribution was 65% H_2, 11.4% CO_2, 15% CO, 8.6% for CH_4 and traces of C_2H_4. The lower methane molar fraction for bare silica as support could be associated to CH_4 decomposition to carbon (Reac. 4), which slightly increases the H_2 yield.

For the Ce-containing catalytic supports, full ethanol conversion was achieved and the main product distribution was not significantly dependent on cerium content. Hydrogen selectivity ranged from 60 to 65%, CH_4 from 8.5 to 10% and no traces of acetaldehyde or C2 products were detected. Similarly, product selectivity was found to be independent of Ce content on

MCM-41 for a Rh over Ce-MCM-41 catalyst, while ethanol conversion was reported to decrease at higher cerium loads (Si/Ce = 10) in the catalytic support[37]. The stability and ethanol conversion of the Ce-promoted mesoporous silica can be attributed to the convertibility of $Ce^{4+} \Rightarrow Ce^{3+}$ in the catalyst surface. The reduced Ce^{3+} sites produce H_2O dissociation to form OH^- surface groups, which catalyze the reforming of C1 species (Reac. 3). This reaction pathway was reported before for a Ni catalyst supported on Cubic CeO_2[111].

In order to analyze the ethanol conversion and hydrogen selectivity at a lower temperature level, the ESR was carried out on 0.02CeMCM-41_MWUS at 450°C (figure 4.10-c). While a similar product distribution was observed, the Ni catalyst was less active at this temperature since ethanol conversion dropped from 77 to 44% after 6h on stream. H_2 selectivity was above 65% and the catalyst yielded lower CO and CH_4 in the products stream (compared to the same catalyst at 500°C), suggesting that after ethanol cracking, C1 products are carbonized via methane decomposition and Boudouard reactions (Reacs. 4 and 5).

For comparative purposes, a sample prepared with conventional hydrothermal synthesis without US for Ce dispersion was also used as catalytic support. For this material, a swift catalyst deactivation is also observed. After achieving high ethanol conversion during the first hour on stream, the final value was below 40%. Product distribution was found to be 73% for H_2, 15% for CO, 9% for CO_2 and 2% for CH_4. A higher carbon monoxide yield, compared to the US-synthesized supports, could be indicative of a poor distribution of the Ce species that do not catalyze complete oxidation from CO to CO_2. Carbon deposition for this particular sample could be associated to methane decomposition, since CH_4 composition was the lowest for all catalyst.

A further screening on the Ce/Si ratios for the catalytic support and Ni loading is beyond the scope of this study since the properties of the parent material MCM-41 are no longer preserved.

4.3.2 SEM micrographs for spent Ni/Ce-MCM-41 catalysts

Figure 4.11 shows the graphitic carbon formation on Ni/xCe-MCM-41_US catalysts. For all the Ce-promoted silicas, only traces of ethylene were observed (below 0.1%), which suggest that after ethanol dehydration (Reac. 6), ethylene quickly polymerizes resulting in carbon deposition. Nevertheless, the Ce modified mesoporous silica provides a suitable matrix for the immobilization of the Ni species since no metallic sintering was

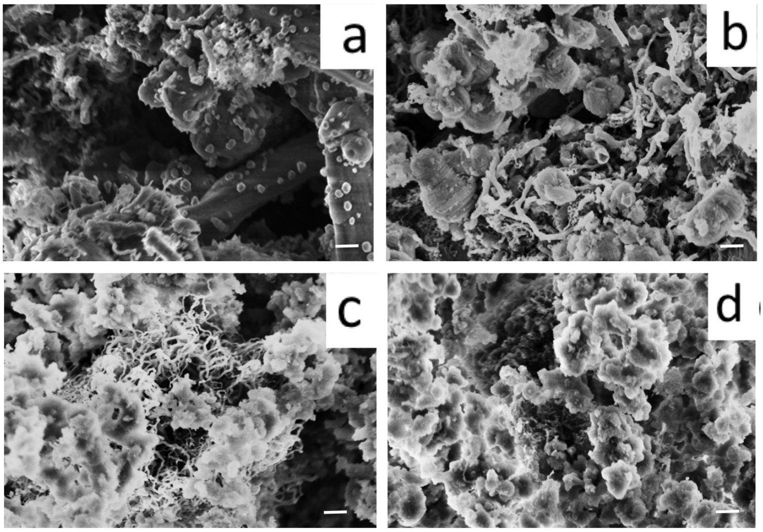

Figure 4.11: Nanocarbon filaments formation over a) Ni/MCM-41, b) Ni/0.02CeMCM-41_US, c) Ni/0.04CeMCM-41_US and d) Ni/0.06CeMCM-41_US after 6h on reaction stream (Bar length = 200nm, magnification 100kX)

observed. The distribution of the Ce species in hexagonally ordered catalytic sieve resulted in formation of carbon nanofibers rather than aggregated carbon. A reaction mechanism for the formation of carbon nano-filaments has been reported over another transition metal catalyst[49].

The hexagonal structure and surface features of Ce-MCM-41 used as catalytic support result in a controlled growth of carbon nanofibers that do not produce catalyst deactivation by carbon poisoning. Cerium incorporation to the support favors the formation of smaller carbon filaments (Fig. 4.11), even at the lowest concentration used in the present research.

Chapter 5

CeO_2-SiO_2 composite mesoporous materials

5.1 Tuning the pore diameter, particle size and surface area of self-assembled mesoporous silica

5.1.1 Small Angle X-ray Scattering curves

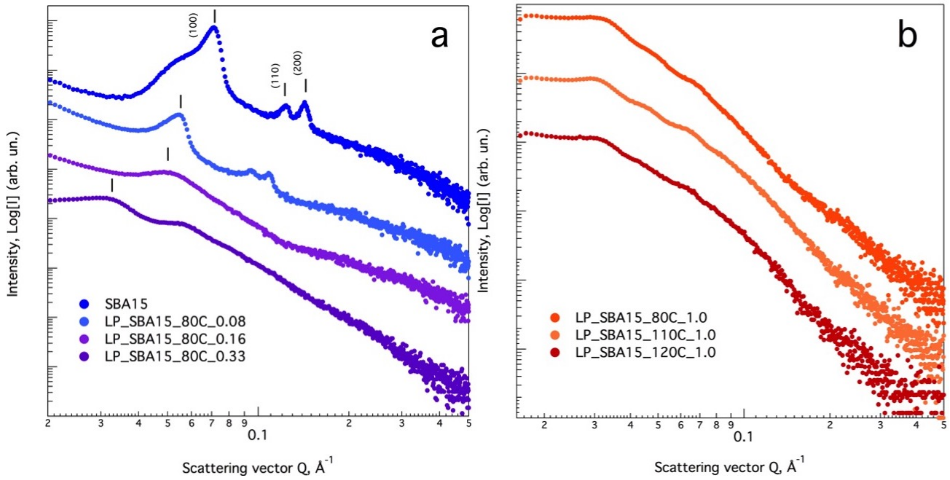

Figure 5.1: SAXS curves for a) Large pore mesoporous SBA-15 prepared under different TMB/P123 wt ratios and b) Large pore SBA-15 prepared under different hydrothermal synthesis temperature

The SAXS curves for the calcined silica supports are shown in figures 5.1a-b. All prepared materials exhibit at least one Bragg diffraction peak in the explored low-Q interval, which can be assigned to the scattering of the d_{100} plane for the hexagonal structure, space group $p6mm$[120]. For unmodified mesoporous SBA-15 (Fig. 5.1a), three well defined diffraction peaks can be found centered at 0.39, 0.56 and 0.61Å^{-1} reciprocal Q values, which can be indexed to the scattering of the (100), (110) and (200) hlk planes respectively. Table 5.1 shows the interplanar distances and lattice cell parameters for all prepared materials, calculated with the scattering of the main diffraction peak.

Sample	TMB/P123^a	d_{100}^{b}	a_0^{b}	S_{BET}^{c}	V_{pore}^{d}	D_{pore}^{b}
SBA-15	0	10.3	11.9	781	0.82	4.2
SBA-15-80^e	1	27.7	32	716	1.71	9.6
SBA-15-110^e	1	30.9	35.7	516	2.42	18.8
SBA-15-120^e	1	30.9	35.7	464	2.49	21.5
SBA-15-80^e	0.33	24.3	39.6	560	0.92	5.3
SBA-15-80^e	0.16	15.2	17.5	631	0.86	5.5
SBA-15-80^e	0.08	13.6	15.7	599	0.79	6.6

Table 5.1: Textural properties and lattice cell parameters for large pore mesoporous silica SBA-15. ^{a}Trimethylbenzene/Pluronic P123 w/w mass ratio; ^{b}Units are expressed in nm; ^{c}BET surface area in m^2/g; ^{d}Pore volume reported in cm^3/g units; ^{e}Indicates the selected temperature for hydrothermal treatment.

The parent material SBA-15 features an interplanar distance of 10.3nm. As the amount of swelling agent increases, the position of the main scattering peak is shifted towards lower reciprocal Q values, which is indicative of larger d_{100} spacing and lattice cell a_0 values. A sample prepared with a TMB/P123 ratio of 0.08 has also three well-defined diffraction peaks in the explored Q interval. Samples prepared at higher TMB/P123 ratios exhibit a single scattering peak, suggesting that a larger amount of trimethylbenzene may modify the packing parameter of the surfactant[110] and therefore hinder self-assembly into a hexagonal structure. A similar trend was observed for another type of large pore mesoporous silica when 1,3,5-triisopropylbenze was used as micelle expander[15].

To analyze the effect of the temperature and thus the effect of autogenous pressure on the characteristics of mesoporous solids, samples with the highest TMB/P123 ratio were prepared at 80, 110 and 120°C (Fig. 5.1b). From the SAXS curves, it is possible to observe that the position of the main diffraction peak remains the same for samples prepared at 110 and 120°C. Therefore, the temperature and pressure have a limited effect on the final micellar size which is largely controlled by the amount and interaction of trimethylbenzene with the hydrophobic polypropylene portion of the surfactant molecule. By modifying the amount of swelling agent, it is possible to tailor the interplanar distance from 10.3 up to 30.9nm in size; Consequently, the lattice cell constant broadens from 11.9 to 35.7nm (for the largest TMB/P123 mass ratio).

5.1.2 Scanning Electron Microscopy

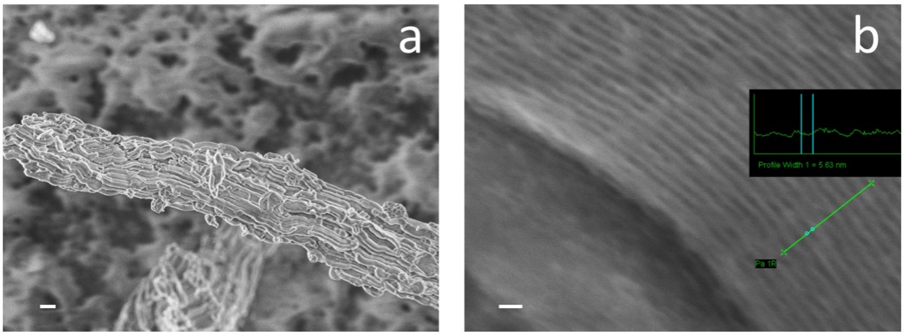

Figure 5.2: Scanning Electron Micrographs for mesoporous silica SBA-15: a) Particle morphology, bar length = 1μm, magnification 10kX; b) View along the mesopores, bar length = 20nm, magnification 800kX

SEM micrographs for the prepared samples are presented in figures 5.2 and 5.3. Figure 5.2a shows the particle morphology for unmodified SBA-15. Once the micellar aggregates start to polymerize, a characteristic fiber multirod-like structure tends to form which has a variable diameter profile up to 7μm in diameter and can grow up to several micrometers in length, forming larger swirled structures. Figure 5.2b shows a view along the hexagonal channels of the mesoporous silica which further confirms the interplanar spacing calculated from the SAXS diffraction pattern.

Figure 5.3 shows the particle morphology for the large pore mesoporous SBA-15 samples. As the amount of swelling agent increases, the twisted rope formations are no longer present and the particles tend to be rounder and shorter in length size. For the samples prepared at higher temperature level, the autogenous pressure may be responsible for limiting their size to less than 10μm and providing them with well-rounded edges in a muffin-like shape.

5.1.3 N_2 adsorption and desorption isotherms

Figure 5.4a shows the Nitrogen adsorption and desorption curve for pure siliceous SBA-15 featuring a type IV isotherm. This is characteristic of porous solids with sizes in the interval from 2-50nm according to the classification made by IUPAC[97]. Four well-defined regions can be observed: a) An initial high nitrogen uptake under relative pressure values $P_S/P_0 < 0.04$ is due to the formation of the monolayer and micropore filling; b) An inflection point followed by a more linear region of the isotherm is associated to unrestricted multilayer formation until a second inflection point is reached; c) A second large nitrogen uptake is indicative

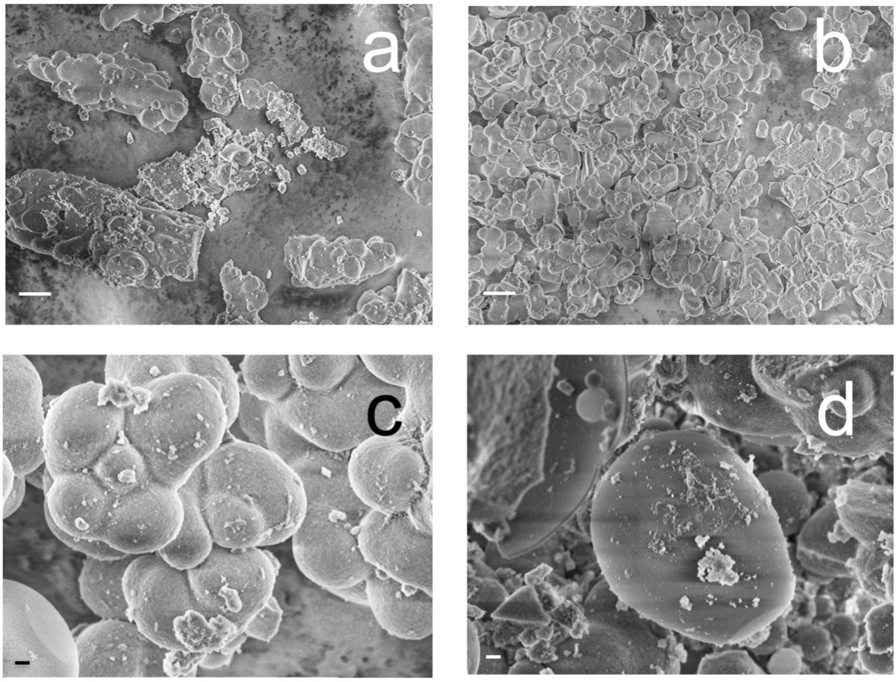

Figure 5.3: SEM for a) LP-SBA-15-80C-0.08; b) LP-SBA-15-80C-0.33; Bar length 10μm, magnification 2kX c) LP-SBA-15-110C-1.0, d) LP-SBA-15-120C-1.0 (Bar length 1μm, magnification 10kX)

of mesopore capillary condensation, and d) A final saturation plateau without significant changes on the volume of nitrogen adsorbed could be due to interparticle adsorption and adsorption on the outer surface of the material. Due to a different desorption mechanism, a type H1[97] hysteresis loop is clearly observed, which is narrow along a short relative pressure interval, indicative of cylindrical pores with open endings. Figure 5.4b features a sharp pore volume distribution curve, obtained with the Barrett-Joyner-Halenda method that further confirms the pore geometry and the estimated pore diameter.

Table 5.1 (S_{BET}, V_{pore} and D_{pore} entries) summarizes the textural properties for the prepared samples. The surface area was calculated with the Brunauer-Emmett-Teller method, which assumes multilayer condensation. The largest surface area was observed for the parent material SBA-15 at 781m^2/g, whereas large pore silicas feature surface areas ranging from 560 to 716m^2/g. A more direct effect was observed in the average pore size, which was estimated as $D = 4 * V_{pore}/S_{BET}$, assuming a cylindrical pore geometry with open endings. The smallest pore size was that of SBA-15 equal to 4.20nm; at low TMB/P123 mass ratios, the pore size broadens to close values between 5.26 and 6.56nm. For larger TMB/P123 ratios equal to 1.0 the pore diameter enlarges to 9.55nm when

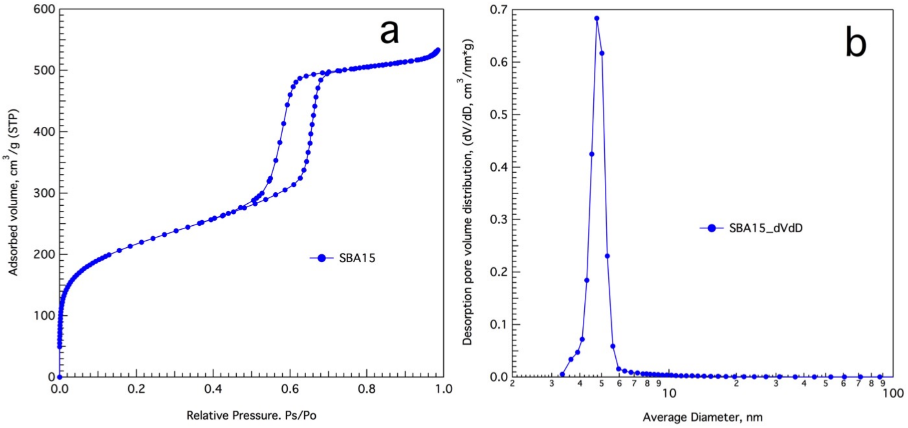

Figure 5.4: a) Nitrogen adsorption and desorption isotherm; b) BJH Pore volume distribution

synthesized at 80°C; then at higher temperature levels of 110°C and 120°C the resulting pore sizes are 18.77 and 21.47nm respectively. The higher temperature could produce a better diffusion of the organic phase to the hydrophobic core of the micellar arrangements by increasing the kinetic energy and velocity of the molecules. A larger amount of trimethylbenzene occluded within the micelle is therefore responsible for an increased pore size and pore volume. A value of $2.49cm^3/g$ is the largest pore volume for LP-SBA15-120C-1.0, estimated at a relative pressure value of $P_S/P_0 = 0.9984$. In a similar fashion, the lowest pore volume of $0.82cm^3/g$ is for mesoporous SBA-15 and the total pore volume increases with the amount of swelling agent and synthesis temperature.

Figure 5.5 shows the adsorption and desorption isotherms for the materials prepared with variable Trimethylbenzene/Pluronic P123 mass ratio and different temperature levels. By increasing the amount of micelle expander, the relative pressure value at which capillary condensation occurs is shifted towards higher relative pressure values. Values closer to $P_S/P_0 = 1.0$ tend to have a broad and less defined hysteresis loop, whereas the temperature increase produces a narrow type H1 loop. The highest relative pressure value at which nitrogen uptake increases due to capillary condensation was found for the sample with the largest pore diameter LP-SBA15-120C-1.0. For materials prepared at 110 and 120°C the pore size distribution function tends to broad (inset figure 5.5a-f).

5.2 CeO_2 Mesoporous SiO_2 nanocomposites

Table 5.2 summarizes the textural properties for cerium oxide deposited on mesoporous silica SBA-15.

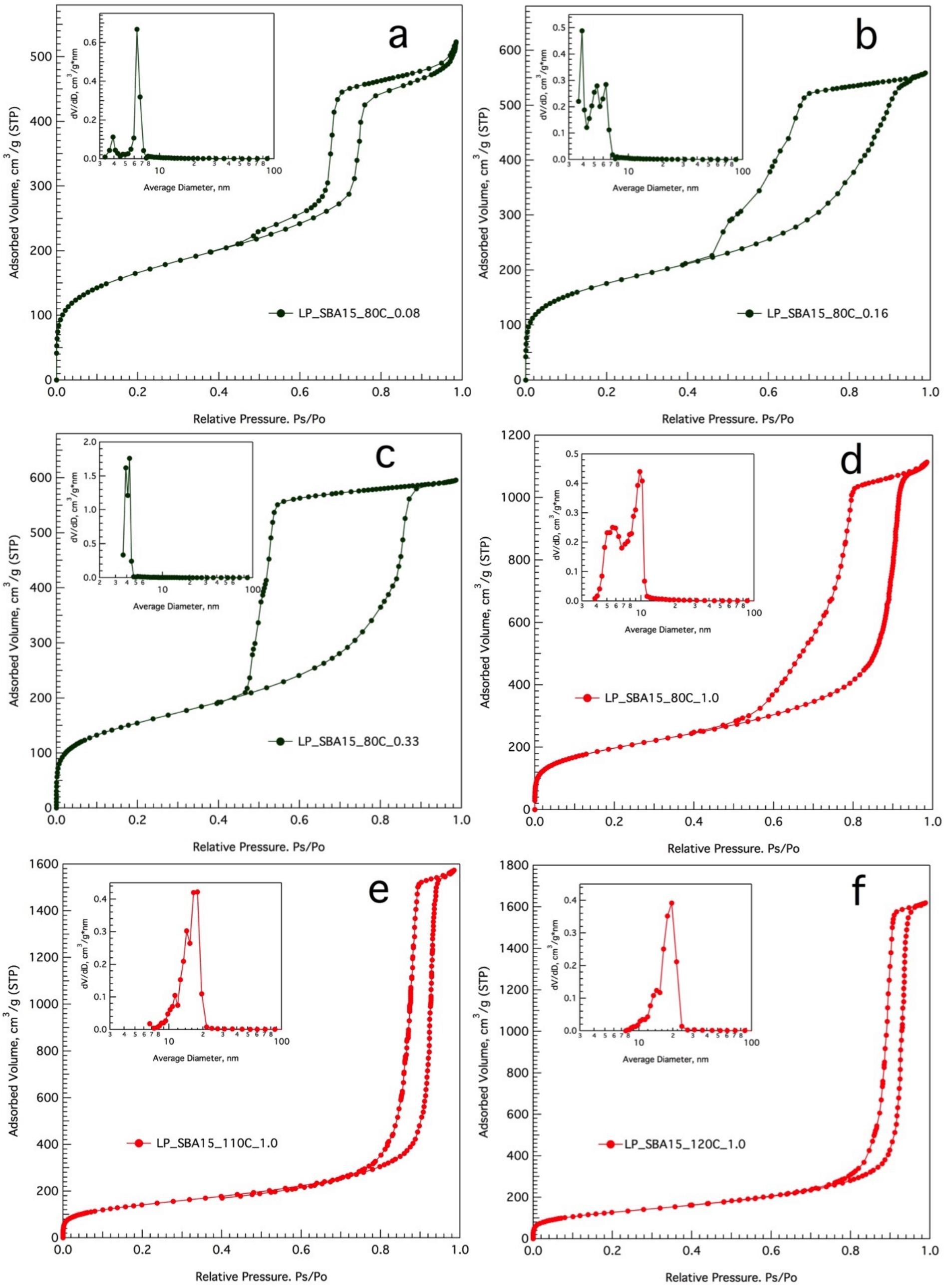

Figure 5.5: N_2 isotherms for a) LP-SBA15-80C-0.08; b) LP-SBA15-80C-0.16 and c) LP-SBA15-80C-0.33. Large pore silicas prepared at different temperature level: d) LP-SBA15-80C-1.0; e) LP-SBA15-110C-1.0 and f) LP-SBA15-120C-1.0. Inset graphs: BJH Pore volume distribution

After CeO_2 deposition on the silica substrate, the surface area and total pore volume are reduced for all samples. The smallest surface area

Sample	S_{BET}, m^2/g	V_{pore} cm^3/g	S_{red} %	V_{red} %
CeO_2-SBA15	373	0.58	52.2	29.6
CeO_2-LP-SBA15-80C-1.0	370	1.39	48.4	18.6
CeO_2-LP-SBA15-120C-1.0	352	1.79	24.1	28.3
CeO_2-LP-SBA15-80C-0.08	309	0.66	48.4	16.9

Table 5.2: Textural properties, surface area and pore volume reduction for CeO_2-LP-SBA15 composite materials

reduction of 24.1% is observed for CeO_2-LP-SBA15-120C-1.0 which had the largest pore diameter and volume, suggesting that the dimensions of the deposited ceria particles produce blocking and pore narrowing to a lesser extent. For the rest of the samples, the surface area reduction is about 50% and the total pore volume reduction is not consistent with the former. This possible over estimation of the pore volume could be due to the contribution of nitrogen adsorbed on the formed ceria particles and interparticle adsorption. Figure 5.6 shows the nitrogen adsorption and desorption isotherms for the composite ceria-silica materials and the large pore mesoporous precursor.

All materials keep a well-defined type IV isotherm and therefore keep the characteristic mesoporosity. All samples feature the previously mentioned regions on the isotherm curve. For CeO_2 deposited on pure siliceous and medium sized pore SBA-15 (TMB/P123 mass ratio equal to 0.08), the isotherm portion associated to micropore filling and monolayer formation is higher compared to CeO_2 deposited on silicas with higher amount of swelling agent. Past the relative pressure interval associated to multilayer formation, the inflection point at which capillary condensation occurs does not shift after ceria grafting, suggesting that the formed CeO_2 particles do not produce mesopore blocking or their average size is not comparable to that of the large pore support.

Concerning the hysteresis, all materials retain a type H1 loop which is almost parallel in a short P_S/P_0 range. For CeO_2/LP-SBA15-80-1.0 the hysteresis loop became narrower after ceria deposition due to a possible reduction of the pore capillary forces. The pore size distribution function for all solids exhibits a similar shape, which is indicative that all materials keep a monomodal pore size (Inset figures 5.6a-d). Nonetheless, all prepared catalytic supports possess surface areas well above those reported elsewhere for amorphous silica supported ceria or CeO_2/SiO_2 composites synthesized by sol-gel methodologies[41,86]

Figure 5.7 shows the Scanning Electron Microscopy graphs for all composite materials. After ceria loading, the morphology of the silica supports is not modified and no evidence of ceria clusters of significant size is observed. In

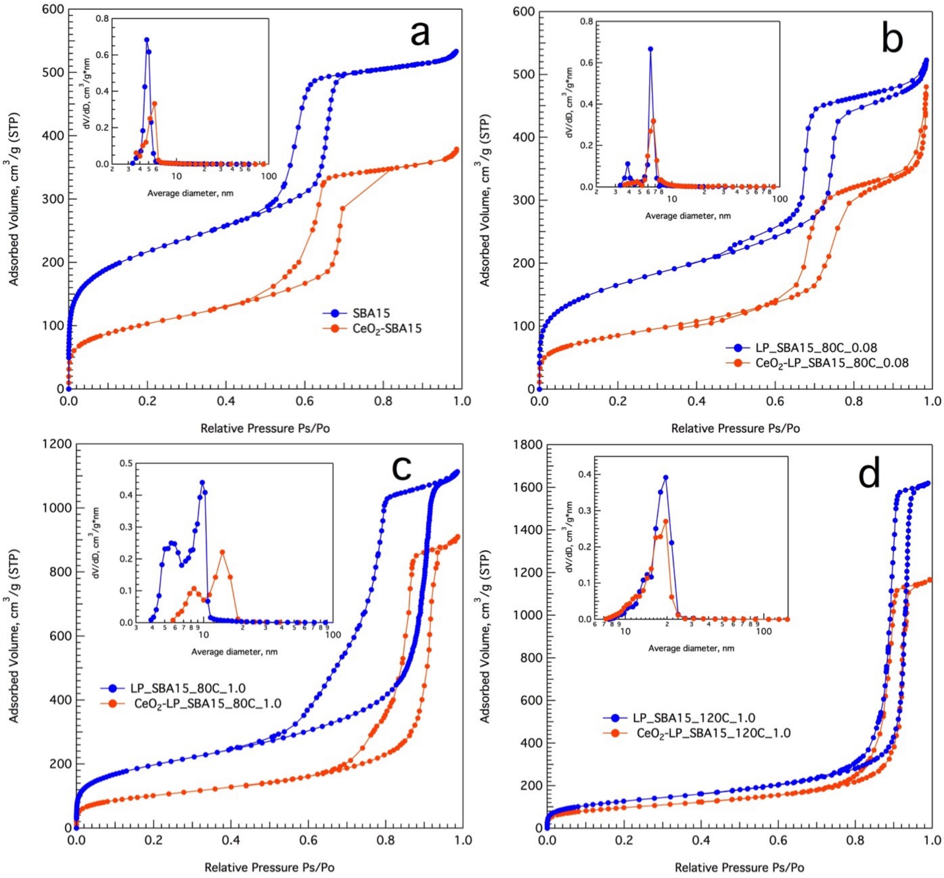

Figure 5.6: N_2 isotherms for CeO_2-LPSBA-15 composites: a) CeO_2-SBA15; b) CeO_2-LP-SBA15-80C-0.08; c) CeO_2-LP-SBA15-80C-1.0; d) CeO_2-LP-SBA15-120C-1.0. Inset graphs: BJH Pore volume distribution

agreement with the surface area results, it is possible to conclude that the deposited ceria particles do not compete in size with the diameter of the large pore mesoporous silica supports.

5.2.1 Ni/CeO_2SiO_2 for the ESR reaction

Based on the results obtained for the Ni/Ce-MCM-41 catalytic system (Chapter 5), ongoing research is currently being carried out to evaluate the catalytic activity of the same Ni catalyst over CeO_2/SiO_2 nanocomposites in the ethanol steam reforming reaction to produce hydrogen. The ethanol conversion, hydrogen yield and secondary products distribution will be compared in terms of the pore size to assess the possible role of diffusion and accessibility to the Ni active sites.

Two different kinds of cerium-promoted silicas (prepared by direct

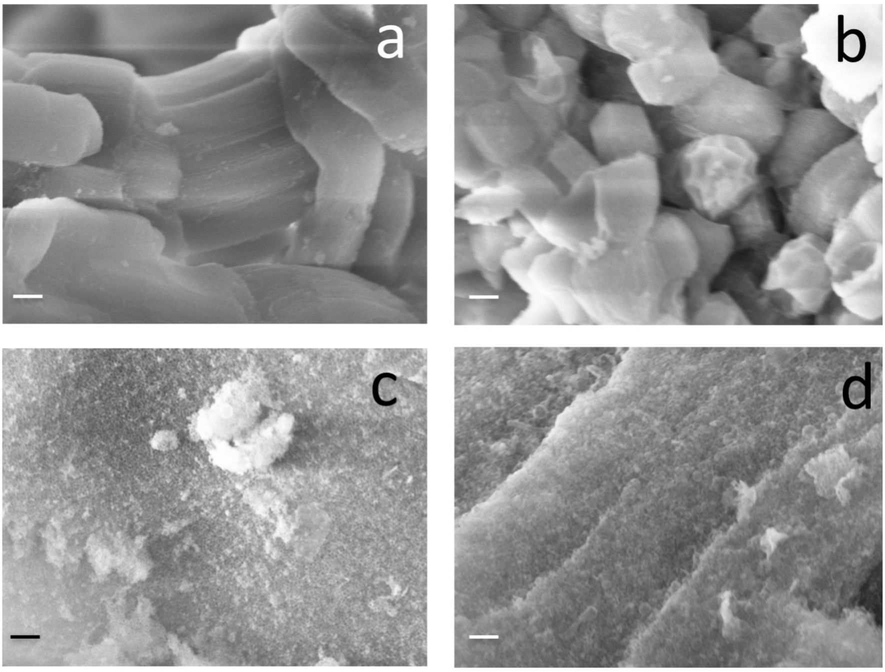

Figure 5.7: Scanning Electron Micrographs and particle morphology for: a) CeO_2-SBA15; b) CeO_2-LP-SBA15-80C-1.0; c) CeO_2-LP-SBA15-120C-1.0; d) CeO_2-LP-SBA15-80C-0.08 (Bar length 200nm, magnification 100kX)

isomorphic substitution of Ce and post synthesis ceria grafting) will be confronted to determine the synergy between the support and the active phase. Then, the most convenient grafting approach can be selected for the preparation of adequate catalytic supports that can find applications in the steam reforming of other hydrocarbons to produce hydrogen.

Chapter 6

Green synthesis of mesoporous silica

6.1 A geothermal waste as non-conventional Si precursor

6.1.1 Particle morphology and EDX spectroscopy

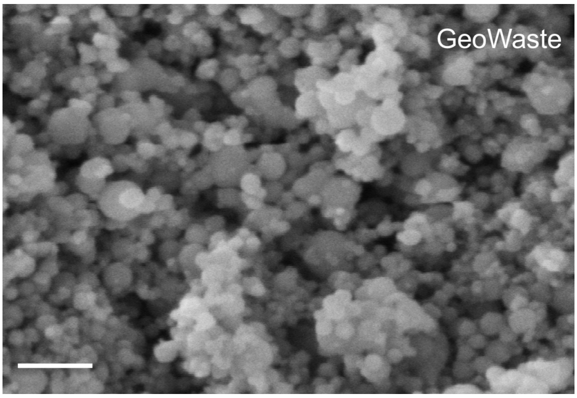

Figure 6.1: Scanning Electron Micrograph for the geothermal waste used as Si precursor (Bar length = 100nm, magnification 400kX)

Initial characterization of the geothermal waste was performed to assess its feasibility as adequate silicon precursor. Figure 6.1 shows the particle morphology for GeoWaste after being crushed, sieved (MESH 150) and washed with a 0.5M solution of HCl. The starting material consists of polydisperse round-like silica particles with variable sizes, ranging from 4 up to 30nm in diameter.

Elemental analysis was performed by means of Energy-dispersive X-ray spectroscopy. As-received geothermal silica is composed mainly of silicon dioxide (over 99.5%), with less than 0.5% of impurities, being the most abundant Al and Fe. After washing with HCl 0.5M the soluble species, which are presumably in the form of chlorides, (NaCl and KCl) are removed. For Al and Fe, the Si/Al and Si/Fe atomic ratios were 72.08 and 73.46. It is noteworthy that after acid treatment the amount of Al in the sample decreases (for a final value of 115.26), suggesting that dealumination of the silica matrix may be occurring. This phenomenon is well documented for aluminosilicates such as zeolites[101], and the extent of Al loss depends on the dealumination agent and the selected reaction conditions. On the other hand the abundance of Fe does not seem to change after HCl washing since the atomic ratio Si/Fe remains constant. The relative abundance of Si compared to O is consistent with tetra-coordinated silicon species in SiO_2.

6.1.2 Small Angle X-ray Scattering curves for mesoporous geothermal silica

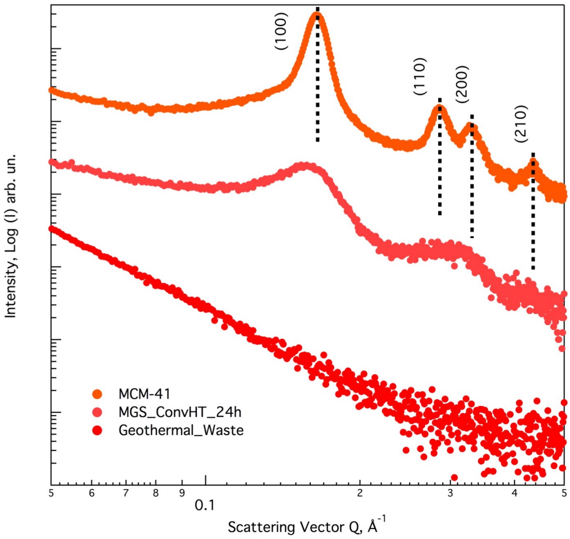

Figure 6.2: SAXS curves for mesoporous silica MCM-41; Mesoporous geothermal silica and the Geothermal Silica Waste, after calcination

Figure 6.2 shows the SAXS curves for the silicon precursor, the mesoporous silica sieve prepared with the geothermal waste under conventional hydrothermal synthesis and mesoporous MCM-41 synthesized using TEOS, in the low Q scattering vector interval from 0.05 to 0.05Å^{-1}. The as-received geothermal silica waste shows no diffraction peaks in the explored Q interval, suggesting that the sample is composed entirely of amorphous silicon dioxide. On the other hand, calcined mesoporous silica MCM-41 features a well-resolved scattering pattern, with a main diffraction peak centered at a reciprocal Q value of 0.165 Å^{-1}. Other secondary Bragg peaks are found at 0.286, 0.33 and 0.434Å^{-1}. These diffraction peaks can be indexed to the reflections of the (100), (110), (200) and (210) hlk planes for the hexagonal structure, space group $p6mm$[59]. The interplanar distance d_{100}, was calculated by interpolation using the Q values for these reflections. For a hexagonal structure, the lattice constant a_0, can be derived from the interplanar distance, as illustrated before. Table 6.1 summarizes the lattice parameters and interplanar distances, calculated for all prepared solids after calcination.

Sample	S_{BET}, m^2/g	V_{pore} cm^3/g	D_{pore}, nm	d_{100}[a]	a_0[a]
GeoWaste	45	0.22	n.d	0	0
MGS-MWHT-2[b]	617	0.73	4.7	43.3	50
MGS-MWHT-4[b]	546	0.69	4.45	43.7	50.5
MGS-MWHT-6[b]	707	0.7	3.97	44.8	51.7
MGS-ConvHT-24[b]	655	0.62	3.77	45.5	52.5
MCM-41-ConvHT-24[b]	923	0.79	3.47	44.8	51.2

Table 6.1: Textural properties and lattice cell parameters for the prepared mesoporous sieves using a geothermal waste as Si precursor. [a]Units are expressed in Å. [b]Refers to the overall hydrothermal synthesis time in hours

Mesoporous geothermal silica prepared under conventional hydrothermal synthesis (MGS-ConvHT-24h), features a main scattering peak that is slightly shifted to a lower reciprocal Q value of 0.159Å^{-1}, which results in a d_{100} spacing and a_0 constant of 45.5 and 52.5Å, respectively (compared to 44.8 and 51.2Å for pure siliceous MCM-41). The structural and lattice parameters of template-based mesoporous silica depend entirely on the length of the surfactant alkylic chain[61] and in the absence of co-solvents or co-surfactants, the closely obtained parameters are in agreement with previously reported values for mesoporous MCM-41[35]. For MGS-ConvHT-24, a second broad scattering peak with a maximum intensity on Q = 0.16Å^{-1} can be interpreted as the convolution of the (110) and (200) peaks. Finally, the least-resolved Bragg peak could be assigned to the scattering of the (210) plane for the hexagonal structure.

Figure 6.3 shows the SAXS curves for the samples prepared under microwave-assisted hydrothermal synthesis. In a similar fashion, all prepared sieves feature a main Bragg diffraction peak with secondary less-resolved peaks at higher Q values. A sample prepared under the longest irradiation time (MGS-MWHT-6h), exhibits an interplanar distance and lattice constant value that are the closest to that of the parent MCM-41 material (Table 6.1, d_{100} and a_0 columns). Although the position of the main scattering peak does not shift significantly, its intensity seems to increase with the hydrothermal synthesis time. Nonetheless, the microwave-assisted solvothermal methodology here reported enables

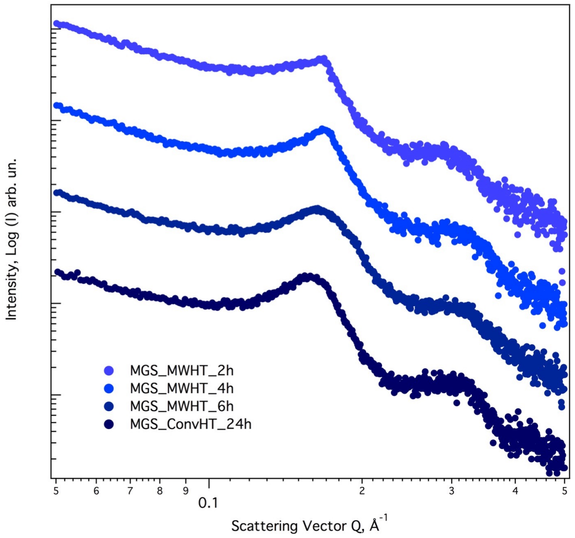

Figure 6.3: SAXS curves for several mesophases of silica prepared under different hydrothermal reaction times

ordered mesophases in a fraction of the typically required conventional hydrothermal synthesis time[8].

To improve the hexagonal ordering of the prepared mesoporous silicas and to better understand the formation mechanism, SAXS curves were recorded in liquid solvent for the synthesis colloid before ageing and hydrothermal treatment. Figure 6.4a shows the scattering curve for the precursor colloid using TEOS as Si source with the following molar composition:

$1.0(CH_3CH_2O)_4Si : 0.30CTABr : 20NH_3 : 210H_2O$

Data was collected right after TEOS addition (total acquisition time, 1800s). From the scattering pattern, a possible formation mechanism for the hexagonal mesophase can be elucidated: Under the strong basic conditions (pH = 12.7) the alkoxide molecules are rapidly hydrolyzed an interact with the positively charged micelles which group in hexagonal domains. A main scattering peak is located at Q = 0.147Å^{-1}. This value shifts to 0.165Å^{-1} after calcination (Fig. 6.2) due to thermal contraction of the silica network. This structural contraction depends on the surfactant removal protocol[55]. From Bragg's law, the distance between two scattering centers can be estimated as 42.7Å. This value is comparable with the micellar radii recently reported[53] for CTABr/TEOS mixtures under basic conditions (molar ratio 1:1, pH = 10).

For the geothermal waste as Si precursor, the synthesis colloid had the following molar composition:

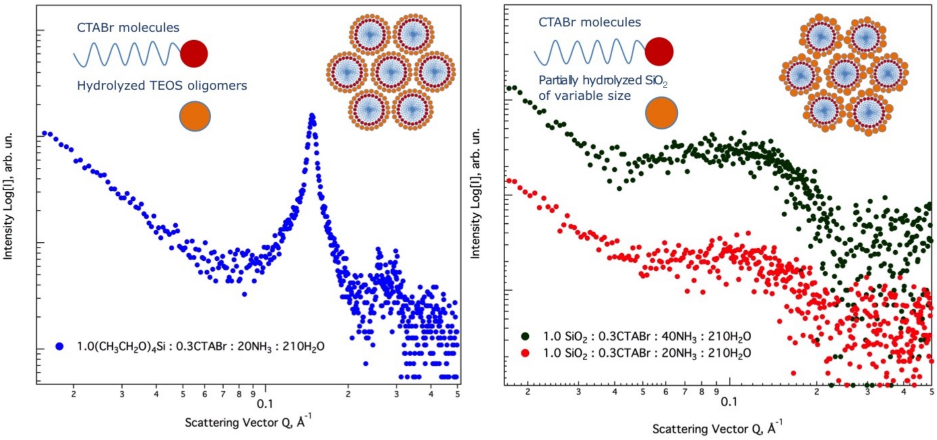

Figure 6.4: SAXS curves for the synthesis colloid using a) TEOS and b) geothermal silica waste as Si precursors

$1.0SiO_2 : 0.30CTABr : 20NH_3 : 210H_2O$.

Under identical acquisition conditions a broad curve can be observed (Fig. 6.4b), which suggests that the cationic micelles interact with the partially hydrolyzed Si particles of variable sizes and tend to group in less defined hexagonal structures. By increasing the amount of mineralizing agent by a twofold factor ($1.0SiO_2 : 40NH_3$), the center of the scattering curve does not change significantly (shifting from Q = 0.093 to 0.095Å^{-1}). Therefore, a reduced amount of NH_4OH solution as silica mineralizing agent was kept for all synthesis. The distance between scattering centers was estimated as 67.6 and 66Å and its value is consistent with micellar formations of thicker silica walls (compared to TEOS). For these materials, silica particles hydrolysis and consequent diffusion towards the positively charged micelles may be limited by their size. Nonetheless, after silica polymerization by microwave-assisted hydrothermal treatment, the obtained silica sieves feature hexagonal structures with d_{100} spacings comparable to the MCM-41 parent material. Inset figures 6.4a-b show a graphical representation of the possible micelle formation mechanism previously discussed.

6.1.3 Assessment of textural properties by N_2 physisorption

The textural properties for all prepared materials were evaluated by means of N_2 adsorption and desorption isotherms. Table 6.1 summarizes the Brunauer-Emmett-Teller surface area and pore volume for all calcined solids(S_{BET} and V_{pore} entries). The as received geothermal waste has a surface area of 45m^2/g whereas the highest area observed was 923m^2/g for MCM-41. For the mesoporous geothermal silica series, the surface area can be tailored in the interval from 550 to 700m^2/g, depending on the overall hydrothermal treatment time. In a similar manner, the largest total pore volume (evaluated at a relative pressure of $P_S/P_0 = 0.9814$) was 0.79cm^3/g for MCM-41 while pore capacity increased from 0.22 up to 0.73cm^3/g, for the geothermal waste after solvothermal synthesis. For the sake of time and energy savings, no longer microwave-assisted synthesis times were explored beyond 6h.

Figure 6.5a-f shows the adsorption and desorption isotherm curves for all calcined mesoporous materials whereas inset figures show the pore volume distribution obtained with the desorption branch of the isotherm and the Barrett-Joyner-Halenda model. The starting material GeoWaste features a type II isotherm according to the classification made by IUPAC[97], which is characteristic of macroporous adsorbents.

For the mesoporous silica series all materials exhibit a type IV(b) isotherm which is characteristic of substrates with pore sizes up to 50nm. Four well-defined portions in the isotherm curve can be described: a) Micropore filling and monolayer formation occur at very low P_S/P_0 values (up to 0.03), denoted by a relatively large nitrogen uptake. For GeoWaste the monolayer capacity was the lowest observed; b) Unrestricted multilayer formation is distinguished by an inflection point and slope change, followed by linear region in the isotherm curve; c) Nitrogen capillary condensation within the mesopores is identified by the presence of a second inflection point at relative pressure values close to 0.3 followed by a significant amount of adsorbed nitrogen. Such feature is not present in the geothermal waste. For MCM-41 a sharp steep is observed whereas the geothermal silicas exhibit a smooth slope. Finally, d) Inter particle adsorption is denoted by a final saturation plateau at high relative pressure areas (over $P_S/P_0 = 0.94$).

Concerning the Barrett-Joyner-Halenda graphs, the silicon precursor shows a broad pore size distribution with no average pore size. For the rest of the prepared materials, a narrow pore size distribution is observed, indicative of a monomodal distribution of pores with cylindrical geometry and open endings. An average pore diameter was calculated as $D_{pore} = 4*V_{pore}/S_{BET}$ (Table 6.1 D_{pore} entry). As the hydrothermal synthesis time increases, the pore size tends to narrow from 4.7 to 3.47nm (for MCM-41), suggesting that longer synthesis times favor irreversible silica polymerization and micelle packing into narrower and elongated worm-like structures. A similar phenomenon was described in terms of micelle concentration for CTABr/NaSal solutions[27]. Such variation in pore size results in a small width type H1 hysteresis loop for samples prepared after 2, 4 and 6h of solvothermal treatment. MGS-ConvHT-24h and MCM-41

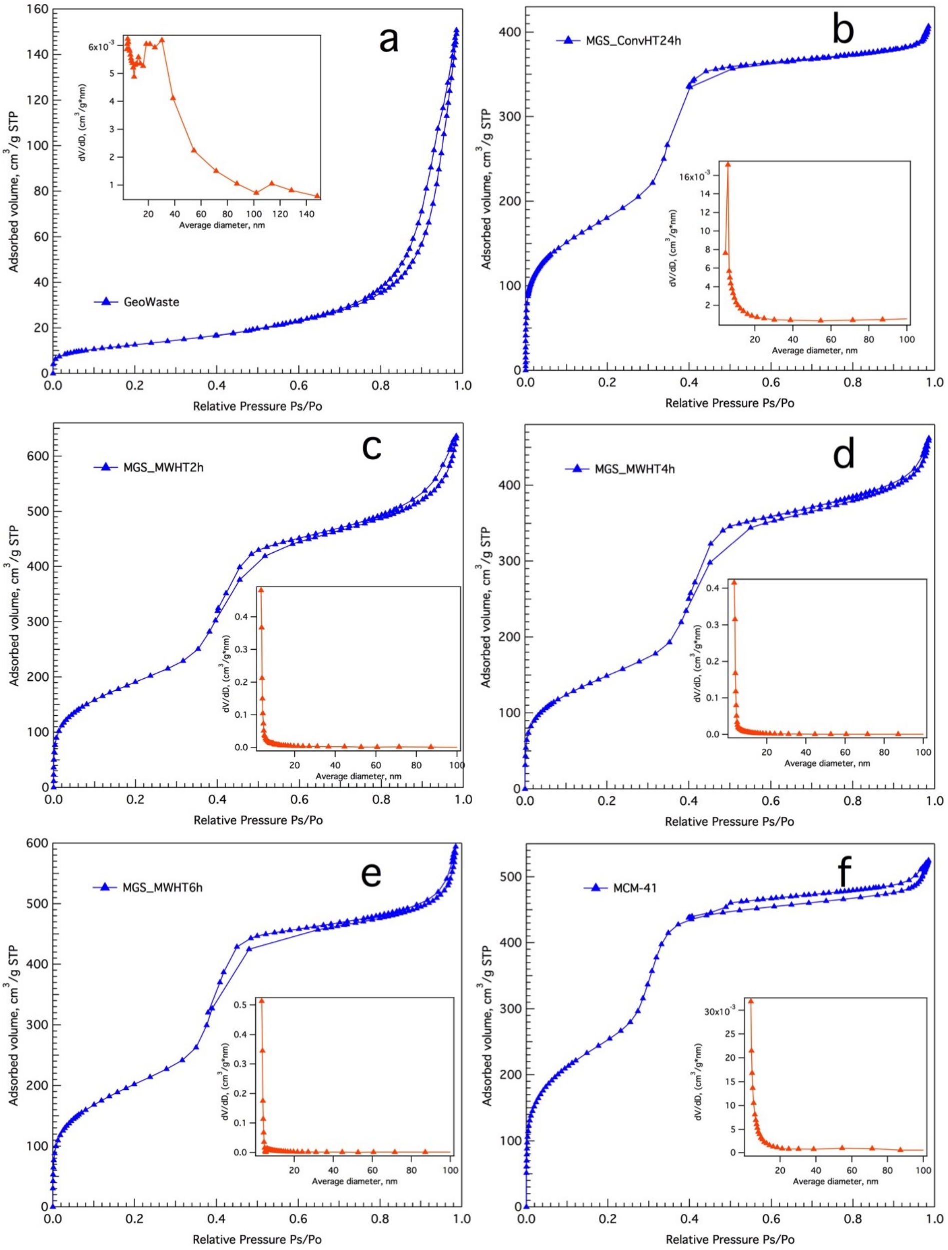

Figure 6.5: Nitrogen adsorption and desorption isotherms for: a) GeoWaste, b) MGS-ConvHT-24, c) MGS-MWHT-2, d) MGS-MWHT-4, e) MGS-MWHT-6 and f) MCM-41. Inset figures: BJH pore size distribution curves

feature the smallest pore diameter and an almost reversible isotherm curve. For MCM-41 a parallel loop over a long interval of relative pressure may be associated to particle aggregate adsorption rather than capillary effects[97].

6.1.4 ^{29}Si and ^{1}H MAS-NMR Spectroscopy

Nuclear magnetic resonance spectroscopy provided additional information concerning the structural environment of two nuclei in the silicon sieve. Figure 6.6a-b show the ^{29}Si and ^{1}H MAS-NMR spectra for the geothermal waste as starting material and the hexagonally ordered mesoporous silicate.

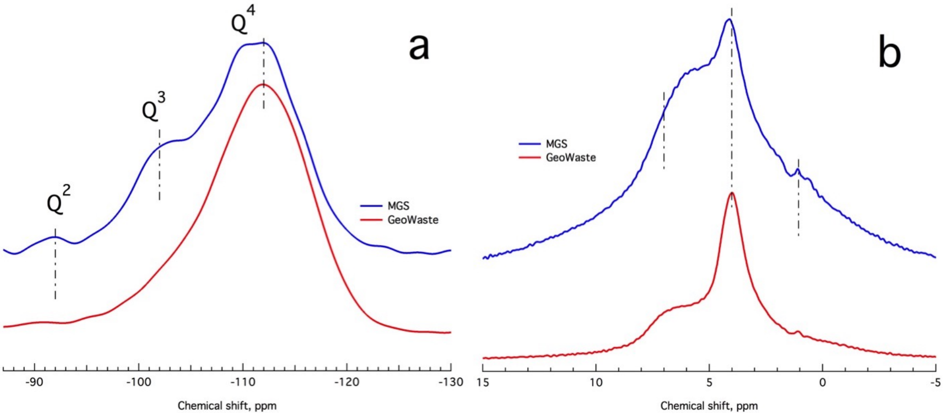

Figure 6.6: a) ^{29}Si and b) ^{1}H solid-state HP-DEC MAS-NMR spectra for the geothermal waste and the mesoporous geothermal silica samples

The as-received geothermal waste has a sole broad spectral signal with a maximum at -112ppm (using TMS as standard) that is indicative of Q^4 siloxane species. For the mesoporous sieve, two other crests are observed at around -102 and -92 ppm. These signals are typically associated to the resonances of Q^3 and Q^2 nuclei which belong to isolated and geminal silanol groups (Si(OH) and $Si(OH)_2$ surface groups).

Sample	Q^4	Q^3	Q^2	$(Q^2+Q^3)/Q^4$
GeoWaste	5.56	0.6	0	0.11
MGS	4.57	1.49	0.09	0.34

Table 6.2: Q^n distributions for the Si species in GeoWaste and MGS calcined samples

In order to obtain individual information of the Si nuclei in the structure, deconvolution of these signals was performed around the chemical shift values of -112, -102 and -92ppm, for Q^4, Q^3 and Q^2 species. Table 6.2 summarizes the Q^n distribution for both calcined solids. After hydrothermal synthesis, the relative amount of total-silanol/siloxane $((Si(OSi)_3OH)+Si(OSi)_2(OH)_2)/(Si(OSi)_4)$ ratio increased from 0.11 to 0.34. A higher recurrence of silanol groups could be indicative of a material with improved surface reactivity since silanol are considered as catalytic Bronsted sites and the Si-OH moiety is particularly important for surface functionalization or grafting of these silicates[75,122].

The ^{1}H NMR spectra further confirm the surface silanol enrichment for mesoporous geothermal silica (Fig 6.6b). For both samples, a main signal can be found at 4ppm chemical shift, that can be associated to physisorbed water on the surface of the material. After hydrothermal synthesis, a broadening of the signal around 7ppm could be indicative of a material with a larger number of both single and geminal Si-OH groups[100].

6.1.5 Scanning Electron Microscopy

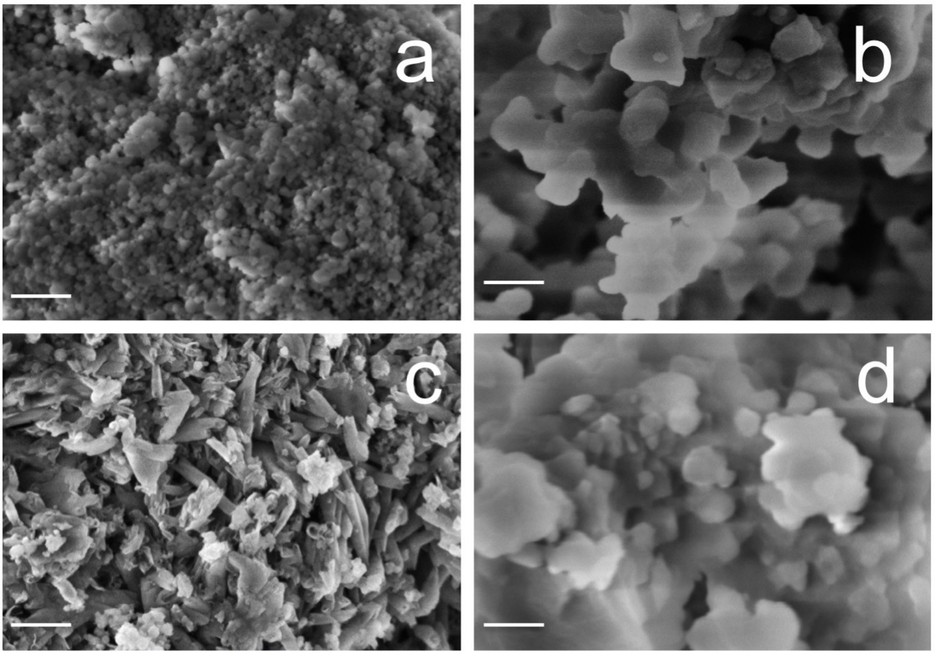

Figure 6.7: SEM Micrographs for: (a) Geothermal waste; (b) MGS-ConvHT24h; (c) MGS-MWHT-6h and (d) MCM-41 (Bar length = 200nm, magnification 200kX for all micrographs)

Figure 6.7 shows the SEM micrographs for calcined samples. After hydrothermal treatment, the resulting materials change from spherical particles to a flake-like morphology, which is characteristic of mesoporous silica MCM-41 (6.7d). For the sample prepared under microwave-assisted solvothermal synthesis (6.7c), tubular particles of variable length were observed which may be triggered by the use of microwaves irradiation for thermal activation and a more uniform heating profile. This particular morphology has been described for halloysite minerals[52] and can be typically associated to silica with low Fe content.

6.2 Glycerol carbonylation over mesoporous geothermal silica-supported Zn catalysts

To determine the feasibility of the mesoporous geothermal silicas as catalytic support, a Zn catalyst was prepared for the synthesis of glycerol carbonate in a solventless approach. Microwaves irradiation was used for thermal activation since glycerol features a higher loss tangent ($d_{\mathrm{Glycerol}} = 0.651$), than that of water at the standard MW frequency of 2.45GHz ($d_{\mathrm{Water}} = 0.231$). Therefore, temperatures as high as 160°C can be achieved within a couple of minutes of MW irradiation. Figure 6.8 shows a typical temperature profile for the solventless conversion of glycerol. The MW source supplies 80% of a 240W maximum power during two minutes; After the desired temperature is reached, a PID controller keeps a smooth MW output between 25 and 35% of the total power. Given the dielectric properties of the reaction medium, and the MW response of the solvent, a more efficient temperature profile and fast heating can be accomplished.

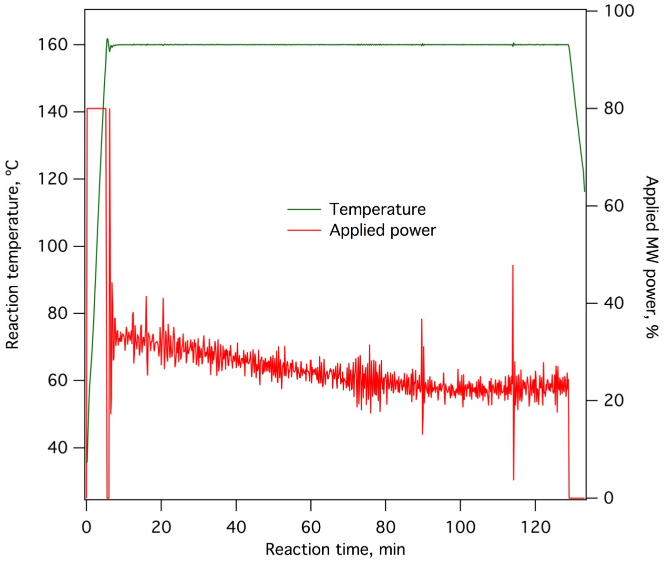

Figure 6.8: Temperature profile for the glycerol carbonate synthesis over Zn/MGS-MWHT-4h after 120 minutes of reaction time. (Reaction temperature = 160°C)

Table 6.2 summarizes the reaction conditions, molar ratios for glycerol and urea, glycerol carbonate yield and glycerol conversion for selected samples of Zn/MGS catalysts. The Glycerol conversion was calculated in terms of the converted mol of glycerol as follows:

$$X_{Glycerol} = \frac{n^{in}_{C_3H_8O_3} - n^{out}_{C_3H_8O_3}}{n^{in}_{C_3H_8O_3}} * 100 \tag{6.1}$$

On the other hand, glycerol carbonate yield was calculated considering glycerol as the limiting reactant, in terms of the converted mol of glycerol:

$$Y_{C_4H_6O_4} = \frac{n_{C_4H_6O_4}}{n^{in}_{C_3H_8O_3} - n^{out}_{C_3H_8O_3}} \tag{6.2}$$

Glycerol carbonylation was initially carried out at 160°C, following a previously reported methodology[57]. For the Zn/MGS catalyst, the highest glycerol conversion was 60% with a glycerol carbonate yield of 0.18; By increasing the amount of urea by a twofold factor, the selectivity was doubled but the glycerol conversion only increased marginally (for a final value of 65% after 2h of reaction time).

To further explore the activity of the Zn/MGS catalyst, the glycerol carbonate synthesis was performed at 140°C and two different urea/glycerol molar ratios. The highest conversion value for the series of catalytic supports obtained was 77% (at 140°C and 1:1 molar ratio). For a molar ratio of 1:1.5 (urea/glycerol), the glycerol carbonate yield was increased again by a twofold factor and the conversion was kept above 70%.

Catalyst	T[a]	[CH_4N_2O][b]	[$C_3H_8O_3$][b]	Yield[c]	Conversion[d]
Zn-MGS-MWHT-4h	140	0.2	0.2	0.18	77%
Zn-MGS-MWHT-4h	140	0.3	0.2	0.33	71%
Zn-MGS-MWHT-4h	160	0.2	0.2	0.18	60%
Zn-MGS-MWHT-4h	160	0.4	0.2	0.37	64%

Table 6.3: Reaction parameters, yield and conversion percentage for the carbonylation of glycerol over mesoporous geothermal silica-supported Zn catalysts. [a]Reaction temperature in °C, [b]Concentrations are expressed in mmol units, [c]Glycerol carbonate yield as mol/mol, [d]Glycerol conversion expressed in terms of the initial load.

Figure 6.9 shows the glycerol conversion for Zn/MGS-MWHT-4h compared to the same catalyst over hexagonally ordered mesoporous MCM-41, as a function of the reaction time (reaction temperature, 160°C). After 60min a total glycerol conversion of 60% was reached and it remained unchanged for another 60min of reaction time. For MCM-41, the highest conversion value of 72% was reached (comparable to the results published elsewhere[57]). Therefore, the MW heating approach enabled the reduction of the overall synthesis time due to the adequate MW response of glycerol as solvent (6h for conventional heating). Although with a lower glycerol conversion, the Zn/MGS catalyst showed good hydrothermal stability and more importantly the Al, and Fe impurities do not catalyze undesired side-reactions.

These obtained results confirm the usability of the prepared catalytic supports and enable the use of the geothermal silica waste as a cheap and abundant Si precursor for the preparation of other type of self-assembled silicon-based structures

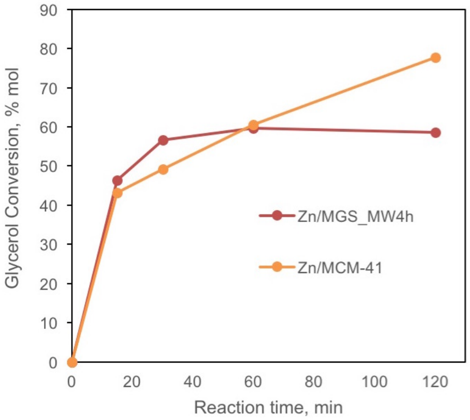

Figure 6.9: Glycerol conversion and glycerol carbonate yield for Zn/MCM-41 and Zn/MGS-MWHT-4h after 120 minutes of reaction time

Part V

Conclusions

Conclusions and future outlook

A series of mesoporous silicon-based nanostructured materials were successfully prepared by an adequate control of the synthesis parameters governing their soft-template hydrothermal synthesis. By coupling innovative approaches such as ultrasounds for micromixing and microwaves irradiation for thermal activation, cerium-promoted mesoporous silicas were prepared by two different strategies: Direct isomorphic substitution of Ce within the hexagonal framework and post-synthesis grafting of mesoporous silica of variable pore size.

Cerium incorporation on MCM-41 was achieved by ultrasound assisted direct hydrothermal synthesis. Depending on the Ce/Si molar ratios in the synthesis colloid, two different Ce incorporation mechanisms were observed: isomorphic substitution in the silica network and condensation in extra framework clusters. The sonochemical methodology enhanced cerium dispersion along the hexagonal framework and preserved the ordering even at high Ce/Si molar ratios. Further, the use of a coaxial applicator for in-situ microwave irradiation allowed the reduction of the hydrothermal synthesis time while preserving the hexagonal structure and achieving a higher surface area compared to materials prepared under hydrothermal synthesis by conventional heating.

The use of US coupled with MW irradiation for thermal activation represents an innovative approach that can be implemented for other types of solvothermal synthesis based on the use of amphiphilic molecules. The cerium-modified materials exhibit high surface areas and were tested as catalytic supports. The catalytic activity of the Ni/xCe-MCM-41 catalyst was evaluated in the ethanol steam reforming reaction to produce hydrogen. Cerium promoted silica resulted in a better catalytic support for the ESR reaction compared to the bare MCM-41, since complete ethanol conversion, high H_2 selectivity were achieved and no catalyst deactivation occurred. The presence of the heteroatom in the mesoporous sieve modified the morphology and chemical behavior of the catalyst, resulting in an ordered deposition of carbon nano-filaments that do not induce catalyst deactivation.

To analyze the kinetics and diffusive effects on the ESR reaction, a series of ceria-silica composite materials were prepared by post-grafting mesoporous SBA-15 of variable pore size. Large pore silica sieves were prepared by solvothermal methodology using a non-ionic triblock copolymer as soft-template and trimethylbenzene as swelling agent. By modifying the TMB/Pluronic P123 mass ratio and the solvothermal ageing temperature, it is possible to obtain hexagonally ordered mesophases in the pore size interval from 4 to 20nm. Selected samples were used as support for the preparation of CeO_2/SiO_2 composites. Acoustic cavitation by means of ultrasounds was used for micromixing and ceria dispersion, using a precipitating agent under wet-impregnation conditions. The surface grafting methodology enabled the formation of well-dispersed CeO_2 particles that do not match the pore size and therefore do not produce pore blocking. All materials kept mesoporosity, pore geometry and high surface areas after ceria deposition. These materials will be used as a Ni catalytic support for the ESR reaction to analyze the pore size effect on the active phase and its effect on the main products distribution.

Lastly, a green integrated microwave-assisted hydrothermal synthesis for the preparation of mesoporous silica using a non-conventional silicon source was disclosed. This novel methodology revalorizes a geothermal waste, allowing the synthesis of ordered silicas with energy savings. By means of a coaxial applicator for in-situ MW irradiation, it is possible to tune the textural properties and hexagonal ordering of mesoporous solids. The total surface area was increased by a tenfold factor (Referring to the starting waste material). The microwave hydrothermal synthesis resulted in shorter reaction times, compared to conventional heating. The prepared materials were used in the solventless conversion of glycerol to glycerol carbonate using Zn as active phase, to demonstrate their usability as catalytic support. The glycerol conversion was comparable to that reported elsewhere and the impurities of the material do not hinder its catalytic activity nor do they catalyze other side-reactions.

In conclusion, the design of soft-synthesis methodologies for the preparation of silicon-based structures as catalytic supports can be enhanced greatly by coupling non conventional approaches for mixing, thermal activation and sustainable green precursors. The developed methodologies can be also applied to the preparation of other types of template-based materials such as zeolites or zeotypes or metal-modified mesoporous solids. The integrated green methodology we propose, enables the realistic projection of a sustainable large-scale industrial process to synthesize mesoporous molecular sieves by making use of a cheap and readily available geothermal silicon precursor.

Bibliography

[1] Akbay, C., Gill, N. L., Powe, A., and Warner, I. M. Monomeric and polymeric anionic gemini surfactants and mixed surfactant systems in micellar electrokinetic chromatography. Part I: Characterization and application as novel pseudostationary phases. *Electrophoresis 26*, 2 (2005), 415–425.

[2] Akondi, A. M., Trivedi, R., Sreedhar, B., Kantam, M. L., and Bhargava, S. Cerium-containing MCM-41 catalyst for selective oxidative arene cross-dehydrogenative coupling reactions. *Catal. Today 198*, 1 (dec 2012), 35–44.

[3] Antonakou, E., Lappas, A., Nilsen, M. H., Bouzga, A., and Stöcker, M. Evaluation of various types of Al-MCM-41 materials as catalysts in biomass pyrolysis for the production of bio-fuels and chemicals. *Fuel 85*, 14-15 (oct 2006), 2202–2212.

[4] Askari, S., Miar Alipour, S., Halladj, R., and Davood Abadi Farahani, M. H. Effects of ultrasound on the synthesis of zeolites: A review. *J. Porous Mater. 20*, 1 (2013), 285–302.

[5] Aydin, F., Chu, X., Uppaladadium, G., Devore, D., Goyal, R., Murthy, N. S., Zhang, Z., Kohn, J., and Dutt, M. Self-Assembly and Critical Aggregation Concentration Measurements of ABA Triblock Copolymers with Varying B Block Types: Model Development, Prediction, and Validation. *J. Phys. Chem. B 120*, 15 (2016), 3666–3676.

[6] Bagshaw, S. a., and Testa, F. Wairakei geothermal silica, a low cost reagent for the synthesis of mesostructured M41S alumino-silicate molecular sieves. *Microporous Mesoporous Mater. 39*, 1-2 (sep 2000), 67–75.

[7] Bagshaw, S. a., and Testa, F. Wairakei geothermal silica; a low cost reagent for the synthesis of low, intermediate- and high-silica zeolites. *Microporous Mesoporous Mater. 42*, 2-3 (feb 2001), 205–217.

[8] Beck, J. S., Vartuli, J. C., Roth, W. J., Leonowicz, M. E., Kresge, C. T., Schmitt, K. D., Chu, C. T. W., Olson, D. H., and Sheppard, E. W. A new family of mesoporous molecular sieves prepared with liquid crystal templates. *J. Am. Chem. Soc. 114*, 27 (dec 1992), 10834–10843.

[9] Blanton, T. N., Rajeswaran, M., Stephens, P. W., Whitcomb, D. R., Misture, S. T., and Kaduk, J. a. Crystal structure determination of the silver carboxylate dimer [Ag(O2C22H43)]2, silver behenate, using powder X-ray diffraction methods. *Powder Diffr. 26*, 04 (mar 2012), 313–320.

[10] Bui, T. X., Kang, S.-Y., Lee, S.-H., and Choi, H. Organically functionalized mesoporous SBA-15 as sorbents for removal of selected pharmaceuticals from water. *J. Hazard. Mater. 193* (oct 2011), 156–63.

[11] Builes, S., López-Aranguren, P., Fraile, J., Vega, L. F., and Domingo, C. Alkylsilane-functionalized microporous and mesoporous materials: Molecular simulation and experimental analysis of gas adsorption. *J. Phys. Chem. C 116*, 18 (2012), 10150–10161.

[12] Calles, J., Carrero, a., and a.J. Vizcaíno. Ce and La modification of mesoporous CuNi/SBA-15 catalysts for hydrogen production through ethanol steam reforming. *Microporous Mesoporous Mater. 119*, 1-3 (mar 2009), 200–207.

[13] Calvino-Casilda, V., Mul, G., Fernández, J. F., Rubio-Marcos, F., and Bañares, M. A. Monitoring the catalytic synthesis of glycerol carbonate by real-time attenuated total reflection FTIR spectroscopy. *Appl. Catal. A Gen. 409-410* (2011), 106–112.

[14] Campbell, C. T., and Peden, C. H. F. Chemistry. Oxygen vacancies and catalysis on ceria surfaces. *Science 309*, 5735 (jul 2005), 713–4.

[15] Cao, L., Man, T., and Kruk, M. Synthesis of ultra-large-pore SBA-15 silica with two-dimensional hexagonal structure using triisopropylbenzene as micelle expander. *Chem. Mater. 21* (2009), 1144–1153.

[16] Carbajal Ramos, I. A., Montini, T., Lorenzut, B., Troiani, H., Gennari, F. C., Graziani, M., and Fornasiero, P. Hydrogen production from ethanol steam reforming on M/CeO2/YSZ (M = Ru, Pd, Ag) nanocomposites. *Catal. Today 180*, 1 (jan 2012), 96–104.

[17] Casanovas, A., Roig, M., de Leitenburg, C., Trovarelli, A., and Llorca, J. Ethanol steam reforming and water gas shift over Co/ZnO catalytic honeycombs doped with Fe, Ni, Cu, Cr and Na. *Int. J. Hydrogen Energy 35*, 15 (aug 2010), 7690–7698.

[18] Chandler, D. Interfaces and the driving force of hydrophobic assembly. *Nature 437*, 7059 (2005), 640–647.

[19] Chen, C., Kim, J., and Ahn, W. S. CO2capture by amine-functionalized nanoporous materials: A review. *Korean J.*

Chem. Eng. 31, 11 (2014), 1919–1934.

[20] Chen, G., Guo, C.-Y., Zhang, X., Huang, Z., and Yuan, G. Direct conversion of syngas to ethanol over Rh/Mn-supported on modified SBA-15 molecular sieves: Effect of supports. *Fuel Process. Technol. 92*, 3 (mar 2011), 456–461.

[21] Chen, Y. L., Chen, S., Frank, C., and Israelachvili, J. Molecular mechanisms and kinetics during the self-assembly of surfactant layers. *J. Colloid Interface Sci. 153*, 1 (1992), 244–265.

[22] Chiang, W.-S., Fratini, E., Baglioni, P., Chen, J.-H., and Liu, Y. Pore Size Effect on Methane Adsorption in Mesoporous Silica Materials Studied by Small-Angle Neutron Scattering. *Langmuir 32*, 35 (2016), 8849–8857.

[23] Chiang, W. S., Fratini, E., Baglioni, P., Georgi, D., Chen, J. H., and Liu, Y. Methane Adsorption in Model Mesoporous Material, SBA-15, Studied by Small-Angle Neutron Scattering. *J. Phys. Chem. C 120*, 8 (2016), 4354–4363.

[24] Cintas, P., Tagliapietra, S., Calcio Gaudino, E., Palmisano, G., and Cravotto, G. Glycerol: a solvent and a building block of choice for microwave and ultrasound irradiation procedures. *Green Chem. 16*, 3 (2014), 1056.

[25] Cordero, B., Gómez, V., Platero-Prats, A. E., Revés, M., Echeverría, J., Cremades, E., Barragán, F., and Alvarez, S. Covalent radii revisited. *Dalt. Trans.*, 21 (2008), 2832–2838.

[26] Cui, X., Mao, S., Liu, M., Yuan, H., and Du, Y. Mechanism of Surfactant Micelle Formation. *Langmuir 24*, August (2008), 10771–10775.

[27] Das, N. C., Cao, H., Kaiser, H., Warren, G. T., Gladden, J. R., and Sokol, P. E. Shape and size of highly concentrated micelles in CTAB/NaSal solutions by small angle neutron scattering (SANS). *Langmuir 28*, 33 (2012), 11962–11968.

[28] Deng, Y. H., Wei, J., Sun, Z. K., and Zhao, D. Y. Large-pore ordered mesoporous materials templated from non-Pluronic amphiphilic block copolymers. *Chem. Soc. Rev. 42*, 9 (2013), 4054–4070.

[29] Fang, Z., L. Smith Jr., R., and Qi, X. *Production of Biofuels and Chemicals with Microwave*, vol. 3. Springer Dordrecht Heidelberg New York London, 2015.

[30] Feng, R.-m., Yang, X.-j., Ji, W.-j., and Au, C.-T. Hydrothermal synthesis of stable mesoporous ZrO2Y2O3 and CeO2ZrO2Y2O3 from simple inorganic salts and CTAB template in aqueous medium. *Mater. Chem. Phys. 107*, 1 (jan 2008), 132–136.

[31] Fu, Y., Wu, Y., Cai, W., Yue, B., and He, H. Promotional effect of cerium on nickel-containing mesoporous silica for carbon dioxide

reforming of methane. *Sci. China Chem. 58*, 1 (2015), 148–155.

[32] García-Diéguez, M., Finocchio, E., Larrubia, M. Á., Alemany, L. J., and Busca, G. Characterization of alumina-supported Pt, Ni and PtNi alloy catalysts for the dry reforming of methane. *J. Catal. 274*, 1 (aug 2010), 11–20.

[33] Gérardin, C., Reboul, J., Bonne, M., and Lebeau, B. Ecodesign of ordered mesoporous silica materials. *Chem. Soc. Rev. 42*, 9 (2013), 4217.

[34] González-Rivera, J., Galindo-Esquivel, I. R., Onor, M., Bramanti, E., Longo, I., and Ferrari, C. Heterogeneous catalytic reaction of microcrystalline cellulose in hydrothermal microwave-assisted decomposition: effect of modified zeolite Beta. *Green Chem. 16*, 3 (2014), 1417–1425.

[35] González-Rivera, J., Tovar-Rodríguez, J., Bramanti, E., Duce, C., Longo, I., Fratini, E., Galindo-Esquivel, I. R., and Ferrari, C. Surfactant recovery from mesoporous metal-modified materials (Sn, Y, Ce, SiMCM-41), by ultrasound assisted ion-exchange extraction and its re-use for a microwave in situ cheap and eco-friendly MCM-41 synthesis. *J. Mater. Chem. A 2*, 19 (2014), 7020.

[36] González Vargas, O., de los Reyes Heredia, J., Montesinos Castellanos, A., Chen, L., and Wang, J. Cerium incorporating into MCM-41 mesoporous materials for CO oxidation. *Mater. Chem. Phys. 139*, 1 (apr 2013), 125–133.

[37] González Vargas, O., de los Reyes Heredia, J., Wang, J., Chen, L., Montesinos Castellanos, A., and Llanos, M. Hydrogen production over Rh/Ce-MCM-41 catalysts via ethanol steam reforming. *Int. J. Hydrogen Energy 38*, 32 (oct 2013), 13914–13925.

[38] Goyal, P. S., and Aswal, V. K. Micellar structure and inter-micelle interactions in micellar solutions: Results of small angle neutron scattering studies. *Curr. Sci. 80*, 8 (2001), 972–979.

[39] Gude, V., Patil, P., Martinez-Guerra, E., Deng, S., and Nirmalakhandan, N. Microwave energy potential for biodiesel production. *Sustain. Chem. Process. 1*, 1 (2013), 5.

[40] Guevara, J., Wang, J., Chen, L., Valenzuela, M., Salas, P., García-Ruiz, A., Toledo, J., Cortes-Jácome, M., Angeles-Chavez, C., and Novaro, O. Ni/Ce-MCM-41 mesostructured catalysts for simultaneous production of hydrogen and nanocarbon via methane decomposition. *Int. J. Hydrogen Energy 35*, 8 (apr 2010), 3509–3521.

[41] Gulkova, D., and Vit, Z. Silica-ceria as support for the preparation of NiMo (P) hydrodesulfurization and hydrodenitrogenation catalysts. *Appl. Catal. A Gen. 125* (1995), 61–70.

[42] Haryanto, A., Fernando, S., Murali, N., and Adhikari, S. Current status of hydrogen production techniques by steam reforming of ethanol: A review. *Energy and Fuels 19*, 5 (2005), 2098–2106.

[43] He, R., Li, W., Deng, D., Chen, W., Li, H., Wei, C., and Tang, Y. Efficient removal of lead from highly acidic wastewater by periodic ion imprinted mesoporous SBA-15 organosilica combining metal coordination and co-condensation. *J. Mater. Chem. A 3*, 18 (2015), 9789–9798.

[44] Hines, J. D., Thomas, R. K., Garrett, P. R., Rennie, G. K., and Penfold, J. Investigation of Mixing in Binary Surfactant Solutions by Surface Tension and Neutron Reflection: Anionic/Nonionic and Zwitterionic/Nonionic Mixtures. *J. Phys. Chem. B 101*, 97 (1997), 9215–9223.

[45] Holmes, S. M., Zholobenko, V. L., Thursfield, A., Plaisted, R. J., Cundy, C. S., and Dwyer, J. In situ FTIR study of the formation of MCM-41. *J. Chem. Soc. Faraday Trans. 94*, 14 (1998), 2025–2032.

[46] Hu, Q., Li, J. J., Hao, Z. P., Li, L. D., and Qiao, S. Z. Dynamic adsorption of volatile organic compounds on organofunctionalized SBA-15 materials. *Chem. Eng. J. 149*, 1-3 (jul 2009), 281–288.

[47] Iliade, P., Miletto, I., Coluccia, S., and Berlier, G. Functionalization of mesoporous MCM-41 with aminopropyl groups by co-condensation and grafting: A physico-chemical characterization. *Res. Chem. Intermed. 38*, 3-5 (2012), 785–794.

[48] Jain, N., Trabelsi, S., Guillot, S., McLoughlin, D., Langevin, D., Letellier, P., and Turmine, M. Critical aggregation concentration in mixed solutions of anionic polyelectrolytes and cationic surfactants. *Langmuir 20*, 20 (2004), 8496–8503.

[49] Jankhah, S., Abatzoglou, N., Gitzhofer, F., Blanchard, J., and Oudghiri-Hassani, H. Catalytic properties of carbon nano-filaments produced by iron-catalysed reforming of ethanol. *Chem. Eng. J. 139*, 3 (jun 2008), 532–539.

[50] Jiang, S. P. Functionalized mesoporous structured inorganic materials as high temperature proton exchange membranes for fuel cells. *J. Mater. Chem. A 2*, 21 (2014), 7637.

[51] Jiang, T., Zhao, Q., Chen, K., Tang, Y., Yu, L., and Yin, H. Synthesis and characterization of Co (Ni or Cu)-MCM-41 mesoporous molecular sieves with different amount of metal obtained by using microwave irradiation method. *Appl. Surf. Sci. 254*, 9 (feb 2008), 2575–2580.

[52] Joussein, E., Petit, S., Churchman, J., Theng, B., Righi, D., and Delvaux, B. Halloysite clay minerals a review. *Clay Miner.*

40, 4 (2005), 383–426.

[53] Katryniok, B., Paul, S., Bellière-Baca, V., Rey, P., and Dumeignil, F. Glycerol dehydration to acrolein in the context of new uses of glycerol. *Green Chem. 12*, 12 (2010), 2079.

[54] Khayoon, M., and Hameed, B. Yttrium-grafted mesostructured SBA-3 catalyst for the transesterification of glycerol with methyl acetate to synthesize fuel oxygenates. *Appl. Catal. A Gen. 460-461* (jun 2013), 61–69.

[55] Klotz, M., Albouy, P. A., Ayral, A., Ménager, C., Grosso, D., Van Der Lee, A., Cabuil, V., Babonneau, F., and Guizard, C. The true structure of hexagonal mesophase-templated silica films as revealed by X-ray scattering: Effects of thermal treatments and of nanoparticle seeding. *Chem. Mater. 12*, 6 (2000), 1721–1728.

[56] Kolinko, P., Smirniotis, P., Kozlov, D., and a.V. Vorontsov. Cr modified TiO2-loaded MCM-41 catalysts for UV-light driven photodegradation of diethyl sulfide and ethanol. *J. Photochem. Photobiol. A Chem. 232* (mar 2012), 1–7.

[57] Kondawar, S. E., Potdar, A. S., and Rode, C. V. Solvent-free carbonylation of glycerol with urea using metal loaded MCM-41 catalysts. *RSC Adv. 5*, 21 (2015), 16452–16460.

[58] Kralova, I., and Sjöblom, J. Surfactants used in food industry: A review. *J. Dispers. Sci. Technol. 30*, 9 (2009), 1363–1383.

[59] Kresge, C. T., Leonowicz, M. E., Roth, W. J., Vartuli, J. C., and Beck, J. S. Ordered mesoporous molecular sieves synthesized by a liquid-crystal template mechanism. *Nature 359*, 6397 (1992), 710–712.

[60] Kresge, C. T., and Roth, W. J. The discovery of mesoporous molecular sieves from the twenty year perspective. *Chem. Soc. Rev. 42*, 9 (2013), 3663.

[61] Kruk, M., Jaroniec, M., and Sayari, A. Adsorption Study of Surface and Structural Properties of MCM-41 Materials of Different Pore Sizes. *J. Phys. Chem. B 101*, 4 (1997), 583–589.

[62] Kuo, S. W. Hydrogen bond-mediated self-assembly and supramolecular structures of diblock copolymer mixture. *Polym. Int. 58*, 5 (2009), 455–464.

[63] Laha, S., Mukherjee, P., Sainkar, S., and Kumar, R. Cerium Containing MCM-41-Type Mesoporous Materials and their Acidic and Redox Catalytic Properties. *J. Catal. 207*, 2 (apr 2002), 213–223.

[64] Li, D., Zeng, L., Li, X., Zhang, C., Wang, X., Ma, H., Assabumrungrat, S., and Gong, J. Ceria-promoted Ni/SBA-15 catalysts for ethanol steam reforming with enhanced activity and resistance to deactivation. *Appl. Catal. B Environ. 176-177* (2015),

532–541.

[65] Li, T., Senesi, A. J., and Lee, B. Small Angle X-ray Scattering for Nanoparticle Research. *Chem. Rev. 116*, 18 (2016), 11128–11180.

[66] Li, Y., Fu, Q., and Flytzani-Stephanopoulos, M. Low-temperature water-gas shift reaction over Cu- and Ni-loaded cerium oxide catalysts. *Appl. Catal. B Environ. 27*, 3 (aug 2000), 179–191.

[67] Lombardo, D., Kiselev, M. A., Magazù, S., and Calandra, P. Amphiphiles self-assembly: Basic concepts and future perspectives of supramolecular approaches. *Adv. Condens. Matter Phys. 2015* (2015).

[68] Longo, I., and Ricci, A. S. Chemical activation using an open-end coaxial applicator. *J. Microw. Power Electromagn. Energy 41*, 1 (2007), 4–19.

[69] López, E., Divins, N. J., Anzola, A., Schbib, S., Borio, D., and Llorca, J. Ethanol steam reforming for hydrogen generation over structured catalysts. *Int. J. Hydrogen Energy 38*, 11 (apr 2013), 4418–4428.

[70] Malik, M. A., Hashim, M. A., Nabi, F., AL-Thabaiti, S. A., and Khan, Z. Anti-corrosion ability of surfactants: A review. *Int. J. Electrochem. Sci. 6*, 6 (2011), 1927–1948.

[71] Manet, S., Schmitt, J., Imperor-Clerc, M., Zholobenko, V., Durand, D., Oliveira, C. L. P., Pedersen, J. S., Gervais, C., Baccile, N., Babonneau, F., Grillo, I., Meneau, F., and Rochas, C. Kinetics of the formation of 2D-hexagonal silica nanostructured materials by nonionic block copolymer templating in solution. *J. Phys. Chem. B 115*, 39 (2011), 11330–11344.

[72] Mao, X., Jiang, R., Xiao, W., and Yu, J. Use of surfactants for the remediation of contaminated soils: A review. *J. Hazard. Mater. 285* (2015), 419–435.

[73] Martin, T., Galarneau, A., Renzo, F. D., Brunel, D., and Fajula, F. Great Improvement of Chromatographic Performance Using MCM-41 Spheres as Stationary Phase in HPLC. *Chem. Mater. 16*, 9 (2004), 1725–1731.

[74] Nagarajan, R., and Ruckenstein, E. Theory of Surfactant Self-Assembly: A Predictive Molecular Thermodynamic Approach. *Langmuir 7*, 12 (1991), 2934–2969.

[75] Nakahara, Y., Takeuchi, T., Yokoyama, S., and Kimura, K. Quantitative 1H NMR analysis of reacted silanol groups in silica nanoparticles chemically modified with monochlorosilanes. *Surf. Interface Anal. 43*, 4 (2011), 809–815.

[76] Newalkar, B. L., Komarneni, S., and Katsuki, H. Rapid synthesis of mesoporous SBA-15 molecular sieve by a microwavehydrothermal process. *Chem. Commun. 3*, 23 (2000),

2389–2390.

[77] Ninham, B. W. On progress in forces since the DLVO theory. *Adv. Colloid Interface Sci. 83*, 1 (1999), 1–17.

[78] Nooney, R. I., Kalyanaraman, M., Kennedy, G., and Maginn, E. J. Heavy metal remediation using functionalized mesoporous silicas with controlled macrostructure. *Langmuir 17*, 2 (2001), 528–533.

[79] Ochoa-Gómez, J. R., Gómez-Jiménez-Aberasturi, O., Maestro-Madurga, B., Pesquera-Rodríguez, A., Ramírez-López, C., Lorenzo-Ibarreta, L., Torrecilla-Soria, J., and Villarán-Velasco, M. C. Synthesis of glycerol carbonate from glycerol and dimethyl carbonate by transesterification: Catalyst screening and reaction optimization. *Appl. Catal. A Gen. 366*, 2 (2009), 315–324.

[80] Olson, M. A., Thompson, J. R., Dawson, T. J., Hernandez, C. M., Messina, M. S., and O'Neal, T. Template-directed self-assembly by way of molecular recognition at the micellarsolvent interface: modulation of the critical micelle concentration. *Org. Biomol. Chem. 11*, 38 (2013), 6483.

[81] Palma, V., Castaldo, F., Ciambelli, P., and Iaquaniello, G. CeO2-supported Pt/Ni catalyst for the renewable and clean H2 production via ethanol steam reforming. *Appl. Catal. B Environ. 145* (2014), 73–84.

[82] Park, S. H., Song, B. Y., and Lee, T. G. Effects of surfactant/silica and silica/cerium ratios on the characteristics of mesoporous Ce-MCM-41. *J. Ind. Eng. Chem. 14*, 2 (mar 2008), 261–264.

[83] Peng, R., Zhao, D., Dimitrijevic, N. M., Rajh, T., and Koodali, R. T. Room Temperature Synthesis of Ti-MCM-48 and Ti-MCM-41 Mesoporous Materials and Their Performance on Photocatalytic Splitting of Water. *J. Phys. Chem. C 116*, 1 (2012), 1605–1613.

[84] Qiu, S., Zhang, X., Liu, Q., Wang, T., Zhang, Q., and Ma, L. A simple method to prepare highly active and dispersed Ni/MCM-41 catalysts by co-impregnation. *Catal. Commun. 42*, 3 (dec 2013), 73–78.

[85] Rayo, P., Rana, M., Ramirez, J., Ancheyta, J., and Aguilarelguezabal, a. Effect of the preparation method on the structural stability and hydrodesulfurization activity of NiMo/SBA-15 catalysts. *Catal. Today 130*, 2-4 (jan 2008), 283–291.

[86] Reddy, B., and Khan, A. Structural characterization of nanosized CeO2-SiO2, CeO2-TiO2, and CeO2-ZrO2 catalysts by XRD, Raman, and HREM techniques. *J. ... 109* (2005), 3355–3363.

[87] Reddy, E. P. E., Sun, B., and Smirniotis, P. P. G. Transition

Metal Modified TiO2-Loaded MCM-41 Catalysts for Visible- and UV-Light Driven Photodegradation of Aqueous Organic Pollutants. *J. Phys. Chem. B 108*, 44 (2004), 17198–17205.

[88] Salesch, T., Bachmann, S., Brugger, S., Rabelo-Schaefer, R., Albert, K., Steinbrecher, S., Plies, E., Mehdi, A., Reyé, C., Corriu, R. J., and Lindner, E. New inorganic-organic hybrid materials for HPLC separation obtained by direct synthesis in the presence of a surfactant. *Adv. Funct. Mater. 12*, 2 (2002), 134–142.

[89] Sánchez-Sánchez, M., Navarro, R., and Fierro, J. Ethanol steam reforming over Ni/MxOyAl2O3 (M= Ce, La, Zr and Mg) catalysts: influence of support on the hydrogen production. *Int. J. Hydrogen Energy 32* (2007), 1462–1471.

[90] Serrano, D. P., Coronado, J. M., de la Peña O'Shea, V. A., Pizarro, P., and Botas, J. Á. Advances in the design of ordered mesoporous materials for low-carbon catalytic hydrogen production. *J. Mater. Chem. A 1*, 39 (2013), 12016.

[91] Shiloach, A., and Blankschtein, D. Prediction of Critical Micelle Concentrations of Nonideal Binary Surfactant Mixtures. *Langmuir 13*, 15 (1997), 3968–3981.

[92] Smit, B., Esselink, K., Hilbers, P. A., van Os, N. M., Rupert, L. A., and Szleifer, I. Computer Simulations of Surfactant Self-Assembly. *Langmuir 9*, 1 (1993), 9–11.

[93] Sonnati, M. O., Amigoni, S., Taffin de Givenchy, E. P., Darmanin, T., Choulet, O., and Guittard, F. Glycerol carbonate as a versatile building block for tomorrow: synthesis, reactivity, properties and applications. *Green Chem. 15*, 2005 (2013), 283–306.

[94] Svenson, S. Controlling surfactant self-assembly. *Curr. Opin. Colloid Interface Sci. 9*, 3-4 (2004), 201–212.

[95] Taguchi, A., and Schüth, F. Ordered mesoporous materials in catalysis. *Microporous Mesoporous Mater. 77*, 1 (jan 2005), 1–45.

[96] Tanaka, M., Itadani, A., Kuroda, Y., and Iwamoto, M. Effect of Pore Size and Nickel Content of Ni-MCM-41 on Catalytic Activity for Ethene Dimerization and Local Structures of Nickel Ions. *J. Phys. Chem. C 116*, 9 (2012), 5664–5672.

[97] Thommes, M., Kaneko, K., Neimark, A. V., Olivier, J. P., Rodriguez-Reinoso, F., Rouquerol, J., and Sing, K. S. W. Physisorption of gases, with special reference to the evaluation of surface area and pore size distribution (IUPAC Technical Report). *Pure Appl. Chem. 87*, 9-10 (2015), 1051–1069.

[98] Tompsett, G. A., Conner, W. C., and Yngvesson, K. S. Microwave synthesis of nanoporous materials. *ChemPhysChem 7*, 2 (2006), 296–319.

[99] Topka, P., Karban, J., Soukup, K., Jirátová, K., and Šolcová, O. Preparation of AlSBA-15 pellets with low amount of additives: Effect of binder content on texture and mechanical properties. Application to FriedelCrafts alkylation. *Chem. Eng. J. 168*, 1 (mar 2011), 433–440.

[100] Trébosc, J., Wiench, J. W., Huh, S., Lin, V. S.-Y., and Pruski, M. Solid-state NMR study of MCM-41-type mesoporous silica nanoparticles. *J. Am. Chem. Soc. 127*, 9 (2005), 3057–3068.

[101] Triantafillidis, C. S., Vlessidis, A. G., and Evmiridis, N. P. Dealuminated HY Zeolites: Influence of the Degree and the Type of Dealumination Method on the Structural and Acidic Characteristics of HY Zeolites. *Ind. Eng. Chem. Res. 39*, 2 (2000), 307–319.

[102] van Grieken, R., Escola, J., Moreno, J., and Rodríguez, R. Direct synthesis of mesoporous M-SBA-15 (M=Al, Fe, B, Cr) and application to 1-hexene oligomerization. *Chem. Eng. J. 155*, 1-2 (dec 2009), 442–450.

[103] Vicente, J., Ereña, J., Montero, C., Azkoiti, M. J., Bilbao, J., and Gayubo, A. G. Reaction pathway for ethanol steam reforming on a Ni/SiO2 catalyst including coke formation. *Int. J. Hydrogen Energy 39*, 33 (nov 2014), 18820–18834.

[104] Vinu, A., Hossain, K. Z., and Ariga, K. Recent Advances in Functionalization of Mesoporous Silica. *J. Nanosci. Nanotechnol. 5*, 3 (2005), 347–371.

[105] Walcarius, A., and Delacôte, C. Rate of Access to the Binding Sites in Organically Modified Silicates. 3. Effect of Structure and Density of Functional Groups in Mesoporous Solids Obtained by the Co-Condensation Route. *Chem. Mater. 15*, 22 (2003), 4181–4192.

[106] Wan, Y., and Zhao, D. On the controllable soft-templating approach to mesoporous silicates. *Chem. Rev. 107*, 7 (2007), 2821–2860.

[107] Wu, C.-G., and Bein, T. Microwave synthesis of molecular sieve MCM-41. *Chem. Commun.*, 8 (1996), 925–926.

[108] Wu, N., Zhang, W., Li, B., and Han, C. Nickel nanoparticles highly dispersed with an ordered distribution in MCM-41 matrix as an efficient catalyst for hydrodechlorination of chlorobenzene. *Microporous Mesoporous Mater. 185* (feb 2014), 130–136.

[109] Wu, X., and Kawi, S. Rh/Ce-SBA-15: Active and stable catalyst for CO2 reforming of ethanol to hydrogen. *Catal. Today 148*, 3-4 (nov 2009), 251–259.

[110] Xin, C., Zhao, N., Zhan, H., Xiao, F., Wei, W., and Sun, Y. Phase transition of silica in the TMB-P123-H2O-TEOS quadru-component system: A feasible route to different mesostructured materials. *J. Colloid Interface Sci. 433* (2014),

176–182.

[111] Xu, W., Liu, Z., Johnston-peck, A. C., Senanayake, S. D., Zhou, G., Stacchiola, D. J., Stach, E. A., and Rodriguez, J. A. Steam Reforming of Ethanol on Ni/CeO2: Reaction Pathway and Interaction between Ni and the CeO2 Support. *ACS Catal. 2*, eq 6 (2013).

[112] Yang, C.-m., Zibrowius, B., and Schuth, F. A novel synthetic route for negatively charged ordered mesoporous silica SBA-15. *Chem. Commun.*, 14 (2003), 1772–1773.

[113] Yao, W., Chen, Y., Min, L., Fang, H., Yan, Z., Wang, H., and Wang, J. Liquid oxidation of cyclohexane to cyclohexanol over cerium-doped MCM-41. *J. Mol. Catal. A Chem. 246* (2006), 162–166.

[114] Ye, J., Wang, Y., and Liu, Y. NiO-Ce0.5Zr0.5O2 catalysts prepared by citric acid method for steam reforming of ethanol. *J. Rare Earths 26*, 6 (dec 2008), 831–835.

[115] YU, Y., ZHAO, J., and Bayly, A. E. Development of Surfactants and Builders in Detergent Formulations. *Chinese J. Chem. Eng. 16*, 4 (2008), 517–527.

[116] Zhan, W., Lu, G., Guo, Y., Guo, Y., Wang, Y., Wang, Y., Zhang, Z., and Liu, X. Synthesis of cerium-doped MCM-48 molecular sieves and its catalytic performance for selective oxidation of cyclohexane. *J. Rare Earths 26*, 4 (aug 2008), 515–522.

[117] Zhang, L., Zhao, Y., Dai, H., He, H., and Au, C. A comparative investigation on the properties of Cr-SBA-15 and CrOx/SBA-15. *Catal. Today 131*, 1-4 (feb 2008), 42–54.

[118] Zhang, Y., Gao, F., Wan, H., Wu, C., Kong, Y., Wu, X., Zhao, B., Dong, L., and Chen, Y. Synthesis, characterization of bimetallic CeFe-SBA-15 and its catalytic performance in the phenol hydroxylation. *Microporous Mesoporous Mater. 113*, 1-3 (aug 2008), 393–401.

[119] Zhang, Z., Santangelo, D. L., Ten Brink, G., Kooi, B. J., Moulijn, J. A., and Melián-Cabrera, I. On the drug adsorption capacity of SBA-15 obtained from various detemplation protocols. *Mater. Lett. 131* (2014), 186–189.

[120] Zhao, D., Feng, J., Huo, Q., Melosh, N., Fredrickson, G. H., Chmelka, B. F., and Stucky, G. D. Triblock Copolymer Syntheses of Mesoporous Silica with Periodic 50 to 300 Angstrom Pores. *Science (80-.). 279*, 5350 (jan 1998), 548–552.

[121] Zhao, D., Yang, P., Melosh, N., Feng, J., Chmelka, B. F., and Stucky, G. D. Continuous Mesoporous Silica Films with Highly Ordered Large Pore Structures. *Adv. Mater. 10*, 16 (nov 1998), 1380–1385.

[122] Zhao, X. S., Lu, G. Q., Whittaker, a. K., Millar, G. J., and

ZHU, H. Y. Comprehensive study of surface chemistry of MCM-41 using Si-29 CP/MAS NMR, FTIR, pyridine-TPD, and TGA. *J. Phys. Chem. B 101*, 33 (1997), 6525–6531.

[123] ZIENKIEWICZ-STRZAŁKA, M., AND PIKUS, S. The study of palladium ions incorporation into the mesoporous ordered silicates. *Appl. Surf. Sci. 261* (nov 2012), 616–622.

Appendix A

List of abbreviations

A.1 Recurrent abbreviations used in this work

BET Brunauer-Emmett-Teller method
BJH Barrett-Joyner-Halenda method
CAC Critical aggregate concentration
CMC Critical micelle concentration
CTABr Hexadecyltrimethylammonium bromide
ESR Ethanol steam reforming reaction
FTIR-ATR Attenuated total reflectance Fourier Transform Infrared Spectroscopy
MAS-NMR Magic angle spinning nuclear magnetic resonance
MCM-41 Mobil Composition of Matter, mesoporous silica MCM-41
MW Microwaves, microwave irradiation
P123 Pluronic paste-123 (triblock poloxamer)
SAXS Small Angle X-ray scattering
SBA-15 Santa Barbara Amorphous, mesoporous silica SBA-15
SEM Scanning electron microscopy
TEM Transmission electron microscopy
TMB 1,3,5-trimethylbenzene
US Ultrasounds
UV-vis DR UV-visible diffuse reflectance spectroscopy
WAXRD Wide Angle X-ray diffraction
WGS Water gas shift reaction

List of Figures

List of Tables

Part VI

List of Publications

Paper I

Ultrasound and microwave-assisted synthesis of hexagonally ordered Cerium-modified mesoporous silica as Nickel catalytic supports for Hydrogen production

Authors: J. Tovar Rodrguez, E. Fratini, P. Baglioni, C. Ferrari, J. A. de los Reyes Heredia, G. Y. Ramrez Hernndez and I. R. Galindo Esquivel

Submitted to the RSC Journal of Materials Chemistry A

Journal Name

ARTICLE

Received 00th January 20xx,
Accepted 00th January 20xx

DOI: 10.1039/x0xx00000x

www.rsc.org/

Ultrasound and microwave-assisted synthesis of hexagonally ordered Cerium-modified mesoporous silica as Nickel catalytic supports for Hydrogen production

J. Tovar Rodríguez[a], E. Fratini[a], P. Baglioni[a], C. Ferrari[b], J. A. de los Reyes Heredia[c], G. Y. Ramírez Hernández[d], I. R. Galindo Esquivel[d*]

Cerium-modified hexagonally ordered silica sieves were prepared by ultrasound-assisted solvothermal synthesis to obtain highly dispersed Ce into the silica framework. The explored Ce/Si molar ratios for the synthesis of the mesoporous materials ranged from 0.02 to 0.08. Microwave irradiation applied by a coaxial antenna was used for thermal activation to reduce the overall hydrothermal synthesis time. The hexagonal ordering of the materials decreased as a consequence of Ce direct incorporation in the structure. As the amount of Ce/Si increased a second mechanism of Ce incorporation resulted in ceria particles condensation outside the silica framework. Nevertheless, the sonochemical approach hindered structure collapse since all materials preserved the hexagonal ordering, exhibited uniform pore size distribution and high surface areas (over 546m^2/g). These materials were analysed by means of SAXS, WAXRD, FT-IR ATR, UV-vis DRS, ^{29}Si HPDEC MAS-NMR, N_2 Physisorption, HR-TEM and SEM. The mesoporous sieves were used as catalytic supports for a Ni active phase (10 wt.% of metal loading). Their catalytic activity was evaluated in the ethanol steam reforming reaction to produce hydrogen. The new catalysts featured complete ethanol conversion, and higher H_2 selectivity (compared to the same Ni catalyst over bare silica) ranging from 60 to 65%. The main product distribution depended to a small degree on Ce content, these materials did not exhibit catalyst deactivation after 6h on stream and were selective towards H_2, CO_2, CO and CH_4 as sole reaction products.

1. Introduction

Ordered mesoporous molecular sieves are a versatile class of template-based materials that can find multiple applications in catalysis[1], fuel cell applications[2], gas[3,4] or heavy metals adsorption[5] and as matrixes for drug delivery[6]. In particular, the pure siliceous MCM-41 exhibits a hexagonal ordering, high surface area and a narrow pore size distribution[7], but it is seldom used as such since it lacks any catalytic activity. Several examples can be found in the literature concerning the structural modification of mesoporous silica, either by direct or post-synthesis functionalization, in order to provide catalytic activity[8]. MCM-41 has been modified with transition metals and has been used for oxidative catalysis, acid-base catalysis, photocatalysis or as catalytic support for a metal active site[9–11]. Therefore, it is important to develop synthesis routes that make possible structure modification and tailoring its characteristics in a minimum number of steps while preserving the high surface area, hexagonal ordering and other features of the parent MCM-41 material.

In this regard, the acoustic cavitation produced by ultrasound (US) has demonstrated to improve the nucleation and crystallization steps during the solvothermal synthesis of template-based micro and mesoporous materials such as zeolites or zeotypes[12]. Still, the sonochemical synthesis of metal-modified mesoporous silica is scarcely reported. On the other hand, microwave assisted chemistry (MW) is a useful tool for thermal activation to reduce the long synthesis time typically required to produce ordered nanoporous materials[13]. Depending on the dielectric properties of the reaction medium and solvents, it is possible to achieve shorter synthesis times by a more effective heating and temperature profile produced by MW irradiation. Nonetheless, most of the commercially available reactors for MW-synthesis have a traditional closed-box configuration, which makes them particularly unsuitable for scaling-up and may limit their operative conditions or coupling with other techniques[14].

Given its oxygen vacancies and oxygen storage capacity[15], cerium oxide and cerium-based composite materials are a well known and preferred catalyst for oxidation of reagents. For instance, cerium modified mesoporous silicas have been

---

[a] Dipartimento di Chimica "Ugo Schiff", Consorzio per lo Sviluppo dei Sistemi a Grande Interfase CSGI. Università degli Studi di Firenze. Via della Lastruccia 3, 50019, Sesto Fiorentino, Firenze. Italia.

[b] Consiglio Nazionale delle Ricerche, Istituto Nazionale di Ottica UOS – Pisa. Via Giuseppe Moruzzi 1, 56124. Pisa, Italia.

[c] Universidad Autónoma Metropolitana. División de Ciencias Básicas e Ingeniería. Av. San Rafael Atlixco No. 186, Col. Vicentina 09340, Distrito Federal, México.

[d] Universidad de Guanajuato. División de Ciencias Naturales y Exactas. Noria alta S/N, Col. Noria Alta 36050. Guanajuato, Guanjuato. México.

†Electronic Supplementary Information (ESI) available: See DOI: 10.1039/x0xx00000x

successfully employed for the selective oxidation of organic compounds[16], exhibiting negligible pore diffusion resistance, higher selectivity, improved catalytic activity[17] and good catalyst reusability[18], compared to Ce over amorphous SiO_2, CeO_2 or other cerium-based supports. Furthermore, Ce-promoted hexagonally ordered materials have also been used as catalytic supports for metallic active phases in the reforming reactions of hydrocarbons to produce hydrogen, since their oxidation capacity makes them less prone to carbon deposition, carbon poisoning and consequent catalyst deactivation[19–21].

The growing interest in hydrogen as an alternative energy carrier is based on its non-polluting nature and several noble metals such as Ru, Pd, Ag[22], Pt[23] and Rh[24] have demonstrated to be adequate catalysts for the ethanol steam reforming reaction. However, their widespread use still faces the high costs and limited availability associated to the materials based on noble metals. In order to address this issue, transition metal catalysts like Ni and Co represent a cheap and effective alternative. Nonetheless, Ni catalysts tend to deactivate swiftly, as they seem to promote ethylene, acetaldehyde and acetone formation, all of which have been identified as coke precursors[25]. For this reason, it is necessary to design catalytic supports that enhance the synergy between the active phase and the support to improve hydrogen yields and inhibit carbon deposition.

In this work, isomorphic incorporation of cerium in the MCM-41 hexagonal structure was achieved by applying ultrasounds during the direct synthesis of Ce modified MCM-41. Once optimal conditions were found for improved hexagonal ordering, microwave irradiation was applied for thermal activation by means of an innovative coaxial antenna. To the best of our understanding, no other reports can be found regarding the US-MW Ce-modification of mesoporous silica. Cerium distribution and location in the hexagonal structure was assessed by several characterization techniques. The effect of structural and chemical change on their catalytic performance was evaluated by using them as supports for a nickel active phase in the hydrogen production through ethanol steam reforming reaction (ESR).

2. Experimental

2.1 Ultrasound and microwave assisted synthesis of cerium-modified mesoporous silica.

Cerium isomorphic substitution in mesoporous silica was achieved in a direct synthesis approach. The structure-directing agent was the cationic amphiphilic molecule hexadecyltrimethylammonium bromide (CTABr, $CH_3(CH_2)_{15}N(Br)(CH_3)_3$ Sigma-Aldrich). Ammonium hydroxide was used as mineralizing agent (30% NH_3 wt/v Sigma); cerium nitrate was used as Ce precursor ($Ce(NO_3)_3•6(H_2O)$, Sigma-Aldrich) and tetraethyl orthosilicate was used as silicon source (TEOS, $CH_3CH_2O)_4Si$ Sigma-Aldrich). All reagents were used without further purification. A series of materials with the following molar composition of the synthesis colloid were prepared: 1.0 $(CH_3CH_2O)_4Si$: $xCe(NO_3)_3*6H_2O$: 0.3CTABr : $20NH_3$: $180H_2O$; x = 0.02, 0.04, 0.06 and 0.08. The materials were named xCeMCM-41, where x indicates the Ce/Si nominal molar ratio. The MCM-41 hydrothermal synthesis reported by Kresge et al.[26], was modified by adding a Ce precursor and using ultrasounds during the nucleation step to increase Ce dispersion in the mesoporous structure. Hydrothermal synthesis using microwave irradiation was carried out in a stainless steel high-pressure reactor using a coaxial antenna for in-situ MW application. Details concerning the design, construction of the reactor[27] and the technical specifications for the MW antenna can be found elsewhere[14]. Conventional hydrothermal synthesis was performed in a Teflon-lined stainless steel reactor using a heating mantle.

In a typical batch, 2.85g of CTABr were dissolved in 50ml of deionized water and 33.5ml of NH_4OH. The temperature of the solution was kept at 45°C and under vigorous stirring (500rpm) for 0.5h. A second solution containing the required amount of cerium nitrate dissolved in 12.5ml of deionized water was mixed with the surfactant solution. Then, 5.7ml of TEOS were added dropwise to the mixture. The colloidal solution was treated with ultrasounds for another 2.5h (frequency 40kHz), before being aged for an additional 4h. The samples were treated hydrothermally at 100°C and autogenous pressure for 24h (conventional synthesis) and 1h (for MW-assisted synthesis). A precipitated product was separated by centrifugation, washed with deionized water and dried at 80°C overnight. The obtained powder was annealed at 550°C and atmospheric pressure under static air for 4h to remove the surfactant and to yield a porous material.

2.2 Synthesis of Ni catalyst over Ce-MCM-41.

Ni catalysts were prepared by wet impregnation method to achieve a total loading of 10wt % of Ni over the catalyst, using a solution of $Ni(NO_3)_2•6H_2O$ (Aldrich). The resulting solids were dried at room temperature for 24h and then calcined at 550°C for 2h. Hereafter, the catalysts containing 10wt % of Ni are referred to as Ni/xCeMCM-41, using the aforementioned values for x depending on the nominal amount of Ce molar load in the support.

2.3 Characterization.

SAXS measurements were carried out with a HECUS S3-MICRO camera (Kratky-type) equipped with a position-sensitive detector (OED 50M) containing 1024 channels of width 54 μm. Cu Kα radiation of wavelength $\lambda = 1.542Å$ was provided by an ultra-brilliant point micro-focus X-ray source (GENIX-Fox 3D, Xenocs, Grenoble), operating at a maximum power of 50 W (50kV and 1mA). The sample-to-detector distance was 281 mm. The volume between the sample and the detector was kept under vacuum during the measurements to minimize scattering from the air. The Kratky camera was calibrated in the small angle region using silver behenate (d = 58.34Å)[28]. Scattering curves were obtained in the Q-range between 0.05 and $0.5Å^{-1}$, assuming that Q is the scattering vector Q =

$4\pi/\lambda*\sin\theta$, and 2θ is the scattering angle. Powder samples were placed into a 1 mm demountable cell having Kapton foils as windows. Liquid samples were mounted in a capillary tube (80mm length, 1.0mm diameter, wall thickness = 0.1mm). The temperature was set at 25°C and was controlled by a Peltier element, with an accuracy of 0.1°C. All scattering curves were corrected for the empty cell or capillary contribution considering the relative transmission factor.

Wide Angle X-Ray Diffraction measurements were performed in a Bruker-D8 Advance X-ray powder Diffractometer in the Bragg-Brentano θ-2θ geometry. The X-ray source was Cu Kα radiation, operating at 40kV and 30mA with a wavelength of λ = 1.54Å. The detection was carried out using a Lynx-eye linear-type detector, in the 2θ interval from 1 to 70 degrees.

Attenuated Total Reflectance Fourier Transform infrared spectra were obtained for samples before and after being calcined, in the wavenumber interval from 600 to 4000cm^{-1} with an FT Infrared Spectrometer Thermo Nicolet Nexus 4700 FT-IR ATR.

Diffuse reflectance UV-vis spectra of the Ce modified samples were acquired by using a UV-Vis Spectrometer (Perkin Elmer USA Lambda 3S) in the wavelength interval of 200 to 600nm, using MgO as reference.

The ^{29}Si Solid-state Nuclear Magnetic Resonance spectra (MAS-NMR) of the powder samples were recorded using a Bruker AVANCE II NMR Spectrometer with a CPMAS H-X BB detector of 4mm, operating at a resonance frequency of 59MHz. The spin velocity of the sample was set at 5kHz and the recycling time between experiments was 10s using the High Power Decoupling, Cross-Polarization technique (HPDEC).

High resolution Transmission Electron Microscopy (HR-TEM) was performed with a JEOL 2100F equipment, using a lighting source of 200kV of acceleration and a high vacuum system, to obtain both TEM and High Angle Annular Dark Field (HAADF) micrographs.

Nitrogen adsorption and desorption isotherms were acquired using a Beckman Coulter SA-3100 Surface area analyser. Calcined samples were outgassed prior to analysis in vacuum conditions at a temperature of 200°C until a pressure of 0.01mmHg was reached.

Morphology and particle size of the catalysts were analysed using a SIGMA Field Emission Scanning Electron Microscope (Carl Zeiss Microscopy GmbH, Germany). The micrographs were acquired from uncoated samples, using the In-Lens Secondary Electron detector and the Backscattered Electron Diffraction (EBDS) simultaneously to yield Z-contrast micrographs of the catalysts.

2.4 Catalytic Evaluation of the Ni/Ce-MCM-41.

The ethanol steam reforming reaction was performed in a reactor with 10mm of internal diameter and a length of 50cm. A catalyst sample of 50mg was placed in the reactor in a powder quartz bed. A thermocouple K-type was placed near the catalytic bed to control the reaction temperature. The catalysts were reduced in-situ at 550°C for 2 hours with a hydrogen flow of 50cm^3/min and a heating rate of 10°C/min. After reduction, the system was flushed with 50cm^3/min of argon for 15 min. The reforming reactions were performed at 450 and 500°C under atmospheric pressure. A liquid flow containing water and ethanol in a molar ratio of 3:1 was evaporated in argon and was fed at a rate of 0.01cm^3/min. The ethanol and water streams were mixed and adjusted with pure argon until a total flow of 100cm^3/min was measured. The composition of the reactor effluent was analysed by two gas chromatographs Clarus 580 (Perkin Elmer): one equipped with a Q-plot capillary column and an FID detector, was used for the separation of CH_4, C_2H_5OH, CH_3CHO, C_2H_4, CH_3COOH, and CH_3COCH_3. The other gas chromatograph was equipped with a Molsieve capillary column and a TCD detector for the analysis of H_2, CO, CH_4, CO_2 and C_2H_4.

3. Results

3.1 Effect of ultrasound and microwave irradiation on the characteristics of Ce-promoted hexagonally ordered mesoporous silica.

To characterise the structure and hexagonal ordering of the cerium modified silicas, SAXS curves were recorded in the low Q interval from 0.05 to 0.5Å^{-1}. Figures 1a-b show the SAXS patterns for all the xCe-MCM-41 powder samples after calcination. Silicon-based mesoporous MCM-41 exhibits four well-defined diffraction peaks, centred at Q vector values of 0.165, 0.285, 0.329 and 0.435Å^{-1} that can be associated to the scattering of the first (*hlk*) planes, where *hlk* is equal to (100), (110), (200) and (210), indexed to the hexagonal system, space group *p6mm*[26]. Table 1 summarizes the interplanar distance d_{100}, calculated using the corresponding Q vector value and Bragg's law, $\lambda = 2d_{hlk}*\sin\theta$. Once cerium is loaded into the hexagonal lattice, a shift towards lower reciprocal Q values is observed for all samples, which is indicative of larger d_{100} spacing values, as consequence of Ce direct incorporation (Table 1, d_{100} entry). In a previous publication, we demonstrated that the broadening of the d_{100} interplanar distance depends on the type of substituted heteroatom and the amount effectively incorporated in the silica framework[29]. A sample with a Ce/Si molar ratio equal to 0.02 features three well-resolved Bragg diffraction peaks (Figure 1-b 0.02CeMCM-41_US). Materials with higher cerium content exhibit less resolved scattering patterns. The interplanar spacing enlarges from 4.42nm to a maximum value of 5.04nm. This evolution towards less ordered sieves could be caused by the disparity of the covalent radii existing between Si (1.11Å) and Ce (2.04Å)[30]. Assuming that the nature of Ce incorporation into the silicon structure occurs in isomorphic manner, as the Ce/Si molar ratio increases the substitution of Si-O-Si bonding for its larger Si-O-Ce counterpart results in materials with less resolved diffraction curves. This covalent radius disproportion also accounts for larger lattice cell a_0 values (Table 1, a_0 entry)

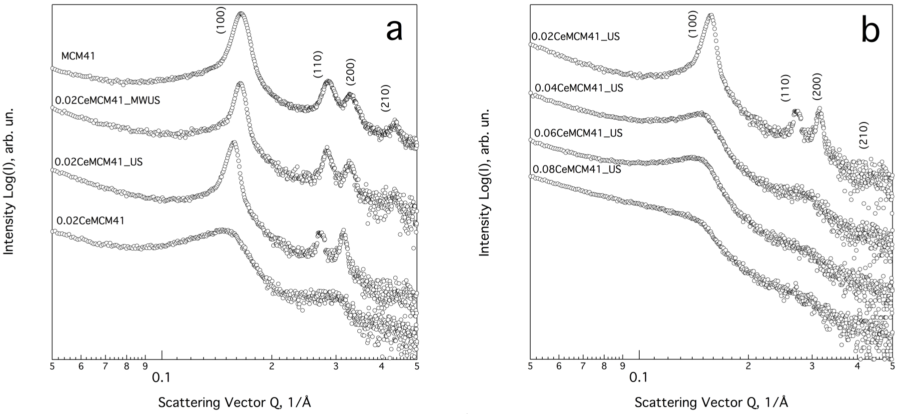

Figure 1. Small Angle X-ray Scattering curves for a) MCM-41 and Ce-modified MCM-41 (Ce/Si = 0.02) prepared using ultrasound (US), microwaves irradiation (MW) and magnetic stirring (0.02CeMCM-41); b) SAXS curves for Ce-modified silica at different Ce/Si molar ratios

For the hexagonal structure, the cell constant can be estimated as $a_0 = 2d_{100}/\sqrt{3}$ and its value ranges from 5.10 to 5.82nm (for 0.08CeMCM-41_US). To better understand the formation mechanism of the hexagonal silica framework, SAXS curves for the synthesis colloid in a liquid capillary were measured in the same Q interval (ESI Fig. S1†). Under the acquisition parameters (50W, t_{acq} = 1800s), the amphiphilic cationic surfactant solution in NH_4OH does not produce any scattering pattern typical of an ordered structure. Upon alkoxide addition, given the strong alkaline conditions (pH = 12.7), the tetraethyl orthosilicate molecules are rapidly hydrolysed and interact with the positively charged cationic micelles. For the CTAB/TEOS/NH_4OH system, a main Bragg peak can be observed with secondary less-defined peaks, suggesting that the hexagonal arrangement of the micelles occurs immediately after TEOS hydrolysis and silica oligomer formation (TEOS/CTAB molar ratio 1:0.30). Therefore, it is important to enhance dispersion of Ce species during TEOS addition and silica polymerization. A comparative study was performed to assess the hexagonal framework regularity of samples with a Ce/Si ratio of 0.02. It is noteworthy that a material prepared without ultrasounds featured a broad d_{100} peak centred on Q = 0.152Å^{-1}; a second less resolved peak, which could be interpreted as the convolution of the d_{110} and d_{200} planes, is centred at Q = 0.297Å^{-1}. On the contrary, a sample prepared using ultrasounds (0.02CeMCM_US) featured three Bragg peaks in the explored low Q interval (d_{100} = 4.63nm). This suggests that the stirring produced by acoustic cavitation effectively promoted better Ce dispersion and incorporation in the silica network during nucleation and micellar organization, compared to magnetic stirring. Considering that template-based mesoporous silica sieves with hexagonal ordering and high surface can be obtained within an hour using microwave ovens[31] or microwave digestion systems[32] (closed-box approach), the hydrothermal synthesis was enhanced by MW irradiation using a coaxial antenna for in-situ application in a high pressure reactor[27].

Table 1. Lattice cell parameters and textural properties for cerium modified mesoporous silica (d_{100}, interplanar spacing; a_0, lattice cell constant $a_0=2d_{100}/\sqrt{3}$; S_{BET}, Surface area calculated with the Brunauer Emmett Teller model; V_{pore}, Total pore volume; D_{pore}, pore diameter calculated as $D = 4*V_{pore}/S_{BET}$).

Sample name	Ce/Si ratio	d_{100}	a_0	S_{BET}, m^2/g	V_{pore}, cm^3/g	$V_{monolayer}$, cm^3/g	D_{pore}, nm
MCM41	0	4.42	5.10	980	0.86	225	3.49
0.02CeMCM41§	0.02	4.46	5.15	967	0.94	222	3.88
0.02CeMCM41*	0.02	4.78	5.52	865	0.96	199	4.45
0.02CeMCM41$^\&$	0.02	4.63	5.35	806	0.77	185	3.84
0.04CeMCM41$^\&$	0.04	4.88	5.63	711	0.68	163	3.84
0.06CeMCM41$^\&$	0.06	4.98	5.75	629	0.65	145	4.14
0.08CeMCM41$^\&$	0.08	5.04	5.82	546	0.60	125	4.39

[§] Synthesized using ultrasounds for cerium dispersion and microwaves for hydrothermal synthesis. *Conventional hydrothermal synthesis without US ageing. [&] Synthesized using ultrasounds for cerium dispersion

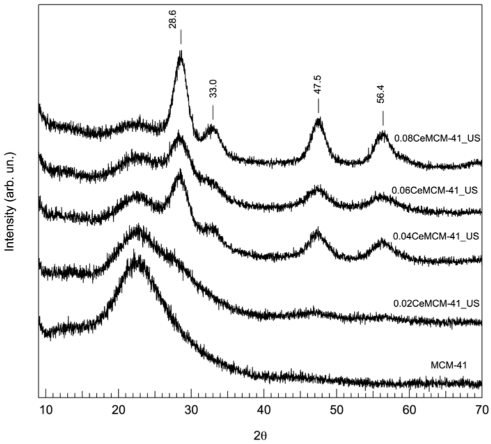

Figure 2. Wide angle X-ray diffraction curves for xCe-MCM-41_US materials.

A 0.02Ce/Si molar ratio mesoporous material was prepared using US during the nucleation step and MW for thermal activation during hydrothermal particle growth. Figure S2† shows the temperature profile for 0.02CeMCM-41_MWUS. Under this innovative synthesis approach, 100°C can be achieved within two minutes of applied power (operating at a maximum power of 240W); then, a PID controller keeps a variable supply of around 60W to maintain the desired operating temperature. Similarly, a well-defined SAXS diffraction pattern was recorded for the material prepared using MW irradiation. The interplanar distance calculated for this sample was the closest to the MCM-41 parent material (4.46nm).

Although US was helpful in achieving Ce distribution and substitution during silica self-assembly, at higher Ce/Si ratios the amount of cerium load and a larger concentration of counter ions (NO_3^-) could be responsible for hindering the hexagonal ordering by modifying micelle aggregation and density numbers[33]. On a previous report[34], optimal values for surfactant/Si and Ce/Si molar ratios were found for Ce substituted MCM-41 (0.2 and 0.025 respectively) by analysing the X-ray scattering and intensity of the d_{100} plane. A Ce-MCM41 sample prepared under magnetic stirring with a Ce/Si molar ratio of 0.025, exhibited only the scattering of the first two *hlk* planes. Taking into account the SAXS scattering curves (Bragg peaks for the [100], [110] and [200] planes for 0.02CeMCM-41_US), the ultrasound and microwave-assisted methodology here reported resulted in a material with better cerium dispersion along the hexagonal framework and a higher degree of hexagonal ordering.

To further characterise the Ce content in all samples, wide angle XRD patterns for the xCe-MCM-41_US materials were recorded in the 2θ interval from 10 to 70°. Unmodified mesoporous silica and the samples with lowest Ce/Si molar ratio exhibit a single broad peak, encompassing 2θ values from 18 to 26°. For Ce/Si values of 0.04 and higher, four diffraction peaks are observed at around 2θ values of 28.6, 33, 47.5 and 56.4°, indexed to the Bragg scattering of the (111), (200), (220) and (311) planes for the cubic phase in CeO_2. Sharper and more intense diffraction peaks were observed for the sample with the highest Ce content (0.08CeMCM-41_US). In conjunction with the SAXS analysis these findings lead to some conclusions concerning the possible mechanism of Ce incorporation into the hexagonally ordered mesoporous silica. For low metal loadings, the well preserved hexagonal structure is indicative of a successful Ce dispersion and isomorphic incorporation in the SiO_2 structure, promoted by the use of ultrasounds acoustic cavitation. Higher Ce/Si molar ratios could favour the formation of cubic CeO_2 particles outside the silica framework.

The FT-IR ATR spectra for all xCe-MCM-41_US materials are shown in Figure 3. Silica MCM-41 features three main bands can be assigned to the asymmetrical stretching vibration (ν_{as}) of the Si-O-Si bond located at wavenumber values of 1235, 1056 and 970cm^{-1}. For all cerium modified materials the main band located at 1056 shifts to 1070cm^{-1} while the intensity of the band located at 1230cm^{-1} is reduced as the molar ratio Ce/Si increases, suggesting a lower recurrence of Si-O-Si that could be replaced by Si-O-Ce bonds. The signals at about 1465 and 1480cm^{-1} can be assigned to the $\delta(CH_2)$ and $\delta_{as}(N\text{-}CH_3)$ bending modes of the surfactant molecule within the pores (scissoring region), whereas the bands at 2852 and 2923cm^{-1} belong to the symmetric and asymmetric ($\nu_{sym}(CH_2)$ and $\nu_{as}(CH_2)$) stretching modes of the surfactant chains[35] (inset figure 4). After calcination these bands are no longer present in the spectrum. The location and intensity of the band centred at 800cm^{-1}, attributed to the vibrations of the ν_s(Si-O-Si) does not change as a consequence of cerium incorporation.

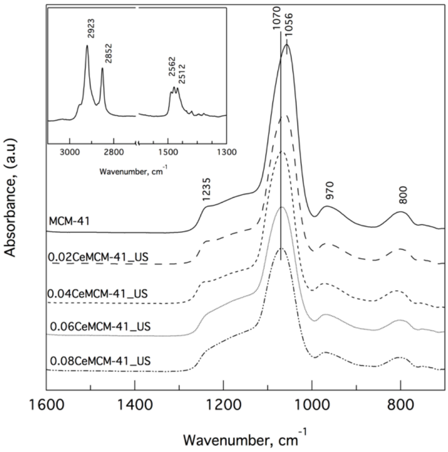

Figure 3. FT-IR ATR spectra for cerium-modified mesoporous silica (inset figure: as-synthesized MCM-41)

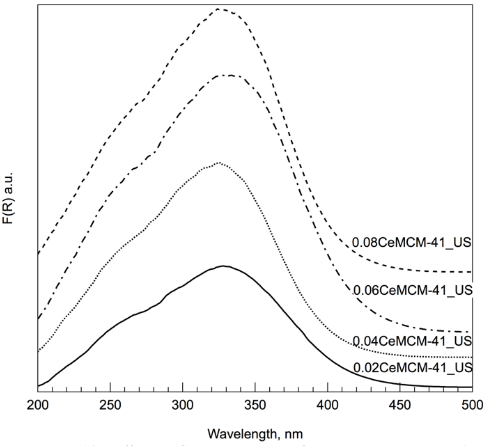

Figure 4. UV-visible Diffuse Reflectance spectra for x-Ce-MCM-41_US calcined materials

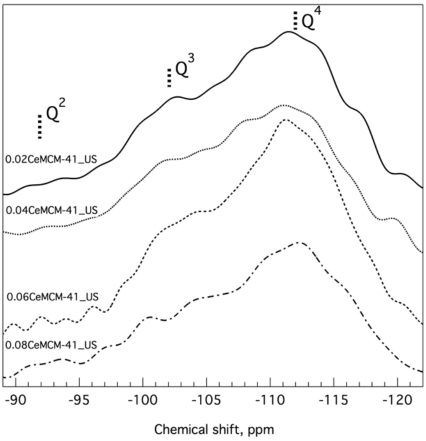

Figure 5. ^{29}Si solid-state HPDEC MAS-NMR spectra cerium modified mesoporous silica xCe-MCM-41

In order to determine the coordination of the Ce species in the hexagonal silica framework, the UV-visible Diffuse Reflectance Spectra for all calcined samples was recorded. Figure 3 shows a single broad band in the wavelength interval from 200 to 400nm for all samples with a maximum value at around 330nm. The intensity of this band increases with the amount of Ce introduced in the sample. For crystalline cerium oxide (CeO_2), there is a band gap of 3.1eV (3.7eV calculated at 330nm for these materials). Since the electronic transitions in the hexa-coordinated atom (Ce^{3+}) require more energy than the transitions for the tetra-coordinated atom (Ce^{4+}), it is possible to assign this band to the transitions Ce-O for Ce^{4+} [36]. Regardless of the position and distribution of Ce in the hexagonal silicon structure, the nature of the cerium species is tetra-coordinated for all cases.

The ^{29}Si NMR spectra for the calcined xCe-MCM-41_US materials are shown in figure 5. All samples present a broad signal ranging from -90 to -120ppm chemical shift values. In order to obtain individual information concerning the environment of the silicon nuclei in the structure, deconvolution of these signals was performed around the chemical shift values of -112, -101 and -92ppm, for Q^4, Q^3 and Q^2 species. A Gaussian/Lorentzian distribution ratio of 0.7 was chosen, to better fit the typical nuclear magnetic resonance spectra of solid samples. Table S1† summarizes the Q^n value distribution for all samples. To compare the Q^n values among samples, the total-silanol/siloxane ($(Si(OSi)_3OH)+Si(OSi)_2(OH)_2)/(Si(OSi)_4)$ and isolated silanol/siloxane $(Si(OSi)_3OH)/(Si(OSi)_4)$ ratios were calculated. Bare silica MCM-41 shows the highest amount of both geminal and isolated silanol groups, and their amount decreases when Ce is incorporated into the silica network.

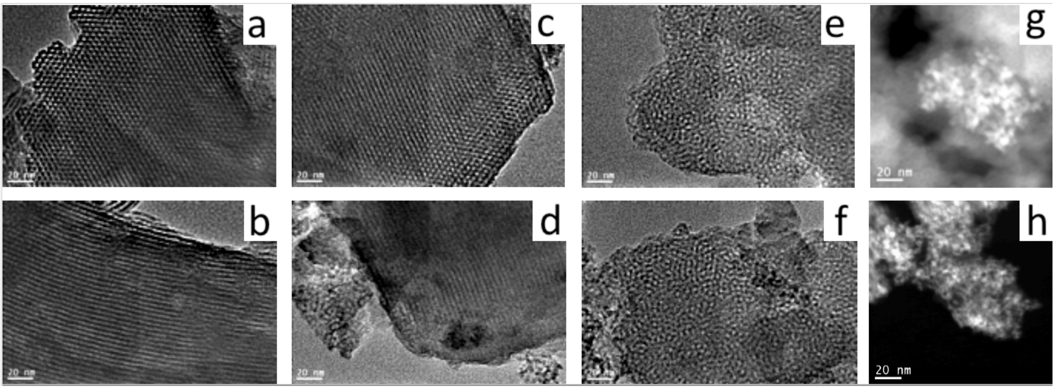

Figure 6. HR-TEM: a) Cross sectional area of the hexagonal structure and b) view along the channels for MCM-41; c) Hexagonal structure and d) interplanar distance for 0.02CeMCM-41_US; e) 0.04CeMCM-41_US and f) 0.06CeMCM-41_US; g) High-Angle Annular Dark-Field Imaging for CeO_2 particles in 0.08CeMCM-41_US and h) 0.06CeMCM-41_US. (Bar length = 20nm for all micrographs)

The isolated silanol/siloxane ratio is 0.76 for the unmodified mesoporous material and Ce incorporation results in a variable reduction ranging from 0.36 to 0.45. Although to a lesser extent, the amount of geminal silanols ($Si(OSi)_2(OH)_2$) also accounts for the total silanolic sites in the material. For unmodified silica, the recurrence of total silanol (Q^3+Q^2) is comparable to that of siloxane groups (Q^4). The reduction of both ratios could be indicative of a successful isomorphic substitution even if a correlation between the amount of Ce in the sample and the resonance of the silicon nuclei is unclear, since cerium substitution modified indeed the environment of the silicon in the hexagonal network by promoting the formation of Si-O-Ce and Ce-OH in the structure. These results agree with the spectroscopic and X-ray characterization already shown.

High Resolution Transmission Electron micrographs shown in Figure 6 provide supplementary evidence of the hexagonal arrangement characterizing the Ce modified mesoporous silica. For unmodified MCM-41, two different observation angles are featured: the cross sectional area offers a view of the hexagonal structure (Fig. 6-a). A second view along the channels of the mesoporous material (Fig. 6-b) confirms the interplanar d_{100} distance calculated by SAXS. As the material losses the degree of ordering, the interplanar distance and the pore size enlarges as a consequence of the amount of incorporated cerium in the sample. For all mesoporous solids, a honey comb-like structure is observed. High-Angle Annular Dark-Field Imaging of the sample with the highest Cerium contents (Fig. 6-g and 6-h) feature medium size CeO_2 domains condensed outside the silicon framework, which are not found in samples with lower Ce/Si ratios.

3.2 Ce-modified silicas as catalytic supports for Nickel

The Ce-promoted silicas were used as catalytic support for a Ni active phase (10% metal content). Nitrogen adsorption-desorption isotherms were recorded for calcined powders before and after Ni loading. Figure 7 shows the N_2 isotherms and pore size distribution for selected samples.

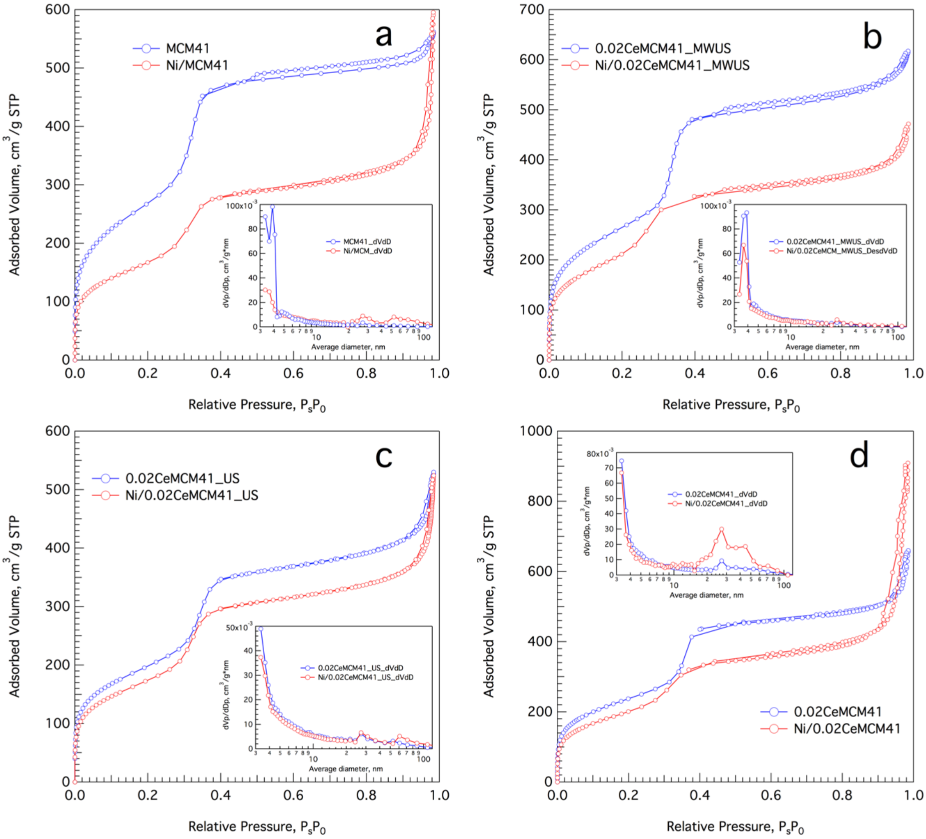

Figure 7. N_2 adsorption and desorption isotherms for a) MCM-41 and Ni/MCM-41; b) 0.02CeMCM-41_MWUS and Ni/0.02CeMCM-41_MWUS; c) 0.02CeMCM-41_US and Ni/0.02CeMCM-41_US; d) 0.02CeMCM-41 and Ni/0.02CeMCM-41

According to the classification made by IUPAC[37], all prepared materials exhibit a type IV isotherm, characteristic of mesoporous materials ranging from 2 to 50nm in pore size. For all catalytic supports, four well-defined regions in the isotherm can be identified: a) A large nitrogen uptake at very low relative pressure values (P/P_0 up to 0.02), that can be associated to micropore filling and monolayer formation; b) An inflexion point and slope change followed by a more linear region in the isotherm curve is indicative of unrestricted multilayer adsorption; c) A second inflexion point at relative pressure values close to 0.30 with a significant amount of adsorbed nitrogen is due to the mesopore capillary condensation. This relative pressure value is closely related to the pore diameter and d) a final saturation plateau once the mesopores are filled is associated to adsorbed nitrogen on the outer surface of the material and in between particles. After Ni loading, the isotherm form is kept and no significant area reductions occur, suggesting that Nickel is well distributed and does not produce pore blocking. For Ni/MCM-41 and Ni/0.02CeMCM-41 a final N_2 uptake at relative pressure values close to 1.0 could be indicative of inter-particle sintering and adsorption that does not contribute to the surface area calculations. Figure S3a-d† show the isotherm and pore size distribution for cerium-modified mesoporous silicas prepared at higher Ce/Si molar ratios. The Barrett-Joyner-Halenda pore size distribution graphs (inset figures 7a-d and S3a-d†), show a monomodal size for mesoporous solids prepared at low Ce/Si molar ratios while a second pore size (close to 40nm) can be observed for the samples with highest cerium content (0.06 and 0.08), suggesting a second type of assembly and silica polymerization. A summary of the textural properties for all materials is reported in Table 1. The calculations for the surface area were performed with the Brunauer-Emmet-Teller method. Unmodified mesoporous MCM-41 features the highest surface area (980m^2/g), the narrowest pore size estimated as 3.49nm (assuming a cylindrical pore with open endings), the highest monolayer capacity (225m^2/g) and pore volume (0.86cm^3/g) For the Cerium-promoted mesoporous silicas, the highest surface area was obtained when microwave irradiation was used for thermal activation during the hydrothermal synthesis, which suggests that the more uniform temperature profile obtained with MW enabled a more uniform particle growth during the solvothermal treatment. The sample with the highest Ce/Si molar ratio has a surface area of 546m^2/g. The pore size broadens from 3.49nm for unmodified mesoporous silica, to the largest value of 4.39nm for 0.08CeMCM-41_US and the monolayer adsorptive capacity is reduced to 125m^2/g. Nonetheless, all synthesized materials exhibit areas well above the values reported elsewhere for ceria and ceria/silica as catalytic supports[38,39], or those obtained with sol-gel methodologies. Since the pore size tends to enlarge as a consequence of the increment in the amount of Ce in the sample, a reduction in the capillary forces in the material could occur, and the total pore volume decreases to 0.60cm^3/g, without implying a morphology change. This effect can also be observed in a reduced nitrogen uptake at the capillary condensation region for samples with higher Ce/Si molar ratios (figures S3a-d†).

To characterise the Ni deposition and particle size on the mesoporous MCM-41 material, Scanning Electron micrographs were acquired using dual detection for secondary and backscattered electrons to yield Z-contrast images of the Ni active phase on the catalyst surface (Fig. 8-a and 8-b). The wet impregnation method enabled the formation of highly dispersed Ni clusters using cerium modified MCM-41 as catalytic support. Although the dispersion of Ni catalyst on pure siliceous MCM-41 was recently reported by co-condensation[40] and co-impregnation[41], the effect of cerium isomorphic incorporation on the particle size of the Ni clusters is still poorly understood. Nonetheless, the methodology here reported, resulted in catalyst with a very well distributed Nickel active phase. For MCM-41, elongated club-like particles can be observed.

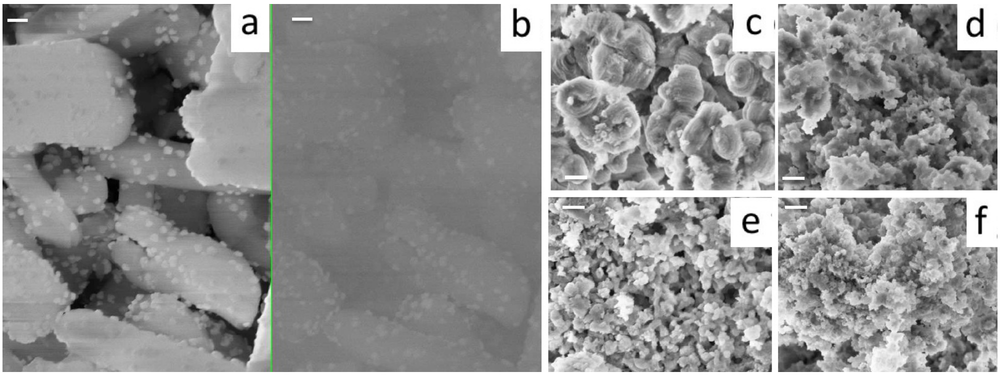

Figure 8. SEM Micrographs for 10%Ni/MCM-41: (a) Obtained using the In-lens detector; (b) Z-contrast image acquired using Backscattered Electron Diffraction. Particle morphology for: (c) Ni/0.02CeMCM-41_US, (d) Ni/0.04CeMCM-41_US, (e) Ni/0.06CeMCM-41_US and (f) Ni/0.08CeMCM-41_US catalysts. (Bar length = 200nm, magnification 100kX for all micrographs).

As the amount of cerium increases in the sample, the disruptive effect of Ce incorporation on the self-assembly of the micellar aggregates and particle growth produced a different morphology in MCM-41 resulting in shorter round-like particles (for intermediate Ce content) and flake-like morphologies (at higher Ce/Si ratios). Large Ni particles are easily observed in pure Si MCM-41 (Fig 8a and 8b) that were not distinguished in other materials.

3.3 Catalytic evaluation of Ni over Ce-promoted silica in the ethanol steam reforming reaction

The catalytic performance of Ni supported on xCe-MCM-41 was evaluated in the ethanol steam reforming reaction (ESR). The overall reaction is:

$C_2H_5OH + 3H_2O \rightarrow 6H_2 + 2CO_2$ (1)

For the Ni/xCeMCM-41 catalyst series, figure 9 reports ethanol conversion and product distribution vs. reaction time. The molar composition for the individual species (y_i) was calculated in terms of all the formed products ($\Sigma_j F_j$), as $y_i = F_i/\Sigma_j F_j$. The conversion of ethanol was obtained using the value of the fluxes at the entrance and exit of the reactor: X_{EtOH} (%) = $[(F_{EthOH,\,in} - F_{EthOH,\,out})/F_{EtOH,\,in}]*100$.

According to a proposed reaction mechanism[42], some of the side reactions that can occur during the ESR are ethanol cracking to C1 products (eq. 2), followed by steam reforming of CH_4 (eq. 3)

$C_2H_5OH + H_2O \rightarrow CH_4 + CO + H_2$ (2)

$CH_4 + 2H_2O \rightarrow 4H_2 + CO_2$ (3)

Concerning the reactions that produce catalyst deactivation by Carbon deposition, surface coking is produced by CH_4 decomposition (eq. 4), Boudouard reaction (eq. 5) and ethanol dehydration to ethylene (eq. 6), followed by surface polymerization and carbon deposition.

$CH_4 \rightarrow 2H_2 + C$ (4)

$2CO \leftrightarrow CO_2 + C$ (5)

$C_2H_5OH \rightarrow C_2H_4 + H_2O$ (6)

When unmodified silica MCM-41 was used as catalytic support, the Ni/MCM-41 catalyst swiftly deactivated after 6h on stream, from a starting value of 88% to a final value of 52% in ethanol conversion. The molar fraction for all products remained constant and was 70% for H_2, 13% for CO_2, 12% for CO, 4% for CH_4 and traces of C_2H_4 (figure 9-a).

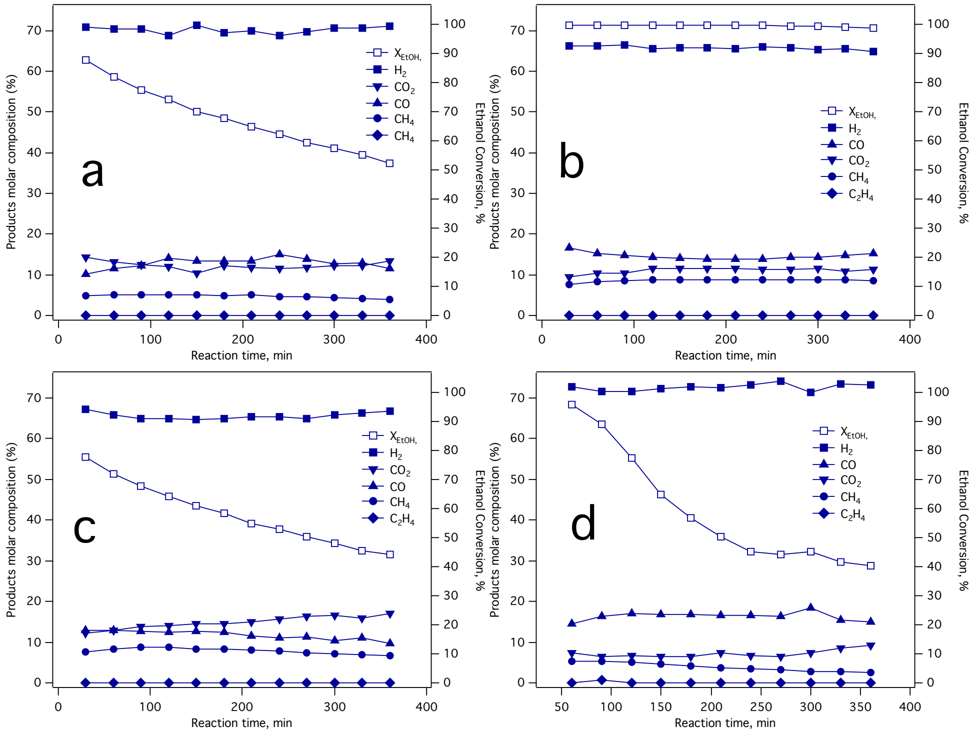

Figure 9. Ethanol conversion (right axis, light markers) and product distribution (left axis, dark markers) for Ni/xCe-MCM-41 catalyst in the ethanol steam reforming reaction: a) Ni/MCM-41 at 500°C; b) Ni/0.04CeMCM-41_MWUS at 500°C; c) Ni/0.02CeMCM-41_MWUS at 450°C d) Ni/0.02CeMCM-41 (Conventional synthesis, no US) at 500°C. (□ C_2H_5OH conversion, and product distribution for: ■H_2, ▲ CO, ▼ CO_2, ● CH_4. ♦ C_2H_4)

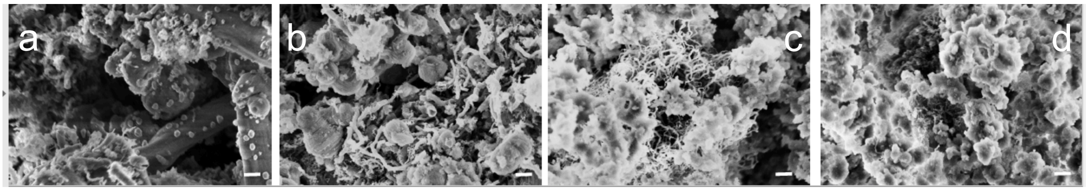

Figure 10. Nanocarbon filaments formation over a) Ni/MCM-41, b) Ni/0.02CeMCM-41_US, c) Ni/0.04CeMCM-41_US and d) Ni/0.06CeMCM-41_US after 6h on reaction stream (Bar length = 200nm, magnification 100kX)

On the other hand, cerium promoted silica (0.02CeMCM-41_MWUS, fig. 9b) resulted in complete hydrogen conversion at 500°C while product distribution was 65% H_2, 11.4% CO_2, 15% CO, 8.6% for CH_4 and traces of C_2H_4. The lower methane molar fraction for bare silica as support could be associated to CH_4 decomposition to carbon (eq. 4), which slightly increases the H_2 yield. For all cerium-containing catalytic supports, full ethanol conversion was achieved and the main product distribution was not significantly dependent on Cerium content. Hydrogen selectivity ranged from 60 to 65%, CH_4 from 8.5 to 10% and no traces of acetaldehyde or C2 products were detected. Similarly, hydrogen selectivity was found to be independent of Ce content on MCM-41 for a Rh over Ce-MCM-41 catalyst, while ethanol conversion was reported to decrease at higher cerium loads (Si/Ce = 10) in the catalytic support[24]. Figure S3† shows the ethanol conversion and product distribution graphs for mesoporous sieves at higher Ce/Si molar ratio (0.04, 0.06 and 0.08). At higher Ce/Si molar ratios (over 0.04), CO selectivity dropped from 15 to 7%, suggesting that oxidation of CO to CO_2 is enhanced by the oxygen storage capacity and oxidative reactivity of the cerium species in the mesoporous structure[15]. The stability and ethanol conversion of the Ce-promoted mesoporous silica can be attributed to the convertibility of $Ce^{4+} \Leftrightarrow Ce^{3+}$ in the catalyst surface. The reduced Ce^{3+} sites produce H_2O dissociation to form OH^- surface groups, which catalyse the reforming of C1 species (eq. 3). This reaction pathway was reported before for a Ni catalyst supported on Cubic CeO_2[43].

In order to analyse the ethanol conversion and hydrogen selectivity at a lower temperature level, the ESR was carried out on 0.02CeMCM-41MWUS at 450°C (figure 9-c). While a similar product distribution was observed, the Ni catalyst was less active at this temperature since ethanol conversion dropped from 77 to 44% after 6h on stream. H_2 selectivity was above 65% and the catalyst yielded lower CO and CH_4 in the products stream (compared to the same catalyst at 500°C), suggesting that after ethanol cracking, C1 products are carbonized via methane decomposition and Boudouard reactions (eq. 4 and 5). For comparative purposes, a sample prepared with conventional hydrothermal synthesis without US for Ce dispersion was also used as catalytic support. For this material, a swift catalyst deactivation is also observed. After achieving high ethanol conversion during the first hour on stream, the final value was below 40%. Product distribution was found to be 73% for H_2, 15% for CO, 9%for CO_2 and 2%for CH_4. A higher carbon monoxide yield, compared to the US-synthesized supports, could be indicative of a poor distribution of the Ce species that do not catalyse complete oxidation from CO to CO_2. Carbon deposition for this particular sample could be associated to methane decomposition, since CH_4 composition was the lowest for all catalyst. A further screening on the Ce/Si ratios for the catalytic support and Ni loading is beyond the scope of this study since the properties of the parent material MCM-41 are no longer preserved.

Figure 10 shows the graphitic carbon formation on Ni/xCe-MCM-41_US catalysts. For all the Ce-promoted silicas, only traces of ethylene were observed (below 0.1%), which suggest that after ethanol dehydration (eq. 6), ethylene quickly polymerizes resulting in carbon deposition. Nevertheless, the Ce modified mesoporous silica provides a suitable matrix for the immobilization of the Ni species since no metallic sintering was observed. The distribution of the Ce species in hexagonally ordered catalytic sieve resulted in formation of carbon nanofibers rather than aggregated carbon. A reaction mechanism for the formation of carbon nano-filaments has been reported over another transition metal catalyst [44]. The hexagonal structure and surface features of Ce-MCM-41 used as catalytic support result in a controlled growth of carbon nanofibers that do not produce catalyst deactivation by carbon poisoning. Cerium incorporation to the support favours the formation of smaller carbon filaments (Fig. 10), even at the lowest concentration used in the present research.

4. Conclusions

Cerium incorporation on mesoporous silica MCM-41 was achieved by ultrasound assisted direct hydrothermal synthesis. Depending on the Ce/Si molar ratios in the sample, two different Ce incorporation mechanisms were favoured: isomorphic substitution in the silica network and condensation in extra framework clusters. The sonochemical methodology enhanced cerium dispersion along the hexagonal framework yielding ordered sieves even at high Ce/Si molar ratios. Further, the use of a coaxial applicator for in-situ microwave irradiation allowed the reduction of the hydrothermal synthesis time while preserving hexagonal ordering and achieving higher surface area compared to materials prepared under conventional hydrothermal synthesis. The use of US coupled with MW irradiation for thermal activation represents an innovative approach that can be implemented for tuning the textural properties of other types of materials prepared under solvothermal synthesis and the use of amphiphilic molecules. The cerium-modified materials exhibit high surface areas and were tested as catalytic supports. Cerium promoted silica resulted in a better catalytic support for the ESR reaction compared to the bare MCM-41, since complete ethanol conversion, high H_2 selectivity (65%) were achieved and no catalyst deactivation occurred or C2 products formation. The presence of the heteroatom in the mesoporous sieve modified the morphology and chemical behaviour of the catalyst, resulting in an ordered deposition of carbon nano-filaments that do not induce catalyst deactivation.

Acknowledgements

The authors wish to acknowledge the National Council of Science and Technology, CONACYT México (project CB-2010-158193) and the Consorzio per lo Sviluppo dei Sistemi a Grande Interfase (CSGI), for providing financial support. The authors would like to thank M. F. Hernández Madera (U. Gto.), M. A. Vera Ramírez and A. M. Murrieta Castañeda (UAM-I) for their valuable technical support

References

1 D. P. Serrano, J. M. Coronado, V. A. de la Peña O'Shea, P. Pizarro and J. Á. Botas, *J. Mater. Chem. A*, 2013, **1**, 12016.
2 S. P. Jiang, *J. Mater. Chem. A*, 2014, **2**, 7637.
3 W. S. Chiang, E. Fratini, P. Baglioni, D. Georgi, J. H. Chen and Y. Liu, *J. Phys. Chem. C*, 2016, **120**, 4354–4363.
4 W.-S. Chiang, E. Fratini, P. Baglioni, J.-H. Chen and Y. Liu, *Langmuir*, 2016, **32**, 8849–8857.
5 R. He, W. Li, D. Deng, W. Chen, H. Li, C. Wei and Y. Tang, *J. Mater. Chem. A*, 2015, **3**, 9789–9798.
6 Z. Zhang, D. L. Santangelo, G. Ten Brink, B. J. Kooi, J. A. Moulijn and I. Melián-Cabrera, *Mater. Lett.*, 2014, **131**, 186–189.
7 C. T. Kresge and W. J. Roth, *Chem. Soc. Rev.*, 2013, **42**, 3663.
8 A. Taguchi and F. Schüth, *Microporous Mesoporous Mater.*, 2005, **77**, 1–45.
9 R. Peng, D. Zhao, N. M. Dimitrijevic, T. Rajh and R. T. Koodali, *J. Phys. Chem. C*, 2012, **116**, 1605–1613.
10 M. Tanaka, A. Itadani, Y. Kuroda and M. Iwamoto, *J. Phys. Chem. C*, 2012, **116**, 5664–5672.
11 E. P. E. P. Reddy, B. Sun and P. G. P. G. Smirniotis, *J. Phys. Chem. B*, 2004, **108**, 17198–17205.
12 S. Askari, S. Miar Alipour, R. Halladj and M. H. Davood Abadi Farahani, *J. Porous Mater.*, 2013, **20**, 285–302.
13 G. A. Tompsett, W. C. Conner and K. S. Yngvesson, *ChemPhysChem*, 2006, **7**, 296–319.
14 I. Longo and A. S. Ricci, *J. Microw. Power Electromagn. Energy*, 2007, **41**, 4–19.
15 C. T. Campbell and C. H. F. Peden, *Science*, 2005, **309**, 713–4.
16 A. M. Akondi, R. Trivedi, B. Sreedhar, M. L. Kantam and S. Bhargava, *Catal. Today*, 2012, **198**, 35–44.
17 O. A. González Vargas, J. A. de los Reyes Heredia, A. Montesinos Castellanos, L. F. Chen and J. A. Wang, *Mater. Chem. Phys.*, 2013, **139**, 125–133.
18 W. Yao, Y. Chen, L. Min, H. Fang, Z. Yan, H. Wang and J. Wang, *J. Mol. Catal. A Chem.*, 2006, **246**, 162–166.
19 J. C. Guevara, J. A. Wang, L. F. Chen, M. A. Valenzuela, P. Salas, A. García-Ruiz, J. A. Toledo, M. A. Cortes-Jácome, C. Angeles-Chavez and O. Novaro, *Int. J. Hydrogen Energy*, 2010, **35**, 3509–3521.
20 D. Li, L. Zeng, X. Li, C. Zhang, X. Wang, H. Ma, S. Assabumrungrat and J. Gong, *Appl. Catal. B Environ.*, 2015, **176**–**177**, 532–541.
21 Y. Fu, Y. Wu, W. Cai, B. Yue and H. He, *Sci. China Chem.*, 2015, **58**, 148–155.
22 I. A. Carbajal Ramos, T. Montini, B. Lorenzut, H. Troiani, F. C. Gennari, M. Graziani and P. Fornasiero, *Catal. Today*, 2012, **180**, 96–104.
23 V. Palma, F. Castaldo, P. Ciambelli and G. Iaquaniello, *Appl. Catal. B Environ.*, 2014, **145**, 73–84.
24 O. A. González Vargas, J. A. de los Reyes Heredia, J. A. Wang, L. F. Chen, A. Montesinos Castellanos and M. E. Llanos, *Int. J. Hydrogen Energy*, 2013, **38**, 13914–13925.
25 J. Vicente, J. Ereña, C. Montero, M. J. Azkoiti, J. Bilbao and A. G. Gayubo, *Int. J. Hydrogen Energy*, 2014, **39**, 18820–18834.
26 J. S. Beck, J. C. Vartuli, W. J. Roth, M. E. Leonowicz, C. T. Kresge, K. D. Schmitt, C. T. W. Chu, D. H. Olson and E. W. Sheppard, *J. Am. Chem. Soc.*, 1992, **114**, 10834–10843.
27 J. González-Rivera, I. R. Galindo-Esquivel, M. Onor, E. Bramanti, I. Longo and C. Ferrari, *Green Chem.*, 2014, **16**, 1417–1425.
28 T. N. Blanton, M. Rajeswaran, P. W. Stephens, D. R. Whitcomb, S. T. Misture and J. a. Kaduk, *Powder Diffr.*, 2012, **26**, 313–320.
29 J. González-Rivera, J. Tovar-Rodríguez, E. Bramanti, C. Duce, I. Longo, E. Fratini, I. R. Galindo-Esquivel and C. Ferrari, *J. Mater. Chem. A*, 2014, **2**, 7020.
30 B. Cordero, V. Gómez, A. E. Platero-Prats, M. Revés, J. Echeverría, E. Cremades, F. Barragán and S. Alvarez, *Dalt. Trans.*, 2008, 2832–2838.
31 C.-G. Wu and T. Bein, *Chem. Commun.*, 1996, 925–926.
32 B. L. Newalkar, S. Komarneni and H. Katsuki, *Chem. Commun.*, 2000, **3**, 2389–2390.
33 P. S. Goyal and V. K. Aswal, *Curr. Sci.*, 2001, **80**, 972–979.
34 S. H. Park, B. Y. Song and T. G. Lee, *J. Ind. Eng. Chem.*, 2008, **14**, 261–264.
35 S. M. Holmes, V. L. Zholobenko, A. Thursfield, R. J. Plaisted, C. S. Cundy and J. Dwyer, *J. Chem. Soc. Faraday Trans.*, 1998, **94**, 2025–2032.
36 S. C. Laha, P. Mukherjee, S. R. Sainkar and R. Kumar, *J. Catal.*, 2002, **207**, 213–223.
37 M. Thommes, K. Kaneko, A. V. Neimark, J. P. Olivier, F. Rodriguez-Reinoso, J. Rouquerol and K. S. W. Sing, *Pure Appl. Chem.*, 2015, **87**, 1051–1069.
38 D. Gulkova and Z. Vit, *Appl. Catal. A Gen.*, 1995, **125**, 61–70.
39 Y. Li, Q. Fu and M. Flytzani-Stephanopoulos, *Appl. Catal. B Environ.*, 2000, **27**, 179–191.
40 N. Wu, W. Zhang, B. Li and C. Han, *Microporous Mesoporous Mater.*, 2014, **185**, 130–136.
41 S. Qiu, X. Zhang, Q. Liu, T. Wang, Q. Zhang and L. Ma, *Catal. Commun.*, 2013, **42**, 73–78.
42 A. Haryanto, S. Fernando, N. Murali and S. Adhikari, *Energy & Fuels*, 2005, **19**, 2098–2106.
43 W. Xu, Z. Liu, A. C. Johnston-Peck, S. D. Senanayake, G. Zhou, D. J. Stacchiola, E. A. Stach and J. A. Rodriguez, *ACS Catal.*, 2013, **3**, 975-984.
44 S. Jankhah, N. Abatzoglou, F. Gitzhofer, J. Blanchard and H. Oudghiri-Hassani, *Chem. Eng. J.*, 2008, **139**, 532–539.

Paper II

A green microwave-assisted synthesis of hexagonally ordered silica sieves using a geothermal waste as silicon precursor and their use as Zn catalytic supports for carbonylation of glycerol.

Authors: J. Tovar Rodríguez, J. González Rivera, C. Ferrari, I. Longo, M. Onor, P. Baglioni and E. Fratini

Submitted to Wiley-VCH ChemSusChem Energy and Materials

A green microwave-assisted synthesis of hexagonally ordered silica sieves using a geothermal waste as silicon precursor and their use as Zn catalytic supports for carbonylation of glycerol.

J. Tovar Rodriguez,[a] J. González Rivera, [b] C. Ferrari,[b] I. Longo, [b] M. Onor,[c] P. Baglioni[a] and E. Fratini*[a]

Abstract: A series of template-based mesoporous molecular silicas were prepared using a non-conventional silicon source. Microwaves irradiation by means of an innovative coaxial applicator were used for thermal activation. All prepared materials feature hexagonal ordering, narrow pore size distribution and high surface areas (over $500 m^2/g$). By changing the parameters of the solvothermal synthesis, it is possible to tune the ordering and textural properties of the mesophases and reduce the reaction time. These materials were used as a Zn catalytic support for the solventless conversion of glycerol to glycerol carbonate.

Introduction

Silicon-based nanostructured sieves constitute a special class of self-assembled materials that can find a broad range of applications due to a unique set of characteristics: they exhibit large surface areas, hexagonally ordered structure, narrow pore size distribution[1] and these features make them suitable materials for catalysis[2]; as support for enzymes and proteins[3]; as drug carriers[4] and for adsorption purposes[5]. Their synthesis involves the use of amphiphilic molecules as structure directing agents and is typically carried out in solvothermal conditions. Therefore, given its widespread use and applications the need for greener and sustainable chemical synthesis routes has become a constant research effort.

Considering the reaction mechanism of the surfactant-template process to synthesize highly ordered materials, several approaches have been developed to reduce the synthesis time or to find less expensive and toxic reagents[6]. As alternative to conventional heating for solvothermal synthesis, the use of microwaves irradiation (MW) has proven to be an effective tool for thermal activation of chemical processes[7]. By depending on the dielectric properties of the media, microwaves makes possible selective heating, superheating, solventless heating approaches and a significant reduction of the overall synthesis time[8]. Several examples can be found in the literature addressing the synthesis and preparation of porous nanomaterials using MW irradiation for thermal activation[9]. Nonetheless, the most typical and commercially available oven-type microwave reactors feature a closed-box geometry [10,11]. Hence, suitable and novel reactor configurations for a broader range of operative conditions and efficient microwave application remain a challenge.

Regarding the silicon source, several chemical reagents can be used for the synthesis of micro and mesoporous materials under solvothermal conditions, being the alkoxy silanes (tetraethoxysilane, tetramethoxysilane), fumed silica, colloidal silica or soluble silicates, the most recurrent. However, these reagents are synthesized from toxic precursors, are generally expensive and could limit their use for large-scale preparation approaches. To overcome this issue, the use of natural sources like natural clays or recycled industrial wastes such as coal fly ash or rice husk fly ash[12] have been suggested as non-conventional silicon sources. Still, their widespread use faces the difficulty of obtaining large surface areas and pore volumes as those obtained by synthetic silicon precursors.

A growing need for finding energy sources to reduce oil dependency for economic and environmental reasons, biodiesel derived from non-edible triglycerides by transesterification with methanol, has attracted considerable attention during the past decade as an alternative fuel [13]. However, biodiesel industrial production is associated by stoichiometry to an inherent glycerol production as undesired product. Therefore, given its low toxicity and biodegradability, glycerol has the potential to be both an excellent renewable solvent in modern chemical processes and a versatile building block in biorefineries[14]. However, these potential applications require the development of adequate catalysts for a specific synthesis route or application.

In this context, the synthesis of glycerol carbonate (glycerin carbonate or 4-hydroxymethyl- 2-oxo-1,3-dioxolane) to revalorize glycerol crudes is an effective alternative. Glycerol carbonate can find several applications as solvent, curing agent, cosmetics synthesis, in lithium batteries, as liquid membrane for gas separation and as blowing agent[15]. Among the most frequent synthesis routes, glycerol carbonylation is typically run with carbonylating agents, by reaction of glycerol with CO_2 under supercritical conditions, dimethyl carbonate[16], and urea[17], under milder reaction conditions. Among these reagents, urea is a particularly attractive carbonylating agent due to the mild reaction conditions and high selectivity. Therefore, developing a heterogeneous catalyst for this process has strategic and environmental benefits[18].

In this work, we present a novel integrated green approach to synthesize self-assembled mesoporous molecular sieves. By modifying the reaction parameters, several silicon-based mesophases were prepared using a geothermal industrial waste

---

[a] Dr. J. Tovar-Rodriguez, Dr. E. Fratini and Dr. P. Baglioni
Dipartimento di Chimica "Ugo Schiff", Consorzio per lo Sviluppo dei Sistemi a Grande Interfase CSGI. Università degli Studi di Firenze. Via della Lastruccia 3, 50019, Sesto Fiorentino, Firenze. Italia
E-mail: fratini@csgi.unifi.it
[b] C. Ferrari, I. Longo, J. Gonzalez Rivera,
Consiglio Nazionale delle Ricerche, Istituto Nazionale di Ottica – Pisa. Via Giuseppe Moruzzi 1, 56124. Pisa, Italia
[c] M. Onor
Consiglio Nazionale delle Ricerche, Istituto di Chimica dei Composti Organometallici UOS UOS – Pisa. Via Giuseppe Moruzzi 1, 56124. Pisa, Italia.

Table 1. Elemental analysis for the Geothermal Silica precursor.

Sample	At %								Atomic ratios	
	O	Si	Al	Fe	Na	Cl	K	As	Si/Al	Si/Fe
GeoWaste[A]	80.47	18.56	0.26	0.25	0.08	0.18	0.08	0.11	72.08	73.46
GeoWaste[B]	77.05	22.30	0.19	0.31	-	-	0.01	0.14	115.26	72.23

[a] as received from the geothermal field [b] After being crushed, sieved and washed with a 0.5M HCl solutio

as silicon source using microwaves for thermal activation. These materials were used as Zn catalytic supports for the microwave-assisted solventless carbonylation of glycerol using urea. Due to the dielectric properties of glycerol as solvent, this novel reaction approach offered several advantages compared to conventional heating.

Results and Discussion

Geothermal silica waste Si precursor.

Initial characterization of the geothermal waste was performed to assess its feasibility as adequate silicon precursor. Figure 1 shows the particle morphology for GeoWaste after being crushed, sieved (MESH 150) and washed with a 0.5M solution of HCl. The starting material consists of polydisperse round-like silica particles with variable sizes, ranging from 4 up to 30nm in diameter. Elemental analysis was performed by means of Energy-dispersive X-ray spectroscopy and the composition of the geothermal waste is expressed on table 1 in terms of percentage atomic content.

As-received geothermal silica is composed mainly of silicon dioxide, with less than 0.5% of impurities, being the most abundant Al and Fe. After washing with HCl 0.5M the soluble species, which are presumably in the form of chlorides, (NaCl and KCl) are removed. For Al and Fe, the Si/Al and Si/Fe atomic ratios were calculated (Table 1 Si/Al and Si/Fe columns). It is noteworthy that after acid treatment the amount of Al in the sample decreases, suggesting that dealumination of the silica matrix may be occurring. This phenomenon is well documented for aluminosilicates such as zeolites[22], and the extent of Al loss depends on the dealumination agent and the selected reaction conditions. On the other hand the abundance of Fe does not seem to change after HCl washing since the atomic ratio Si/Fe remains constant. The relative abundance of Si compared to O is consistent with tetra-coordinated silicon species.

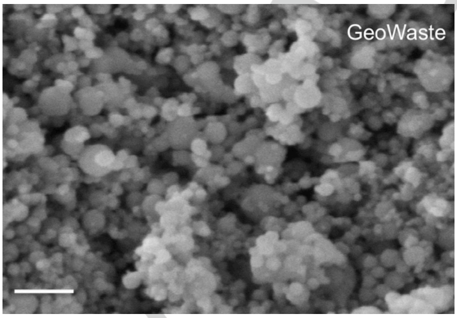

Figure 1. Scanning Electron Micrograph for the geothermal waste used as Si precursor (Bar length = 100nm, magnification 400kX).

Small angle X-ray scattering curves

Figure 2 shows the Small Angle X-ray scattering curves for the silicon precursor, the mesoporous silica sieve prepared with the geothermal waste under conventional hydrothermal synthesis and mesoporous MCM-41 synthesized using TEOS, in the low Q scattering vector interval from 0.05 to 0.05Å^{-1}. The as-received geothermal silica waste shows no diffraction peaks in the explored Q interval, suggesting that the sample is composed entirely of amorphous silicon dioxide. On the other hand, calcined mesoporous silica MCM-41 features a well-resolved scattering pattern, with a main diffraction peak centered at a reciprocal Q values of 0.165 Å^{-1}. Other secondary Bragg peaks are found at 0.286, 0.33 and 0.434Å^{-1}.

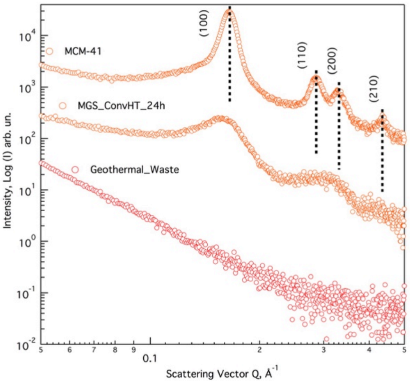

Figure 2. Small Angle X-ray Scattering curves for mesoporous silica MCM-41; Mesoporous geothermal silica and the Geothermal Silica Waste, after calcination.

Table 2. Textural properties and lattice cell parameters for the prepared mesoporous sieves using a geothermal waste as Si precursor

Sample	HT time, h	S_{BET}, m^2/g	V_{Pore}, cm^3/g	D_{Pore}, nm	d_{100}, Å	a_0, Å
GeoWaste	0	45	0.22	n.d[&]	0	0
MGS_MWHT_2[§]	2	617	0.73	4.7	43.3	50.0
MGS_MWHT_4[§]	4	546	0.69	4.45	43.7	50.5
MGS_MWHT_6[§]	6	707	0.70	3.97	44.8	51.7
MGS_ConvHT_24[*]	24	655	0.62	3.77	45.5	52.5
MCM-41_ConvHT_24[*]	24	923	0.79	3.47	44.8	51.2

[*] Synthesized under conventional hydrothermal synthesis, [§]Synthesized with microwaves for thermal activation, S_{BET} BET Surface area, V_{Pore} Total pore volume calculated at a relative pressure Ps/Po = 0.9814, D_{pore} Pore diameter calculated as $D = 4*V_{pore}/S_{BET}$, [&] Non-determined due to a broad BJH pore distribution

These diffraction peaks can be indexed to the reflections of the (100), (110), (200) and (210) *hlk* planes for the hexagonal structure, space group *p6mm*[23]. The interplanar distance d_{100} was calculated by interpolation using the Q values for these reflections and Bragg's law, $\lambda = 2d_{hlk}*\sin\theta$. For a hexagonal structure, the dependence between the lattice constant a_0 and the interplanar distance is given by $a_0 = 2d_{100}/\sqrt{3}$. Table 2 summarizes the lattice parameter a_0 and interplanar distances d_{100}, calculated for all prepared solids after calcination. Mesoporous geothermal silica prepared under conventional hydrothermal synthesis (MGS_ConvHT_24h), features a main scattering peak that is slightly shifted to a lower reciprocal Q value of 0.159Å^{-1}, which results in a d_{100} spacing and a_0 constant of 45.5 and 52.5Å, respectively (compared to 44.8 and 51.2Å for pure siliceous MCM-41). The structural and lattice parameters of template-based mesoporous silica depend entirely on the length of the surfactant alkylic chain[24] and in the absence of co-solvents or co-surfactants, the closely obtained parameters are in agreement with previously reported values for mesoporous MCM-41[20]. For MGS_ConvHT_24, a second broad scattering peak with a maximum intensity on Q = 0.16Å^{-1} can be interpreted as the convolution of the (110) and (200) peaks. Finally, the least-resolved Bragg peak could be assigned to the scattering of the (210) plane for the hexagonal structure. Figure 3 shows the SAXS curves for the samples prepared under microwave-assisted hydrothermal synthesis. In a similar fashion, all prepared sieves feature a main Bragg diffraction peak with secondary less-resolved peaks at higher Q values. A sample prepared under the longest irradiation time (MGS_MWHT_6h), exhibits an interplanar distance and lattice constant value that are the closest to that of the parent MCM-41 material (Table 2, d_{100} and a_0 columns). Although no significant shift for the main scattering peak are observed, its intensity seems to increase with the hydrothermal synthesis time. Nonetheless, the microwave-assisted solvothermal methodology here reported enables ordered mesophases in a fraction of the typically required conventional hydrothermal time[25].

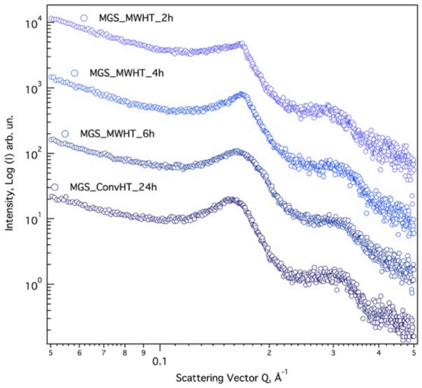

Figure 3. Small Angle X-ray Scattering curves for Mesoporous geothermal silica obtained at different MW irradiation times and conventional heating.

To improve the hexagonal ordering of the prepared mesoporous silicas and to better understand the formation mechanism, SAXS curves were recorded in liquid solvent for the synthesis colloid before ageing and hydrothermal treatment. Figure 4a shows the scattering curve for the precursor colloid using TEOS as Si source with the following molar composition: $1.0(CH_3CH_2O)_4Si$: 0.30CTABr : $20NH_3$: $210H_2O$, recorded right after TEOS additions (total acquisition time, 1800s). From the scattering patter, a possible formation mechanism of the hexagonal structure can be elucidated: Under the strong basic conditions (pH = 12.7) the alkoxide molecules are rapidly hydrolyzed an interact with the positively charged micelles which group in hexagonal domains. A main scattering peak is observed located at Q = 0.147Å^{-1}. This value shifts to 0.165Å^{-1} after calcination (Fig. 2) due to thermal contraction of the silica network[26]. From Bragg's law, the distance between two scattering centers can be estimated as 42.7 Å.

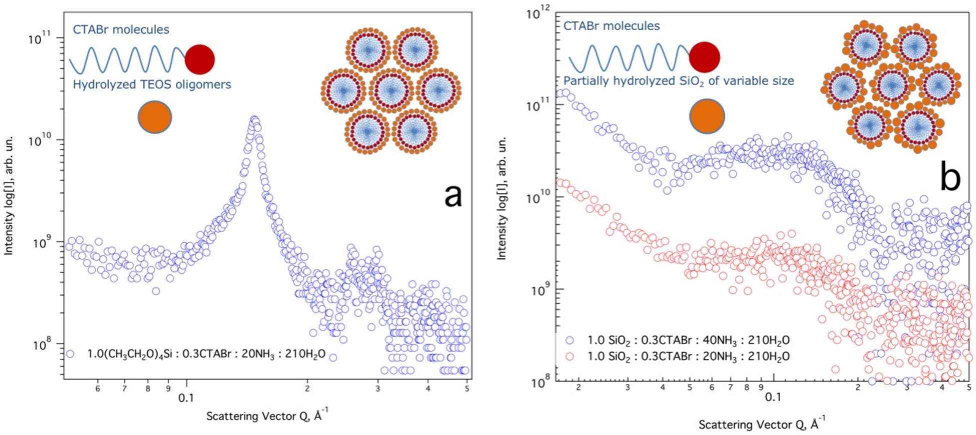

Figure 4. SAXS curves for the colloidal synthesis using a) TEOS and b) geothermal silica waste as Si precursors

This value is comparable with the micellar radii recently reported[27] for CTABr/TEOS mixtures under basic conditions (molar ratio 1:1, pH = 10). For the geothermal waste as Si precursor, the synthesis colloid had the following molar composition: 1.0SiO$_2$: 0.30CTABr : 20NH$_3$: 210H$_2$O. Under identical acquisition conditions a broad curve can be observed (Fig. 4b), which suggests that the cationic micelles interact with the partially hydrolyzed Si particles of variable sizes and tend to group in less defined hexagonal structures. By increasing the amount of mineralizing agent by a twofold factor (1.0SiO$_2$: 40NH$_3$), the center of the scattering curve does not change significantly (From Q = 0.093 to 0.095Å^{-1}). Therefore, a reduced amount of NH$_4$OH solution as silica mineralizing agent was selected for all synthesis. The distance between scattering centers was estimated as 67.6 and 66Å and its value is consistent with micellar arrangements of thicker silica walls. For these materials, Si particles hydrolysis and consequent diffusion towards the micelle may be limited by their size. Nonetheless, after silica polymerization by microwave-assisted hydrothermal treatment, the obtained silica sieves feature hexagonal structures with d$_{100}$ spacing comparable to the MCM-41 parent material. Inset figures 4a-b show a graphical representation of the possible micelle formation mechanism previously discussed.

Textural properties and N$_2$ adsorption and desorption isotherms

The textural properties for all prepared materials were evaluated by means of N$_2$ adsorption and desorption isotherms. Table 1 summarizes the Brunauer-Emmett-Teller surface area and pore volume for all calcined solids. The as received geothermal waste has a surface area of 45m^2/g whereas the highest area observed was 923m^2/g for mesoporous MCM-41. For the mesoporous geothermal silica series, the surface area can be tailored in the interval from 550 to 700m^2/g, depending on the overall hydrothermal treatment time. For the sake of time and energy savings, no longer microwave-assisted synthesis times were explored. In a similar manner, the largest total pore volume (evaluated at a relative pressure of P$_s$/P$_0$ = 0.9814) was 0.79cm^3/g for MCM-41 while pore capacity increased from 0.22 up to 0.73cm^3/g, for the geothermal waste after solvothermal synthesis.

Figure 5a-f shows the N$_2$ adsorption and desorption isotherm curves for all calcined mesoporous materials whereas inset figures show the pore volume distribution obtained with the desorption branch of the isotherm and the Barrett-Joyner-Halenda model. The starting material GeoWaste features a type II isotherm according to the classification made by IUPAC[28], which is characteristic of macroporous adsorbents. On the other hand, for the mesoporous silica series all materials exhibit a type IV(b) isotherm which is characteristic of substrates with pore sizes up to 50nm. Four well-defined portions in the isotherm curve can be described: a) Micropore filling and monolayer formation occur at very low P$_s$/P$_0$ values (up to 0.03), denoted by a relatively large nitrogen uptake. For GeoWaste the monolayer capacity was the lowest observed; b) Unrestricted multilayer formation is distinguished by an inflexion point and slope change, followed by linear region in the isotherm curve; c) Nitrogen capillary condensation within the mesopores is identified by the presence of a second inflexion point at relative pressure values close to 0.3 followed by a significant amount of adsorbed nitrogen. Such feature is not present in the geothermal waste. For MCM-41 a sharp steep is observed whereas the geothermal silicas exhibit a smooth slope. Finally, d) Inter particle adsorption

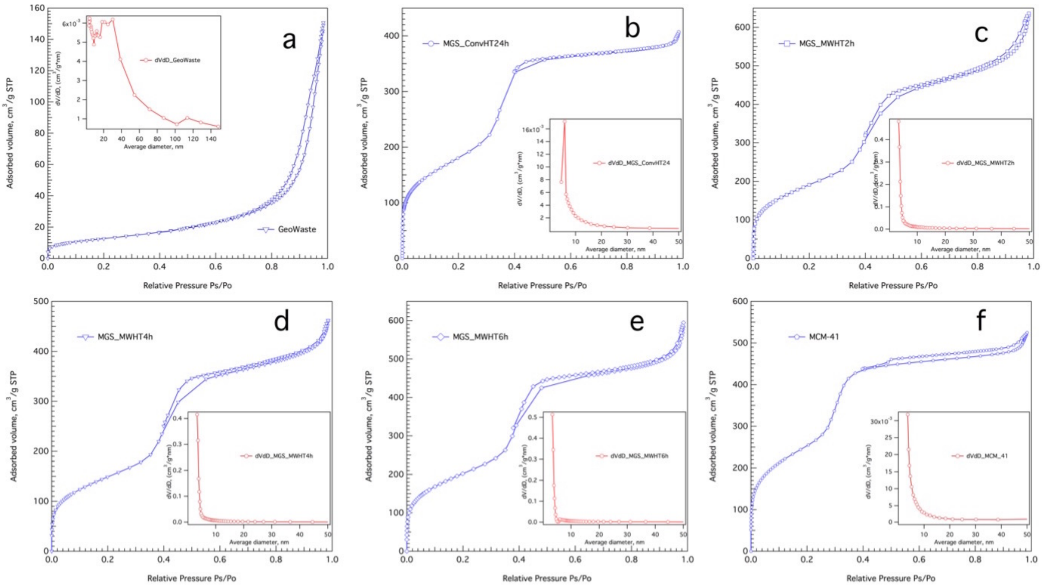

Figure 5. Nitrogen adsorption/desorption isotherms for a) Geothermal Waste and the synthesized Mesoporous Geothermal Silicas MGS: b) Conventional hydrothermal synthesis 24h, c) Microwave-Assisted Hydrothermal Synthesis (MWHT) 2h, d) MWHT_4h ; e) MWHT_6h and f) MCM_41. Inset figures: BJH pore volume distribution..

is denoted by a final saturation plateau at high relative pressure areas (over P_s/P_0 = 0.94). Concerning the Barrett-Joyner-Halenda graphs, the silicon precursor shows a broad pore size distribution with no average pore size. For the rest of the prepared materials, a narrow pore size distribution is observed, indicative of a monomodal distribution of pores with cylindrical geometry and open endings. An average pore diameter was calculated as D_{pore} = $4*V_{pore}/S_{BET}$ (Table 2 D_{pore} entry). As the hydrothermal synthesis time increases, the pore size tends to narrow from 4.7 to 3.47nm (for MCM-41), suggesting that longer synthesis times favor irreversible silica polymerization and micelle packing into narrower and elongated worm-like structures. This phenomenon was described in terms of micelle concentration for CTABr/NaSal solutions[29]. Such variation in pore size result in a small width type H1 hysteresis loop for samples prepared after 2, 4 and 6 h of solvothermal treatment. MGS_ConvHT_24h and MCM-41 feature the smallest pore diameter and an almost reversible isotherm curve. For MCM-41 a parallel loop over a long interval of relative pressure may be associated to particle aggregate adsorption rather than capillary effects[28].

^{29}Si and ^{1}H MAS-NMR Spectroscopy

Nuclear magnetic resonance spectroscopy provided additional information concerning the structural environment of two nuclei in the silicon sieve. Figure 6a-b shows the ^{29}Si and ^{1}H MAS-NMR spectra for the geothermal waste as starting material and the hexagonally ordered mesoporous silicate. The as-received geothermal waste has a sole broad spectral signal with a maximum at -112ppm (using TMS as standard) that is indicative of Q^4 siloxane species. For the mesoporous sieve, two other crests are observed at around -102 and -92 ppm. These signals are typically associated to the resonances of Q^3 and Q^2 nuclei which belong to isolated and geminal silanol groups (Si(OH) and $Si(OH)_2$ surface groups).

To obtain individual information of the Si nuclei in the structure, deconvolution of these signals was performed around the chemical shift values of -112, -102 and -92ppm, for Q^4, Q^3 and Q^2 species.

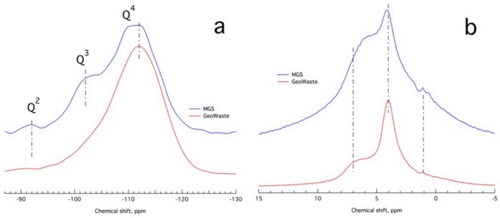

Figure 6. ^{29}Si and ^{1}H solid-state HP-DEC MAS-NMR spectra for the geothermal waste and the mesoporous geothermal silica.

Table 3. Q^n distributions for the Si species in GeoWaste and MGS calcined samples.

Sample	Q^4	Q^3	Q^2	$(Q^2+Q^3)/Q^4$
GeoWaste	5.56	0.60	0	0.11
MGS	4.57	1.49	0.09	0.34

Table 3 summarizes the Q^n distribution for both calcined solids. After hydrothermal synthesis, the relative amount of total-silanol/siloxane $((Si(OSi)_3OH)+ Si(OSi)_2(OH)_2)/(Si(OSi)_4)$ ratio increased from 0.11 to 0.34. A higher recurrence of silanol groups could be indicative of material with improved surface reactivity since silanol are considered as catalytic Bronsted sites and the Si-OH moiety is particularly important for surface functionalization or grafting of these silicates[30]. The ^1H NMR spectra further confirms the surface silanol enrichment for mesoporous geothermal silica (Fig 6b). For both samples, a main signal can be found at 4ppm chemical shift, that can be associated to physisorbed water on the surface of the material. After hydrothermal synthesis, a broadening of the signal around 7ppm could be indicative of a material with a larger number of both single and geminal Si-OH groups[31].

Scanning electron micrographs for Mesoporous Geothermal Silica

Figure 7 shows the SEM micrographs for calcined samples. After hydrothermal treatment, the resulting materials change from spherical particles to a flake-like morphology, which is characteristic of mesoporous silica MCM-41 (Fig. 7d). For the sample prepared under microwave-assisted solvothermal synthesis (7c), tubular particles of variable length were observed which may be the result of a quicker heating produced by MW. This particular morphology has been described for halloysite minerals[32] and is typically associated to silica with low Fe content.

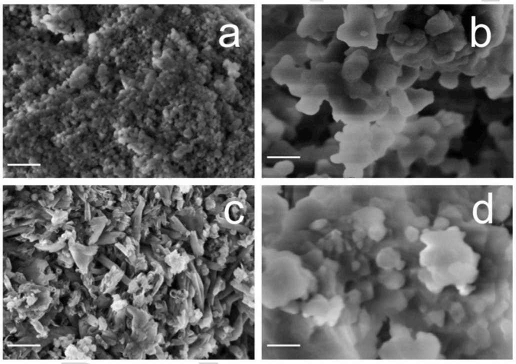

Figure 7. SEM Micrographs for: (a) Geothermal waste; (b) MGS_ConvHT24h; (c) MGS_MWHT_6h and (d) MCM-41 (Bar length = 200nm, magnification 200kX for all micrographs).

Catalytic evaluation of Zn/MGS in the carbonlylation of glycerol.

To evaluate the feasibility of mesoporous geothermal silica as support, a Zn catalyst was prepared and tested in the solventless carbonylation of glycerol with urea. Figure 8 shows the glycerol conversion and product yield for a selected sample of Zn/MGS_MWHT_4h. For comparative purposes, MCM-41 was used as Zn catalytic support, according to a previously reported methodology[17]. After 60 minutes of reaction time, a glycerol conversion of 60% was reached and it remained unchanged after 120 minutes of reaction time. For MCM-41, the highest conversion value of 72% was reached (8% glycerol carbonate yield). Although with a lower glycerol conversion, the Zn/MGS catalyst showed good hydrothermal stability and the Al, and Fe impurities do not catalyze undesired side-reactions.

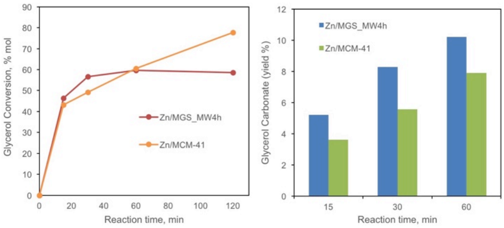

Figure 8. Glycerol conversion and glycerol carbonate yield for Z/MCM-41 and Zn/MGS_MWHT_4h after 120 minutes of reaction time.

Conclusions

A novel methodology for the synthesis of mesoporous molecular sieves using a geothermal waste as silicon precursor was described. By means of microwave-assisted hydrothermal synthesis, it is possible to revalorize an industrial waste and tune the ordering and textural properties of mesoporous silica. The innovative coaxial applicator enabled shorter reaction times, compared to conventional heating. The prepared materials were used in the solventless conversion of glycerol to glycerol carbonate using Zn as active phase, to demonstrate their usability as catalytic support. The methodology here proposed enables the realistic projection of a sustainable industrial process to synthesize mesoporous molecular sieves by making use of a cheap and readily available geothermal silicon precursor.

Experimental Section

Geothermal waste as silicon source for the synthesis of mesoporous materials.

A sample of inorganic geothermal waste was received from a geothermal field in the region of “Los Azufres”, MX (19°47'23"N, 100°39'57"W). This material was obtained from the condensation of the high-pressure vapors coming from a hot spring used in the electricity generation process. To adequate this sample to be used as a raw material for the synthesis of silica mesophases, the geothermal waste underwent the following treatment: 100g of this material were put in contact with 500ml of a HCl solution (0.5M) for 1h under atmospheric conditions and 300rpm of magnetic stirring. This aqueous dispersion was separated by centrifugation (3.5krpm) and the precipitated solid was dried at 90ºC for 24h. Afterwards, the geothermal waste was crushed and sieved to yield a maximum particle size of 105µm (using a MESH grid, 150 nominal size). Then, the sample was calcined to remove any organic impurities at 550ºC for 4h. This material is referred hereafter as geothermal waste (GeoWaste).

Synthesis of hexagonally ordered mesoporous silica using a geothermal waste.

To yield a hexagonally ordered mesoporous material, the geothermal industrial waste (GeoWaste) was used as building block in a soft-template preparation approach. The proposed green synthesis of the materials was performed by hydrothermal treatment, using a microwave-assisted teflon-lined stainless steel high-pressure reactor. The microwaves were applied in-situ by means of an innovative microwave coaxial antenna, which allows direct microwave application within the reaction system. The details concerning the construction and operation of the high-pressure reactor can be found elsewhere[19]. On the other hand, conventional hydrothermal synthesis was performed using a heating mantle. The structure-directing agent used was the quaternary cationic ammine hexadecyltrimethylammonium bromide (CTABr, Sigma-Aldrich) and ammonium hydroxide (NH_4OH, 30%wt Sigma-Aldrich) was used as mineralizing agent. The molar composition for the synthesis colloid was as follows: 1.0 SiO_2 : 0.30 CTABr : 20 NH_3 : 210 H_2O. In a typical synthesis, 1.43g of CTABr were dissolved in 25ml of deionized water. Then, 0.8g of geothermal waste (GeoWaste) were mixed with 17.5ml of NH_4OH and 14.13ml of deionized water. Both solutions were kept under vigorous stirring. Once the surfactant was completely dissolved, the GeoWaste emulsion was added dropwise and it was kept at 45ºC for 24 or 48h, to allow silica polymerization around the micellar formations. Then, this mixture was transferred to the high-pressure reactor to be hydrothermally treated at 100ºC for 2, 4 or 6 hours. For comparative purposes, a conventional silicon source (tetraethylortosilicate, TEOS $SiC_8H_{20}O_4$, 99% Sigma-Aldrich) was used for the preparation of hexagonally ordered mesoporous MCM-41 under hydrothermal treatment at 100ºC and 24h, according to a previously reported methodology[20]. For the preparation of MCM-41, the aforementioned molar ratios were used: 1.0 $(CH_3CH_2O)_4Si$: 0.30 CTABr : 20 NH_3 : 210 H_2O. After hydrothermal treatment was completed, all samples were washed with deionized water several times, dried overnight at 80ºC and calcined at 550ºC under static air to remove the surfactant occluded within the mesopores.

Synthesis of Mesoporous Geothermal Silica MGS-supported ZnO catalyst

Selected mesoporous geothermal silica samples were used as support for a ZnO catalyst (for a 5% of ZnO in the final material). In a typical synthesis, 300mg of a Zn precursor ($ZnSO_4 \cdot 7H_2O$ Sigma-Aldrich) were dissolved in 7.5ml of methanol. Then, 1.45g of dried mesoporous solid were put in contact with the Zn precursor solution. This mixture was transferred to an ultrasonic bath operating at a maximum frequency of 40kHz and was sonically dispersed for 30 minutes. The solvent excess was removed using a rotovapor. The resulting powder was dried overnight at 80ºC and annealed at 550ºC under static air to yield the oxidized Zn form.

Solventless Microwaves-assisted carbonylation of glycerol to glycerol carbonate

The prepared ZnO/MGS (mesoporous geothermal silica) catalysts were used for the synthesis of glycerol carbonate using glycerol and carbamide as reagents ($C_3H_8O_3$ 98% Sigma-Aldrich; $CO(NH_2)_2$, 99% Sigma-Aldrich) and microwaves irradiation for thermal activation. A green solventless approach was developed to carry out the carbonylation reactions: The reaction was performed in an ordinary glassware triple-neck round-bottom flask, possessing an open ending tube to place an innovative microwave applicator for in-situ microwaves irradiation. The coaxial applicator ending was placed at three quarters of the total length of the flask inner tube and a choke section was used to minimize reflected power towards the MW source[8]. The source of microwave consisted in a magnetron oscillator equipped with forward and reflected power indicators (SAIREM, Mod. GMP 03 K/SM), operating at a maximum of 300 W of continuous MW irradiation power at a frequency of 2.45 GHz. A Faraday cage-type enclosure was made by covering the flask with a largely sieved metallic continuous grid, allowing visual control of the reaction and a safety operation by eliminating non-absorbed radiation escaping the boundaries of the reactor. For a reflux set-up, a condenser was mounted on the middle neck, leaving one neck for a thermometric well and another one for sampling. A typical reaction was performed by loading 0.2mol of glycerol, a stoichiometric amount of urea (1:1 glycerol to urea molar ratio) and 0.92g of dried catalyst (for a 5% wt of catalysts, referred to the glycerol mass). The reaction was performed at 160ºC and samples were taken after 15, 30, 60, 90 and 120 minutes.

Characterization

Small angle X-ray scattering

SAXS measurements were carried out with a HECUS S3-MICRO camera (Kratky-type) equipped with a position-sensitive detector (OED 50M) containing 1024 channels of width 54 µm. Cu Kα radiation of wavelength λ = 1.542Å was provided by an ultra-brilliant point micro-focus X-ray source (GENIX-Fox 3D, Xenocs, Grenoble), operating at a maximum power of 50 W (50kV and 1mA). The sample-to-detector distance was 281 mm. The volume between the sample and the detector was kept under vacuum during the measurements to minimize scattering from the air. The Kratky camera was calibrated in the small angle region using silver behenate (d = 58.34Å)[21]. Scattering curves were obtained in the Q-range between 0.05 and $0.5Å^{-1}$, if Q is the scattering vector $Q = 4\pi/\lambda^* \sin\theta$, and θ is the scattering angle. Powder samples were placed into a 1 mm demountable cell having Kapton foils as windows. Liquid samples were mounted in a capillary tube (80mm length, 1.0mm diameter, wall thickness = 0.1mm). The temperature was set at 25ºC and was controlled by a Peltier element, with an accuracy of 0.1ºC. All scattering curves were corrected for the empty cell or capillary contribution considering the relative transmission factor.

Nitrogen physisorption analysis

Nitrogen adsorption and desorption isotherms were recorded using a Beckman Coulter SA 3100 Surface Area Analyzer. Calcined samples were outgassed prior to analysis in vacuum conditions ($P = 10^{-3}$mmHg) at a temperature of 200ºC for 2 hours. The specific surface area was calculated with the Brunauer-Emmett-Teller method (BET Method), and the size distribution and diameter were obtained with the desorption branch of the isotherm, using the Barrett-Joyner-Halenda (BJH) method.

Solid-state NMR spectroscopy

The ^{29}Si Solid-state Nuclear Magnetic Resonance spectra (MAS-NMR) of the powder samples were recorded using a Bruker AVANCE II NMR Spectrometer with a CPMAS H-X BB detector of 4mm, operating at a resonance frequency of 59MHz. The spin velocity of the sample was set at 5kHz and the recycling time between experiments was 10s using the High-Power Decoupling Cross-Polarization technique (HPDEC).

SEM Analysis

Morphology and particle size of the catalysts were analyzed using a SIGMA Field Emission Scanning Microscope (Carl Zeiss Microscopy GmbH, Germany). The micrographs were acquired from uncoated samples, using the In-Lens Secondary Electron detector. Elemental analysis was performed by means of Energy-dispersive X-ray spectroscopy for the starting silicon precursor material.

GC-MS spectroscopy

To determine glycerol conversion and product distribution, product samples were analyzed by means of gas chromatography coupled with mass spectrometry (GC-MS). An Agilent 6850 gas chromatograph, equipped with a split/splitless injector, was used in combination with an Agilent 5975c mass spectrometer. A CTC CombiPAL autosampler was employed for the liquid injections. A sample of 1µl was injected in split mode (split ratio 1:100) into the gas chromatograph. Then, the inlet liner (4mm internal diameter) was held at 250°C and the injection was performed in split mode. The column was kept under a constant helium flow rate of 1.2 mL/min). Compounds were then separated in a high polarity column (DB-FFAP; 60m length; consisting of terephtalic acid-modified carbowax stationary phase; 0.25 mm inner diameter; 0.5 µm coating) using the following temperature program: 5 min at 150°C, 10°C/min up to 230◦C held for 30 min (53 min total runtime). The temperature of the transfer line was set at 240°C. After GC separation, glycerol carbonate and glycerol were ionized in positive EI. The MS acquisition was performed in total ion chromatography TIC which allowed for the identification of glycerol and glycerol carbonate, whereas extracted Ion was implemented for quantitative purposes by monitoring m/z of 61, 87, 43 and 45 (100ms dwell time). For the calibration of the instrumental response, 1 ml of a 200ppm primary standard solution of glycerol and glycerol carbonate were introduced in 2 mL of methanol.

Acknowledgements

Acknowledgements Text.

Keywords: Geothermal SiO_2 • Microwaves• glycerol carbonate • MCM-41• eco-friendly processes

[1] C.T. Kresge, W.J. Roth, Chem. Soc. Rev. 42 (2013) 3663.

[2] A. Taguchi, F. Schüth, Microporous Mesoporous Mater. 77 (2005) 1–45.

[3] S. Hudson, J. Cooney, E. Magner, Angew. Chemie Int. Ed. 47 (2008) 8582–8594.

[4] S. Wang, Microporous Mesoporous Mater. 117 (2009) 1–9.

[5] W.-S. Chiang, E. Fratini, P. Baglioni, J.-H. Chen, Y. Liu, Langmuir 32 (2016) 8849–8857.

[6] G.A. Tompsett, W.C. Conner, K.S. Yngvesson, ChemPhysChem 7 (2006) 296–319.

[7] Y. Cao, H. Wei, Z. Xia, Trans. Nonferrous Met. Soc. China 19 (2009) s656–s664.

[8] I. Longo, A.S. Ricci, J. Microw. Power Electromagn. Energy 41 (2007) 4–19.

[9] J.J. a. M. van der Mullen, M.J. van de Sande, N. de Vries, B. Broks, E. Iordanova, a. Gamero, J. Torres, a. Sola, Spectrochim. Acta Part B At. Spectrosc. 62 (2007) 1135–1146.

[10] V. Gude, P. Patil, E. Martinez-Guerra, S. Deng, N. Nirmalakhandan, Sustain. Chem. Process. 1 (2013) 5.

[11] Z. Fang, R. L. Smith Jr., X. Qi, Production of Biofuels and Chemicals with Microwave, Springer Dordrecht Heidelberg New York London, 2015.

[12] C. Gérardin, J. Reboul, M. Bonne, B. Lebeau, Chem. Soc. Rev. 42 (2013) 4217.

[13] H. Fukuda, A. Kondo, H. Noda, J. Biosci. Bioeng. 92 (2001) 405–416.

[14] P. Cintas, S. Tagliapietra, E. Calcio Gaudino, G. Palmisano, G. Cravotto, Green Chem. 16 (2014) 1056.

[15] M.O. Sonnati, S. Amigoni, E.P. Taffin de Givenchy, T. Darmanin, O. Choulet, F. Guittard, Green Chem. 15 (2013) 283–306.

[16] J.R. Ochoa-Gómez, O. Gómez-Jiménez-Aberasturi, B. Maestro-Madurga, A. Pesquera-Rodríguez, C. Ramírez-López, L. Lorenzo-Ibarreta, J. Torrecilla-Soria, M.C. Villarán-Velasco, Appl. Catal. A Gen. 366 (2009) 315–324.

[17] S.E. Kondawar, A.S. Potdar, C. V. Rode, RSC Adv. 5 (2015) 16452–16460.

[18] V. Calvino-Casilda, G. Mul, J.F. Fernández, F. Rubio-Marcos, M.A. Bañares, Appl. Catal. A Gen. 409–410 (2011) 106–112.

[19] J. González-Rivera, I.R. Galindo-Esquivel, M. Onor, E. Bramanti, I. Longo, C. Ferrari, Green Chem. 16 (2014) 1417–1425.

[20] J. González-Rivera, J. Tovar-Rodríguez, E. Bramanti, C. Duce, I. Longo, E. Fratini, I.R. Galindo-Esquivel, C. Ferrari, J. Mater. Chem. A 2 (2014) 7020.

[21] T.N. Blanton, M. Rajeswaran, P.W. Stephens, D.R. Whitcomb, S.T. Misture, J. a. Kaduk, Powder Diffr. 26 (2012) 313–320.

[22] C.S. Triantafillidis, A.G. Vlessidis, N.P. Evmiridis, Ind. Eng. Chem. Res. 39 (2000) 307–319.

[23] C.T. Kresge, M.E. Leonowicz, W.J. Roth, J.C. Vartuli, J.S. Beck, Nature 359 (1992) 710–712.

[24] M. Kruk, M. Jaroniec, A. Sayari, J. Phys. Chem. B 101 (1997) 583–589.

[25] J.S. Beck, J.C. Vartuli, W.J. Roth, M.E. Leonowicz, C.T. Kresge, K.D. Schmitt, C.T.W. Chu, D.H. Olson, E.W. Sheppard, J. Am. Chem. Soc. 114 (1992) 10834–10843.

[26] M. Klotz, P.A. Albouy, A. Ayral, C. Ménager, D. Grosso, A. Van Der Lee, V. Cabuil, F. Babonneau, C. Guizard, Chem. Mater. 12 (2000) 1721–1728.

[27] B. Katryniok, S. Paul, V. Bellière-Baca, P. Rey, F. Dumeignil, Green Chem. 12 (2010) 2079.

[28] M. Thommes, K. Kaneko, A. V. Neimark, J.P. Olivier, F. Rodriguez-Reinoso, J. Rouquerol, K.S.W. Sing, Pure Appl. Chem. 87 (2015) 1051–1069.

[29] N.C. Das, H. Cao, H. Kaiser, T. Warren, J.R. Gladden, P.E. Sokol, (2012).

[30] Y. Nakahara, T. Takeuchi, S. Yokoyama, K. Kimura, Surf. Interface Anal. 43 (2011) 809–815.

[31] J. Trébosc, J.W. Wiench, S. Huh, V.S.-Y. Lin, M. Pruski, J. Am. Chem. Soc. 127 (2005) 3057–3068.

[32] E. Joussein, S. Petit, J. Churchman, B. Theng, D. Righi, B. Delvaux, Clay Miner. 40 (2005) 383–426.

Entry for the Table of Contents

FULL PAPER

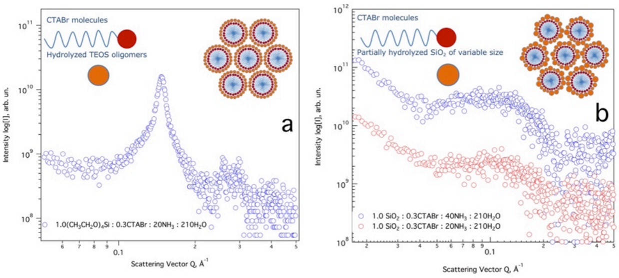

J. Tovar Rodriguez,[a] J. González Rivera,[b] C. Ferrari,[b] I. Longo,[b] M. Onor,[c] P. Baglioni[a] and E. Fratini[a]*

Page No. – Page No.

A green microwave-assisted synthesis of hexagonally ordered silica sieves using a geothermal waste as silicon precursor and their use as Zn catalytic supports for carbonylation of glycerol

Paper III

Surfactant recovery from mesoporous metal modified materials (Sn, Y, Ce, Si MCM-41), by ultrasound assisted ion-exchange extraction and its re-use for a microwave in situ cheap and ecofriendly MCM-41 synthesis

Authors: J. Gonzlez Rivera, J. Tovar-Rodrguez, E. Bramanti, C. Duce, I. Longo, E. Fratini, I. R. Galindo-Esquivel and C. Ferrari

RSC Journal of Materials Chemistry A

Journal of
Materials Chemistry A

PAPER

View Article Online
View Journal | View Issue

Cite this: *J. Mater. Chem. A*, 2014, **2**, 7020

Surfactant recovery from mesoporous metal-modified materials (Sn–, Y–, Ce–, Si–MCM-41), by ultrasound assisted ion-exchange extraction and its re-use for a microwave *in situ* cheap and eco-friendly MCM-41 synthesis

J. González-Rivera,[a] J. Tovar-Rodríguez,[a] E. Bramanti,[b] C. Duce,[c] I. Longo,[d] E. Fratini,[e] I. R. Galindo-Esquivel[a] and C. Ferrari*[d]

Received 7th December 2013
Accepted 24th February 2014

DOI: 10.1039/c3ta15078j

www.rsc.org/MaterialsA

Different metal substituted (Y, Sn and Ce) MCM-41 materials were synthesized and detemplated by a low temperature surfactant removal methodology. All metal substituted materials showed an increase in the d_{100} lattice parameter compared to the parent MCM-41 matrices. The increase depends on both the metal type and amount that is successfully incorporated by direct conventional hydrothermal synthesis. The metal modified MCM-41 materials were detemplated by an ultrasound assisted (US) ion-exchange process using methanol as the solvent (NH_4NO_3/US/MeOH). The effect of the ultrasound amplitude, extraction time and salt concentration were explored, and optimal values were determined for Y–MCM-41 detemplation (40 mM of NH_4NO_3, 60% of US amplitude and 15 min of adiabatic treatment). The removal percentage achieved with these values was in the following order: Y (97.7%) > Ce (94.4%) > Sn (92.1%) > Si (90.3%). Several techniques (SAXS, FTIR, TGA, ^{1}H MAS, ^{29}Si HPDEC MAS NMR and N_2 physisorption) demonstrated that the mesoporous materials keep their hexagonal structure and high surface area after the NH_4NO_3/US/MeOH surfactant extraction. Moreover, the thermal shrinkage of the structure was reduced in the following order: Si (0.6%) < Sn (4%) < Ce (5%) < Y (9%) < calcined samples (from 9 to 15%). The surfactant recovered was successfully recycled in a consecutive microwave assisted hydrothermal synthesis cycle (MW-HT). The synergy of different strategies (MW-HT synthesis, NH_4NO_3/US/MeOH surfactant removal and surfactant recovery) produces considerable time, energy and cost abatement, environmental impact reduction and promising scale up projections in the eco-friendly synthesis of MCM-41 materials.

1 Introduction

Recently, the use of MCM-41 mesoporous materials has been increasing in different applications such as catalysis[1] or heavy metal pollutant adsorbents in environmental applications.[1–3] They show unique properties, like high specific surface area, controllable pore size and well ordered hexagonal structure.[4]

The synthesis of siliceous MCM-41 has been widely studied and different methodologies have been proposed.[2–4] To modulate its surface properties, Si–MCM-41 can be modified with an active phase like metals[5,6] or enzymes[7,8] in post-synthesis treatments. On the other hand, direct insertion of different metals into the siliceous framework is typically done by the addition of the metal precursor in the synthesis gel followed by the hydrothermal crystallization process. Several metals have been tested for this purpose.[9–12]

The MCM-41 structure is built up by the presence of a structure directing agent, typically the surfactant molecule cetyltrimethylammonium bromide (CTAB). After the crystallization process, usually done under mild hydrothermal conditions, the CTAB must be removed from the inorganic structure to generate porosity. Calcination is generally used to remove the surfactant from the mesoporous structure. The process is carried out at high temperature under controlled conditions to avoid thermal shrinkage and structure damage. The conventional calcination process is highly undesirable since it might

---

[a] Chemical Engineering Department, University of Guanajuato, Noria Alta s/n 36050, Guanajuato, Gto, Mexico

[b] National Research Council of Italy (C.N.R.), Istituto di Chimica dei Composti Organo Metallici (ICCOM) – UOS Pisa, Via G. Moruzzi 1, 56124 Pisa, Italy

[c] Department of Chemistry and Industrial Chemistry, University of Pisa, Via Risorgimento 35, 56127 Pisa, Italy

[d] National Research Council of Italy (C.N.R.), Istituto Nazionale di Ottica, (INO) – UOS Pisa, Via G. Moruzzi 1, 56124 Pisa, Italy. E-mail: carlo.ferrari@ino.it; Fax: +39-050-315-2247; Tel: +39-050-315-2245

[e] Department of Chemistry "Ugo Schiff" and CSGI, University of Florence, Via della Lastruccia 3, 50019 Sesto Fiorentino, Florence, Italy

cause not only structural damage but it also presents high energy demands, requires long processing time and produces toxic residual pollution, which results in an increase of the catalyst production cost.

As alternatives to the high temperature calcination process, several methodologies have been developed to remove the surfactant from the MCM-41 structure.[13,14] Two main approaches have been explored: (1) low temperature degradation and (2) removal by solvent extraction. The first approach requires an oxidative system to degrade the surfactant, achieved by dielectric barrier discharge plasma,[15] H_2O_2,[16] microwave[17] and Fe/H_2O_2.[18] Regarding the second approach, the removal of the template has been achieved using acids[16,19] ammonium salts,[19,20] ultrasound[21] or supercritical CO_2 in alcoholic solvents.[22]

While both approaches are performed at low temperature levels, the solvent extraction process seems more appealing since it opens up the possibility to recover and further re-use the surfactant in the synthesis process. This is a very important fact from an economical point of view since about 50% w/w of the total quantity of MCM-41 synthesized corresponds to the surfactant molecule. Thus, the direct cost reduction in raw materials is clearly advantageous compared to the surfactant loss and pollution generation caused by its degradation.

The surfactant removal by extraction using alcohols seems to be the best approach, whereas some drawbacks still have to be solved. The mechanism could be a disruption of the surfactant aggregates caused by the organic solvent contact. Then, the non-aggregated surfactant molecules are released to the solvent and easily elute from the mesopores. However, using solely organic solvents like ethanol does not allow the surfactant to be removed completely and some acids or cation exchangers have to be added to the extraction mixture. HCl in ethanol has been reported by some authors[16,19] and high detemplation was achieved. Nonetheless, the use of acids with alcohols can cause an esterification of the silanol groups in the MCM-41 surface and consequently, undesired changes in the material properties can occur.[19]

Considering the cationic nature of the surfactant CTAB, a solvent extraction using a similar salt cation producing an ion exchange between the dissolvent salt ions and the CTAB molecule anchored onto the O_3SiO^- groups in the MCM-41 structure, is already well established. In particular, the pure silicon MCM-41 matrices were difficult to detemplate completely using NH_4NO_3 in ethanol and 3 cycles of 15 min were necessary.[20] However, it was also shown that an increase in the isomorphic metal (aluminium) substitution resulted in higher surfactant removal, because CTAB molecules attached onto O_3MO^- such as the tetrahedral aluminium atoms $[AlO_4]^-$ are easier to detemplate.

Following the mechanism of surfactant aggregate disruption, recently, Jabariyan and Zanjanchi[21] reported an efficient surfactant removal from the Si–MCM-41 structure using low frequency ultrasound (US) irradiation in ethanol without addition of any salt. This approach still required more than one cycle to completely remove the surfactant from the mesopores.

The US assisted ion exchange methanol extraction of the surfactant from metal modified MCM-41 has not been explored so far. The synergy caused by the US irradiation and the ion-exchange salt is expected to increase the surfactant removal in a single cycle. In such a case, a total removal of CTAB could be easily achieved, causing direct minimization of solvent use, energy consumption and processing time. Furthermore, this approach allows CTAB to be recovered and re-used after simple solvent distillation.

As mentioned above, both the diminution of total stages in the synthesis process of the metal modified MCM-41 and the reduction in pollution and final cost of the materials are desirable. In consequence, to develop an eco-friendly synthesis of metal modified MCM-41 mesoporous structures, direct incorporation of different metals (yttrium, tin and cerium) into the hydrothermal synthesis and a fast low temperature removal of the surfactant from these structures are explored in this work. Furthermore, the possibility of an accelerated synthesis by microwave assistance has been explored, resulting in a considerable reduction of the synthesis time.

The effects of the ultrasound amplitude, extraction time and salt concentration were studied in the low temperature ultrasound assisted ion exchange process (named as NH_4NO_3/US/MeOH surfactant extraction here on) and optimal values were determined for high detemplation. The recycling of the recovered surfactant has been demonstrated. Additionally, different conditions of the surfactant degradation by oxidative systems were compared.

The synergy of using different strategies like microwave assisted hydrothermal synthesis (MW-HT), low temperature NH_4NO_3/US/MeOH surfactant extraction and the recovery/re-use of surfactant and solvent resulted in a considerable time, raw material, energy, cost and environmental impact reduction in the synthesis of metal–MCM-41.

2 Results and discussion

2.1 Characterization of M–MCM-41 synthesized mesoporous materials

Several well ordered metal modified MCM-41 structures were synthesized by the hydrothermal crystallization process. Three different metal substituted (Y, Sn and Ce) materials were prepared. For comparative purposes, the chemical composition obtained by energy dispersed X-ray spectroscopy microanalysis (EDS) of the different materials is shown in Table 1 (see columns Si and M).

Table 1 Composition of as-synthesized metal modified MCM-41 materials by EDS analysis and lattice parameters

Material	Si (w/w)	M (w/w)	Si/M		d_{100}, nm	a_0, nm
			[a]	[b]		
Si–MCM-41	100.0	—	—	—	4.77	5.5
Y–MCM-41	36.68	1.03	225	133	4.79	5.5
Sn–MCM-41	35.1	1.4	125	107	5.08	5.9
Ce–MCM-41	32.10	0.60	50	153	4.85	5.6

[a] Nominal molar ratio Si/M. [b] Calculated by microanalysis results.

The nominal metal concentration for each material was selected considering the disparity between the tetrahedral silicon Si^{4+} and the ionic radius for the isomorphic substituted heteroatom. The ionic radius size decreases in the order: Ce^{4+} (1.01 Å) > Y^{3+} (0.93 Å) > Sn^{4+} (0.71 Å) > Si^{4+} (0.41 Å); thus, the direct incorporation is expected to be difficult. Nevertheless, all the metals were successfully incorporated into the framework and, as expected, the poorest metal substitution occurred when the cerium incorporation was made. As the Ce^{4+} ionic radius is more than twice the size of Si^{4+}, only a third of the nominal metal loading was substituted. The Si/Ce ratio obtained was 153 compared to the nominal value of 50 (Table 1, columns A and B). The highest metal substitution was achieved for the Sn–MCM-41 material.

Fig. 1a shows the Small Angle X-ray Scattering (SAXS) patterns for the synthesized MCM-41 materials. All the materials prepared exhibit four main diffraction peaks that can be indexed to the (100), (110), (200) and (210) planes associated with the hexagonal crystal system,[23] space group *p6mm*. For the parent Si–MCM-41 material (see Fig. 1a), the (*hkl*) values assigned to the first three planes are found around the scattering vector (*q*) values of 0.15, 0.27 and 0.31 A^{-1} respectively. The spacing for the hexagonal lattice (Table 1, column d_{100}) was calculated by interpolation using these reflections. The unit cell a_0 constant (Table 1, column a_0) was calculated using Bragg's Law. Assuming that the nominal metal concentration was effectively incorporated, the d_{100} increase should follow the order: Ce > Y > Sn. However, the d_{100} parameter increases depending on both, the size of the metal and the actual amount of heteroatom substituted. Given that Sn exhibits the highest quantity of metal incorporated successfully, the d_{100} increase was observed as Sn > Ce > Y. Since the chemical bonding Si–O–M is longer than the bonding Si–O–Si, the d_{100} spacing increase is in agreement with an incorporation of the metal into the framework. As the metal load increases, the diffraction peaks tend to shift to lower *q* values, which represent an increase in the unit cell parameters. A lower structural change is produced when Y is introduced into the structure. For this material, the small diffraction peak at 0.24 A^{-1} is consistent with the presence of a lamellar structure given by the surfactant. The most considerable effect is evident when Sn is incorporated into the MCM-41 structure, with a (100) diffraction peak displacement to $q = 0.14\ A^{-1}$, indicative of a d_{100} value of 5.08 nm. Similar results have been reported for several metal modified MCM-41.[10,19] Regardless of the metal substituted, the hexagonal structure is well preserved for all materials.

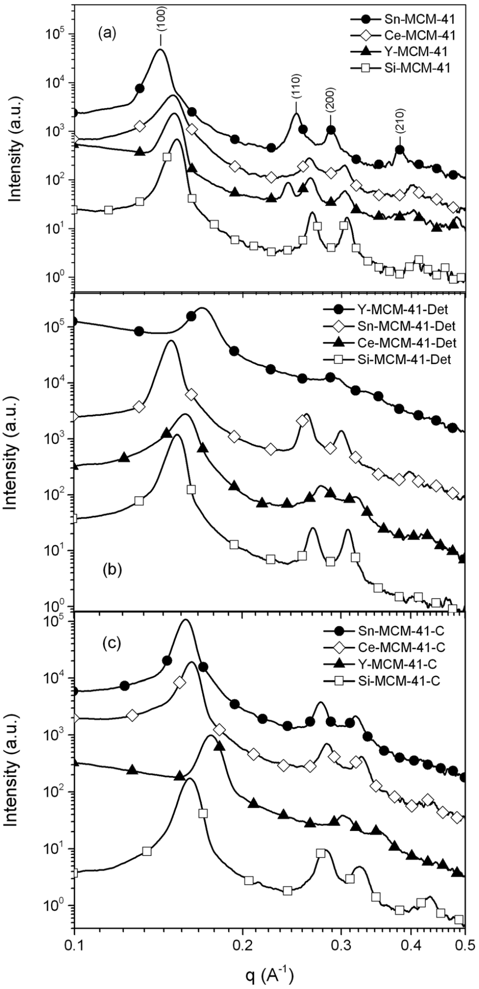

Fig. 1 SAXS patterns: (a) materials containing the templating agent (as synthesized); (b) materials after NH_4NO_3/US/MeOH surfactant extraction under optimal conditions; (c) calcined samples.

2.2 Ultrasound assisted-NH_4NO_3/methanol ion exchange extraction surfactant removal

A low temperature methodology for surfactant removal from the metal modified mesoporous MCM-41 synthesized structures was investigated. This methodology considered the use of ultrasound irradiation coupled with a low concentration ammonium salt solution in methanol.

While ethanol is the most widely used solvent for extraction, methanol has considerable advantages such as a lower boiling point (10 °C below that of ethanol) which allows a considerable energy saving in the solvent recovery process. Moreover, the solubility of CTAB in methanol is higher than the solubility when ethanol is used as the solvent (greater than 0.75 M against 0.5 M in ethanol). The use of ultrasound further increases the solubility of CTAB, since the energy transferred to the solution increases the temperature. At 40 °C the solubility of CTAB in methanol increases beyond 1 M.

Many other monovalent salts can be used as ion exchange agents. Different characteristic must be considered to increase surfactant removal efficiency while the structural surface properties remain unchanged. The ion exchange process can be described as a reversible chemical reaction wherein a ionic specie in solution (NH_4^+ for our system) is exchanged by a similarly charged ion ($(C_{16}H_{33})N^+(CH_3)_3$) attached to a fixed molecule in MCM-41 particles (O_3SiO^- or O_3MO^- groups). Thus, different and smaller counterions could cause different results due to ion exchange efficiency. In principle, the smallest counterion (such as Na^+) could be more effective due to an easier access to the exchange sites. However, in our particular case, the use of ultrasound greatly increases the dynamics of the exchange process, so that the counterion size should not be a critical parameter.

Furthermore, samples that had been extracted with alkali metal salts (EtOH/$NaNO_3$) presented: (i) lower surface area; (ii) lower mesopore volume than samples that had been extracted with either pure solvents or with acid-containing solutions, (iii) are very unstable toward the following calcination step, and (iv) show no catalytic activity (in Friedel–Crafts acylation of 2-methoxynaphthalene) demonstrating that active sites of the catalyst might be modified by the presence of sodium ions.[19,20]

The use of ammonium nitrate is the most logical choice, given that the calcined materials are usually ion exchanged in NH_4NO_3 solution to remove the residual sodium ions, and Brønsted acidity is created by heating the ammonium form.[19] Even more, the use of ammonium nitrate causes a weak interaction of the ammonium ions with the different groups on the surface on the MCM-41,[20] resulting in easy condensation to produce the silanol or the active sites. This characteristic is very desirable for the final application of the synthesized materials.

The effect of three different factors (salt concentration, ultrasound amplitude and time) on a solvent extraction approach was investigated. The evaluation of the detemplation degree was done using FT-IR and TGA.

It seems that the disruption of micelles and the CTAB release to the methanol was fast, due to the synergy caused by the ultrasound energy and the high ion exchange efficiency of NH_4NO_3 in methanol. Thus, only one cycle of treatment is enough to achieve high percentages of removal. Table 2 shows the results of the Y–MCM-41 detemplation for all the Box–Behnken experimental design runs. High detemplation values were achieved (99.3%, run 11, Table 2) after only one cycle of treatment. According to the analysis of variance (ANOVA), the salt concentration (x_1) showed the main effect on the NH_4NO_3/US/MeOH surfactant extraction. The low concentration caused low removal whereas high concentration showed a negative effect, indicating that an optimal value should exist in the explored range.

Table 2 Full experimental values of the Box–Behnken design

Run	x_1	x_2	x_3	Total area[a]	% Removal[b]
1	−1	−1	0	11.9	69.2
2	0	+1	−1	1.2	96.9
3	+1	−1	0	1.9	95.1
4	+1	0	−1	2.3	94.1
5	0	0	0	2.1	94.5
6	−1	+1	0	14.3	63.1
7	0	−1	+1	1.7	95.7
8	−1	0	−1	14.5	62.4
9	0	−1	−1	2.0	94.9
10	+1	+1	0	0.9	97.8
11	+1	0	+1	0.3	99.3
12	0	0	0	1.9	95.1
13	0	0	0	2.0	94.9
14	0	+1	+1	0.5	98.8
15	−1	0	+1	12.0	68.9

[a] Calculated form of the integrated area of FTIR spectra. [b] Calculated using the as-synthesized Y–MCM-41 FTIR area as 100%.

The time (x_3) and the ultrasound amplitude (x_2) did not show considerable effect by themselves. However, the interaction between the US and NH_4NO_3 concentration contributed with positive effects. From the Box–Behnken surface response analysis, the optimal levels to maximize the surfactant removal were identified as: $x_1 = 0.6$, $x_2 = 1$, $x_3 = 1$. According to Table 6, the decoded values are: 40 mM of NH_4NO_3, 60% of US amplitude and 15 min of adiabatic treatment (the maximum temperature observed was below 50 °C and it depends on the different combination of the factors and its levels). These conditions were applied to the Sn–MCM-41, Ce–MCM-41 and Si–MCM-41 materials. The removal percentage achieved after the NH_4NO_3/US/MeOH surfactant extraction was in the order: Y > Ce > Sn > Si, with the corresponding values of 97.7, 94.4, 92.1 and 90.3%.

Lang and Tuel[20] proposed a surfactant removing approach from aluminium modified and pure silica based MCM-41, using 250 mM of NH_4NO_3 at 60 °C in ethanol. They proposed that the surfactant removal percentage depends on the metal concentration, being greater for higher metal concentrations. In this work, the salt concentration was reduced to 40 mM (around 6 times less compared to the literature[20]) for high silica/Y molar ratio samples and full detemplation was achieved. This reduction can be due to the synergy between the cavitation effect produced by the ultrasound irradiation and the salt concentration. The sudden formation of cavities in the solvent might be contributing to the facilitation of the transport of the NH_4NO_3 inside the MCM-41 channels, accelerating the ion-exchange process. Similarly, the use of ultrasound to detemplate MCM-41 was recently reported by Jabariyan and Zanjanchi.[21] They achieved a 93% of detemplation from Si–MCM-41 when it was treated for 15 min using ethanol or methanol as the solvent and ultrasound. To fully remove the surfactant, they used more cycles under sonication. Their reported methodology was focused solely on pure siliceous MCM-41 and the metal modified materials were not explored.

2.3 Characterisation of M–MCM-41 NH_4NO_3/US/methanol extracted mesoporous materials

Fig. 2 shows the FTIR spectra for the materials containing the surfactant, after the low temperature removal and the calcined samples. Several bands are associated with the presence of the surfactant into the MCM-41 samples: (i) the bands at 2924 and 2850 cm^{-1} correspond to the bending vibration (–C–H) of the $-CH_2-$ and $-CH_3$ groups in the C_{16} aliphatic chain of the CTAB molecule, respectively; (ii) the –C–H stretching vibration and alkylammonium vibration are assigned in the region of 1490 to 1380 cm^{-1}; (iii) a weak signal at 725 cm^{-1} is also assigned to the symmetrical vibration in the plane (rocking). For all the

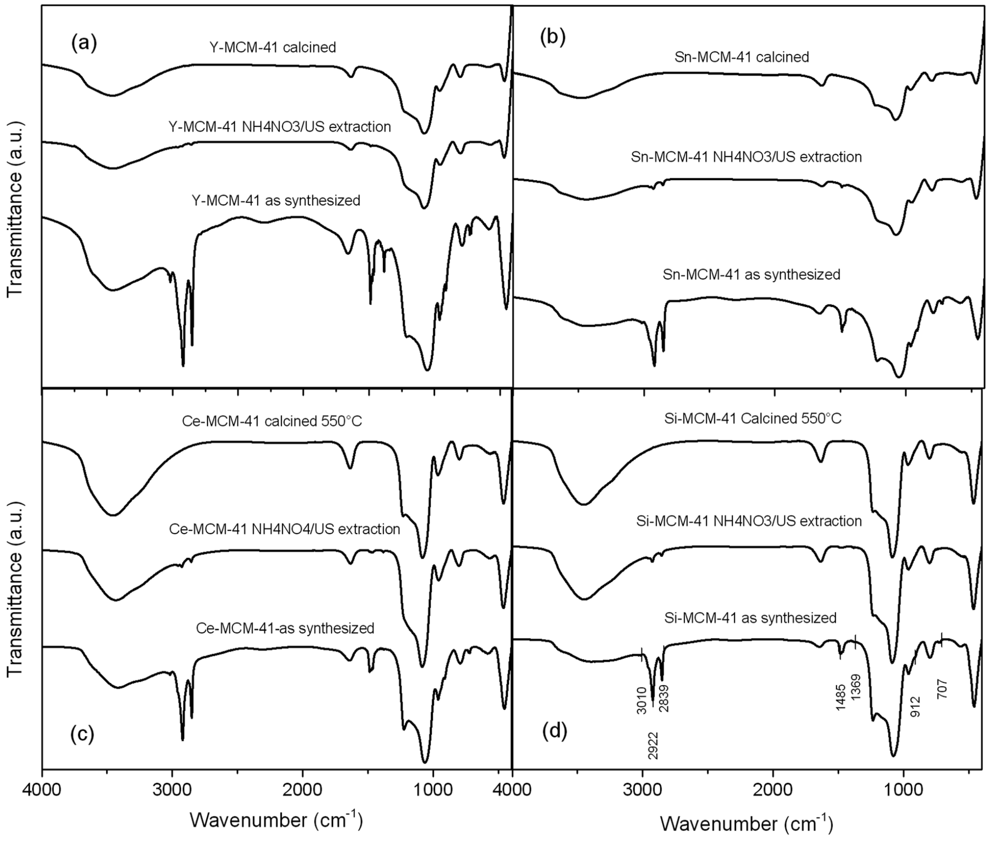

Fig. 2 FTIR spectra for: (a) Y–MCM-41; (b) Sn–MCM-41; (c) Ce–MCM-41 and (d) Si–MCM-41 after calcination, NH_4NO_3/US/MeOH extraction and as synthesized materials.

calcined samples, these bands are not present. After the NH_4NO_3/US/MeOH surfactant extraction, the peaks assigned to the hexadecyltrymethylammonium molecule are minimized or completely reduced.

The peak signals at around 1090, 970, and 465 cm^{-1} are assigned to the stretching and bending vibrations of silica–oxygen tetrahedra. The NH_4NO_3/US/MeOH surfactant extraction produces no changes in these bands and after the treatment, these peaks remain unmodified. It is important to note that no signals were identified in the region from 1400 to 1450 cm^{-1} typically for NH_4^+ ions. This result suggests a weak interaction between this group and the modified metal or silanol groups (Si–OH) which tend to be reactive.

The FTIR and the SAXS analyses (Fig. 1 and 2) demonstrate that the mesoporous materials keep their hexagonal structure without considerable changes after the NH_4NO_3/US/MeOH surfactant extraction. In the particular case of pure Si- and Sn-modified structures, the scattering patterns remain identical to the as-synthesized materials. Y– and Ce–MCM-41 samples show small reduction in the intensity of SAXS peaks. Both structures showed the greater response to the surfactant removal treatment and achieved the highest percentage of removal. These results suggest that the modified metal has additional effects on the surfactant removal beyond the factors explored in the Box–Behnken analysis. Further optimization for each individual material should be done, to obtain the maximum surfactant removal.

Confirmatory experiments of the surfactant removal were carried out using thermo-gravimetric analysis. The temperature region of the surfactant removal was explored using FTIR spectroscopy coupled to TG analysis. The experiments were performed under an air atmosphere to emulate the calcination process. In the case of Y–MCM-41 and Sn–MCM-41, different mass loss regions were identified (see Fig. 3): the first event was at temperatures below 120 °C corresponding to the physisorbed water into the mesopores. Then from 120 to 270 °C the CTAB was successfully removed. From 270 to 350 °C the TMAOH molecule was burned. The drop in mass after 350 °C was due to the water release produced by the silanol condensation and also the oxidation of the residual carbonaceous material after an

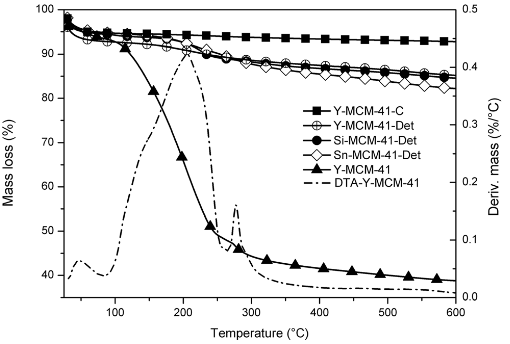

Fig. 3 TG analysis for calcined and as synthesized (Y–MCM-41), and extracted samples (Y, Si, Sn–MCM-41).

incomplete surfactant and/or co-surfactant combustion. In the case of Ce–MCM-41 and Si–MCM-41 a similar trend was observed, however the synthesis of these two materials did not involve the use of a co-surfactant molecule (TMAOH). The mass loss of surfactant in all cases was estimated in the temperature range of 120 to 350 °C. The results were in agreement with the FTIR quantitative analysis.

Table 3 summarizes the textural properties for the calcined and extracted materials. The pore diameter of the MCM-41 is typically in the range of 2 to 10 nm.[23] After the surfactant treatment (either calcination or NH_4NO_3/US/MeOH surfactant extraction), these materials exhibited a narrow pore size distribution from 2 to 4 nm (see Table 3, column D). The materials subjected to high temperature surfactant removal showed large pore diameters. The modified metal caused an expected effect on the pore size: when cerium was introduced into the silica framework, a higher pore modification was produced, compared to the parent material composed of pure silica. In contrast, yttrium produced a lower pore size change, for both surfactant removal treatments (calcined and NH_4NO_3/US/MeOH surfactant extraction). A bimodal pore size distribution was shown by Y–MCM-41 (pore size of 2.2 and 3.2 nm) and Ce–MCM-41 (pore size of 2.4 and 4.0 nm). This bimodal pore size distribution can be attributed to the difference in ionic sizes of the modified metals. If the metal incorporation into the MCM-41 structure is inhomogeneous, the periodicity changes and results in pores with an increased size. This can be applied to Ce– and Y–MCM-41. However, Sn–MCM-41 showed only one pore size distribution suggesting high periodicity and homogeneous metal incorporation.

The specific surface area was high in all cases (see Table 3, column S_{BET}). Ce–MCM-41 detemplated using NH_4NO_3/US/MeOH surfactant extraction shows a higher surface area than the calcined sample even though 5% of the surfactant still remains in the framework. On the other hand, the Y–MCM-41 calcined sample exhibits a higher surface area than the fully surfactant removed sample by NH_4NO_3/US/MeOH surfactant extraction. In the case of Sn– and Si–MCM-41 materials, the specific surface area was higher for the calcined materials than for the extracted samples. For those materials, the remaining surfactant in the structures was about 8 and 10% respectively. The latest values can explain the difference in the value of S_{BET} in the case of Sn– and Si–MCM-4. It is possible to affirm that not only the surfactant removal contributes to the increase in the surface area value S_{BET}, but also the presence of the substituted metal in the framework had a significant effect, when compared with Si–MCM-41.

The structural parameters for the calcined and NH_4NO_3/US/MeOH surfactant extraction detemplated materials are also shown in Table 3. The cell unit value of all samples changes after both surfactant removal approaches (Table 3, column a_0). High temperature calcination can cause a framework contraction due to the dehydroxylation and siloxane bond formation known as thermal shrinkage.[24] The thermal shrinkage can be referred to as $TS = 1 - a_{02}/a_{01}$ where a_{02} and a_{01} are the cell unit values of the detemplated and as-synthesized materials, respectively. For the calcination process, the TS calculated values ranged from 9 to 15%. The highest framework contraction was shown by Ce–MCM-41 and Si–MCM-41 and it was estimated to be 14%. Sn–MCM-41 showed 9% and 13% for the Y–MCM-41 material. The remaining surfactant in the frameworks did not affect the TS value, as mentioned elsewhere.[25]

On the other hand, after the low temperature NH_4NO_3/US/MeOH surfactant extraction proposed, the TS can be minimized to 0.6% in the case of Si–MCM-41. The metal modified structures showed lower TS values in the order of Y > Ce > Sn with 9, 5 and 4%, respectively. In all cases, the values are smaller than the TS caused by calcination. In the case of the NH_4NO_3/US/MeOH surfactant extraction, the metal modified structures can experiment a unit cell reduction produced by the ion exchange mechanism, where the NH_4^+ interacts with the metal substituted (see Table 3, column a_0). The highest unit cell contraction was shown by Y–MCM-41. In this framework, after yttrium was incorporated into the silica network, it could be

Table 3 Structural (SAXS) and textural parameters of mesoporous materials (values between parentheses refer to extracted materials)

Material	$S_{BET}{}^a$ ($m^2 g^{-1}$)	V^b ($cm^3 g^{-1}$)	D^c (nm)	d^d (nm)	$a_0{}^e$ (Å)	W^f (Å)
Y–MCM-41	1077(925)	0.94(0.70)	2.94(2.38)	4.2(4.3)	48(50)	19(26)
Ce–MCM-41	806(870)	0.77(0.64)	3.83(2.77)	4.2(4.6)	48(53)	10(25)
Sn–MCM-41	1129(955)	1.03(0.88)	3.63(2.43)	4.6(4.9)	53(56)	17(32)
Si–MCM-41	1044(1023)	0.94(0.82)	3.56(2.75)	4.1(4.7)	48(55)	12(27)

[a] BET specific surface area. [b] BJH pore volume. [c] BJH average pore diameter. [d] d interplanar spacing of the four reflections derived from the q-vector value. [e] Hexagonal unit cell. [f] Wall thickness as $a_0 - D$.

stabilized by NH_4^+ ions. However, from the spectroscopic characterization there is no evidence of ammonium groups linked to the framework, due to the absence of significant signals in the 1400 to 1450 cm^{-1} interval. This could indicate a structural rearrangement once the surfactant molecule is removed.

SEM micrographs for the metal modified extracted samples are shown in Fig. 4. Ce–MCM-41 shows the smaller particle size (around 0.5 μm) with predominant round ball shape morphology (see Fig. 4a). In the case of Sn–MCM-41 (Fig. 4b), a wide particle size distribution was observed (from 1 to 10 μm) with an irregular shape in the biggest particles to round ball shape morphology showed by the smallest particles. Y–MCM-41 shows worm-like to round ball shapes with a wide particle size distribution (see Fig. 4c). The aggregation patterns depend on the different metal modified synthesized MCM-41 materials. Sn–MCM-41 showed less aggregation and well defined particles when compared with Ce– and Y–MCM-41.

2.4 Effect of the metal concentration on the ion exchange extraction

In order to study the effect of the same metal concentration on the low temperature surfactant removal and possible structural changes, two new metal modified MCM-41 materials were synthesized: Sn– and Ce–MCM-41 were prepared with the same Si/Y ratio (Si/M = 225). For these materials, the removal percentage achieved after the NH_4NO_3/US/MeOH surfactant extraction was in the order: Y > Sn > Ce > Si, with the corresponding values of 97.7, 95.9, 93.6 and 90.3%. These results show that at the same metal concentration, Y–MCM-41 still showed the highest surfactant removal whereas the surfactant percent removal changed considerably for Sn–MCM-41 (from 92.1 to 95.9%) when the tin concentration was reduced 2 : 1. In the case of Ce–MCM-41 no significant effect was found (less than 1% of variation) when the Si/Ce ratio was changed from 50 to 225. It seems that the metal concentration (at least at the same nominal concentration) has an effect on the low temperature surfactant removal and it depends on the nature of the metal used to modify the Si–MCM-41 structure.

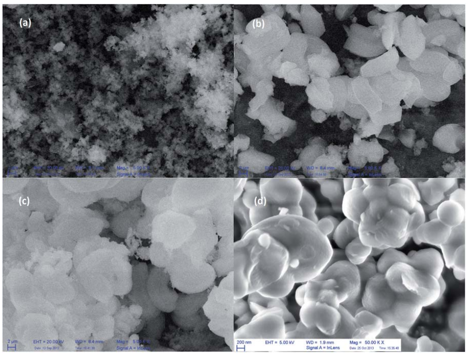

Fig. 4 SEM micrographs for: (a) Ce–MCM-41 (bar = 4 μm, magnification 5k×); (b) Sn–MCM-41 (bar = 4 μm, magnification 5k×); (c) Y–MCM-41 (bar = 4 μm, magnification 5k×) after the NH_4NO_3/US/MeOH surfactant extraction treatment and (d) silica MCM-41 (bar = 400 nm, magnification 50k×) synthesized from surfactant recovered and re-used.

2.5 Solid state NMR characterization of the M–MCM-41 (Si/M = 225) mesoporous materials

Solid state nuclear magnetic resonance studies using magic-angle spinning (MAS NMR) have proven an important role in the structural characterization of some important solids such as the inorganic mesoporous MCM-41 materials[26] and the microporous zeolites.[27] A multinuclear analysis approach can lead to complementing the structural characterization since ^{29}Si MAS NMR provides accurate information regarding the environment of silicon atoms both in the structural framework and those present on the surface. Ultrafast ^{1}H MAS NMR gives valuable information about the surface groups and the water molecules bonded to the silanol groups through hydrogen bonds. Even more, indirect information can be obtained about the influence and the environment of the different metal isomorphically substituted into the hexagonal structure. Other heteronucleus analysis such as ^{119}Sn MAS NMR and ^{89}Y MAS NMR can help to determine the metal coordination state and structural interaction in the analyzed solids. However, some technical limitations involve low sensitivity and low concentration of the metal into the solid materials. In these cases the physical determination by MAS NMR is sometimes not feasible.

The high power decoupling ^{29}Si MAS NMR spectra of the M–MCM-41 materials (Si/M = 225) after the low temperature surfactant removal and the calcined samples are compared with the as synthesized materials in Fig. 5.

All calcined samples exhibit a broad band from −90 to −120 ppm with no distinctive peaks. The spectra for detemplated and as-synthesized materials show two distinctive peaks assigned to Q^3 and Q^4 environments at around −102 and −111 ppm values of chemical shift, which confirms that the proposed ion-exchange extraction methodology results in materials with a similar Q^n distribution compared to the as-synthesized materials.

In order to obtain the single Q^4, Q^3 and Q^2 values assigned to siloxane groups ($Si(O–Si)_4$), isolated silanol groups ($(–O–)_3–Si–OH$), and germinal silanol groups ($(–O–)_2–Si–(OH)_2$), the deconvolution of the spectra obtained between −80 and −120 ppm was performed. Table 4 presents the Q^n values after spectra deconvolution for calcined, NH_4NO_3/US/MeOH extracted and as-synthesized metal modified MCM-41 materials, considering a Gaussian–Lorentzian ratio equal to 0.7 selected to better adjust the typical NMR signal. To compare the relative amount of silanol and siloxane in the samples, the isolated silanol/siloxane (Q^3/Q^4) and total silanol/siloxane ($(Q^2 + Q^3)/Q^4$) ratios were calculated (Table 4, entries 5 and 6).

For the as-synthesized materials containing the same nominal amount of metal substituted, a change in the silicon coordination given by different distributions of Q^n groups is clearly observed. The type and coordination of the heteroatom incorporated produces a unique modification into the silicon environment, when compared to the pure siliceous MCM-41.

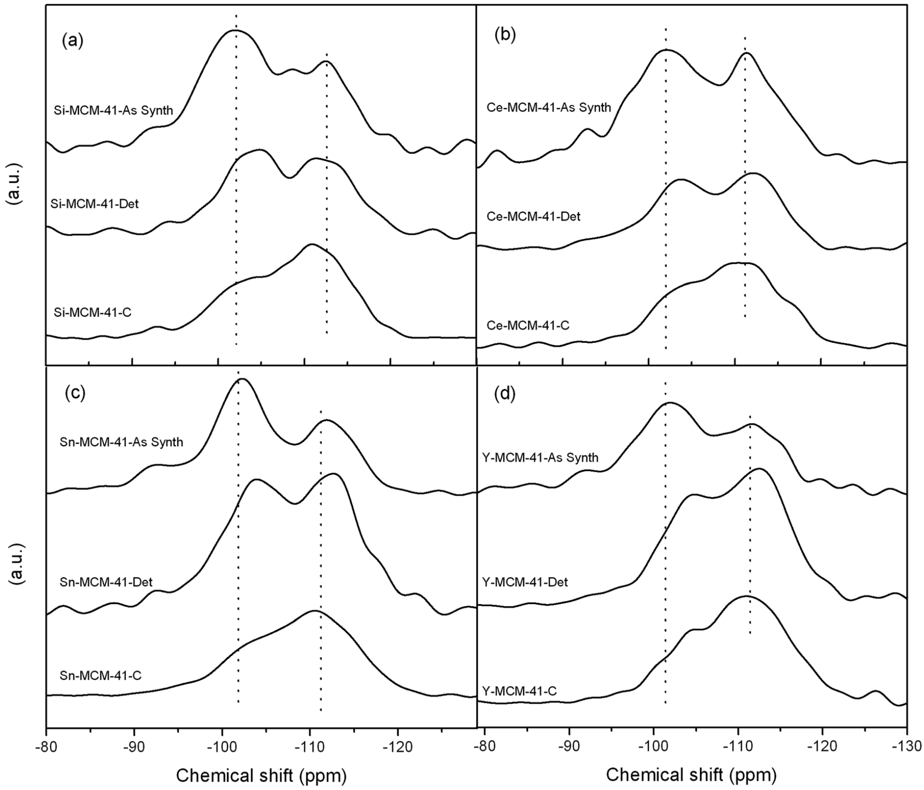

Fig. 5 ^{29}Si HPDEC MAS NMR spectra of the metal modified mesoporous materials: (a) Si–MCM-41, (b) Ce–MCM-41, (c) Sn–MCM-41 and (d) Y–MCM-41.

Table 4 Q^n distribution for calcined, detemplated and as-synthesized metal modified MCM-41 materials

Sample		Q^4	Q^3	Q^2	Q^3/Q^4	$(Q^2 + Q^3)/Q^4$
Si–MCM-41	Calc.	50.37	38.41	9.65	0.76	0.95
	Det.	46.26	45.89	7.84	0.99	1.16
	As syn.	25.87	54.15	19.37	2.09	2.84
Sn–MCM-41	Calc.	55.79	40.95	3.25	0.73	0.79
	Det.	47.66	39.95	12.39	0.84	1.10
	As syn.	30.55	42.24	25.53	1.38	2.22
Y–MCM-41	Calc.	48.9	45.71	5.04	0.93	1.04
	Det.	50.74	40.72	8.08	0.80	0.96
	As syn.	28.04	67.03	4.93	2.39	2.57
Ce–MCM-41	Calc.	64.3	32.32	3.38	0.50	0.55
	Det.	48.1	47.24	4.66	0.98	1.08
	As syn.	36.51	27.72	34.56	0.76	1.71

The calcination treatment to remove the surfactant molecules produces the highest loss of silanolic sites. At least half of the total silanol groups in the original material are condensed with the high temperature treatment to form siloxane bridges or totally eliminated to form water molecules. The surface siloxane bonds formed are hydrophobic and do not produce surface rehydration or water adsorption to favour the reverse process to regenerate the Si–OH sites.[28]

The NH_4NO_3/US/MeOH extraction approach produces silanolic sites loss to a lesser extent. For the Y–MCM-41, the silanol loss has a similar magnitude compared to the calcination procedure. For the rest of the materials, a lower silanol condensation allows the material to keep more active sites than their calcined counterparts. The two distinctive bands for Q^4 and Q^3 are kept (see Fig. 5) and tend to be displaced to lower values of chemical shift, depending on the metal substituted, which proves to have a significant effect on the Q^n distribution as well as the surfactant removal treatment. While the calcination treatment causes surface dehydroxylation, the proposed methodology to remove the surfactant allows the materials to keep a significant amount of the original silanolic sites and may result in the design of specific materials with the desired hydrophobic or hydrophilic properties, since the surface characteristics could be tailored.

High-speed ^{1}H MAS (50 kHz) lead to a sensitive and simple approach for acquiring the high-resolution NMR spectra in MCM-41 samples. According to Trébosc *et al.*[29] the CTAB molecule inside the mesopores of Si–MCM-41 shows three well-resolved peaks at 0.8, 1.2, and 3.1 ppm assigned to the $-CH_3$, $-CH_2-$, and $-CH_2-N(CH_3)_3$ protons in the surfactant molecules inside the mesopores. In the ^{1}H MAS NMR spectra, the surface groups of Si–MCM-41 (free isolated silanols, –Si–OH, Q^3-like environments detected by ^{29}Si HPDEC MAS NMR) are typically assigned to the chemical shift value of 1.8 ppm for dried and degasified materials. The presence of physisorbed water into the mesopores is well detected by the ^{1}H chemical shift of water molecules in hydrated samples of MCM-41. Grünberg *et al.*[30] mentioned three main water environmental sites for the siliceous MCM-41. When the water content in the mesoporous material is about 3 to 6%, the molecules tend to interact due to their high polarity by hydrogen-bonding with the hydration sites (–SiOH) on the solid surface ($-Si_{surface}-OH + H_2O \Rightarrow -Si_{surface}-OH{:}OH_2$) and this signal can be detected about 2.5 ppm. Hydrogen bonded clusters of water molecules may begin to form water molecule bonds (at a concentration bigger than 23%) to the previously adsorbed water ($Si_{surface}-OH{:}OH_2 + H_2O \Rightarrow Si_{surface}-OH_2(OH_2)$) with a chemical shift around 4.7 ppm. Other weak signals for the free water molecules without any surface interaction (mobile clusters) can appear in the whole range from 1 to 6 ppm.

The ^{1}H MAS NMR spectra for the as-synthesized Ce–MCM-41 (Si/Ce = 225) containing the surfactant (CTAB), after the ion exchange extraction and the calcined sample are shown in Fig. 6a. For all the metal modified MCM-41 as synthesized materials, three main chemical shifts around 4.5, 2.6 and 2.2 ppm can be identified. In the analyzed samples of this work, the chemical shifts at 2.2 and 2.6 ppm could be assigned to the CTAB molecule inside the pores of the as-synthesized materials and the residual surfactant molecule for the incomplete detemplated M–MCM-41 materials since these chemical shifts decrease after the two treatments. Even more, the intensity reduction value is more evident for the calcined samples. However, since the analyzed samples did not receive previous treatment such as degasification or thermal heating to remove the physisorbed water, the chemical shift around 2.5 ppm can also be related to the water molecules bonded to the hydrated surface ($-Si_{surface}-OH{:}OH_2$), especially in the case of the calcined and the NH_4NO_3/US/MeOH extracted samples. The chemical shift around 4.5 ppm exhibited by the as-synthesized materials can be assigned to the hydrogen bonded clusters of water molecules mentioned above. This chemical shift showed a displacement to lower ppm after the two treatments for the surfactant removal. In the case of the low temperature surfactant removal, it seems that the water–silanol configurations and associated proton chemical shifts are more complex than only a single hydrogen bonding mentioned before since at least three different peaks are apparently visible. However, a detailed investigation on these possible interactions is beyond the scope of this work. In the case of the calcined samples, a wide signal distributed from 3 to 5 ppm is related to the water–silanol and the mobile clusters mentioned elsewhere.[31]

Fig. 6b shows an enlarged area of the ^{1}H MAS NMR spectra in the interval from 8 to 5 ppm. The spectra show a chemical shift at around 6.3 ppm which corresponds to the NH_4NO_3/US extracted samples. These chemical shifts were detected due to the bonding of ammonium ions after the ion exchange treatment and were not present for the as-synthesized and calcined samples. As is shown in Fig. 6b, the peaks show a displacement from 6.3 to 6.1 ppm in the following order: Y > Sn > Ce. These chemical shifts displacement depend on the nature of the metal and it could be indirect evidence of the isomorphic substitution of the metal into hexagonal siliceous MCM-41 framework. These ^{1}H MAS NMR results seem to indicate that the Y and Sn incorporation appear to generate more acidic sites than the rest of the materials, which is generally true when different coordination and electronegativity heteroatoms are substituted into the oxide structure.

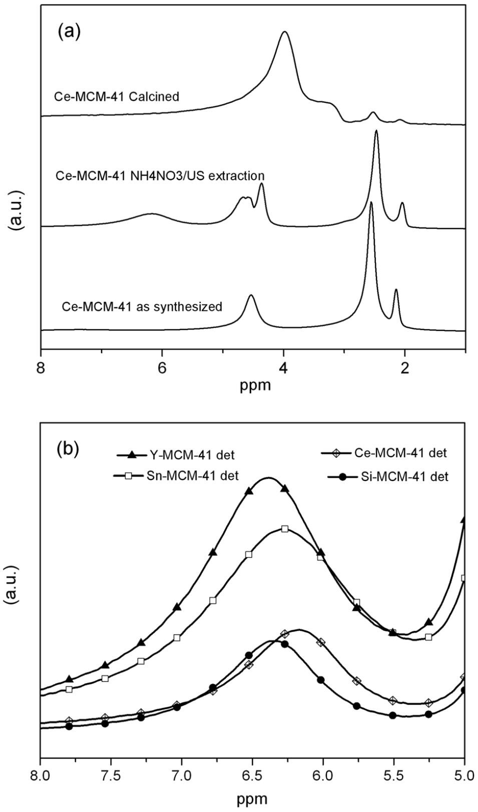

Fig. 6 Ultrafast ^{1}H MAS NMR spectra of: (a) the modified Ce–MCM-41 mesoporous material and (b) M–MCM-41 surfactant removal by NH_4NO_3/US/MeOH extraction.

2.6 Comparative study on Sn–MCM-41 detemplation by oxidative systems and NH_4NO_3/US/MeOH surfactant extraction

To compare the low temperature NH_4NO_3/US/MeOH surfactant extraction proposed in this work, several other surfactant degradation approaches using oxidative systems were applied

Table 5 Surfactant removal efficiency by oxidative and solvent extraction applied to Sn–MCM-41

System	Time (min)	Temperature (°C)	% Removal
UV-MW	60	95	33.6
H_2O_2/UV-MW	60	95	25.7
Fe^{3+}/H_2O_2/UV-MV	60	95	30.8
US/NH_4NO_3/MeOH	15	50	92.1
Calcined	900	550	100

to the metal modified Sn–MCM-41 synthesized mesoporous structure. The FTIR spectra for the different approaches listed in Table 5 are shown in Fig. 7. The efficiency of each surfactant degradation method is reported in Table 5.

The effectiveness in the surfactant degradation using a photochemical reactor and different combinations of the oxidative agents was low in all cases. Several reports indicate that the use of high contact time and oxidative agent concentration is effective to achieve high detemplation under mild conditions.[18] In this work, 60 min and low concentration of oxidative agents were explored. Moreover, the combination of different oxidative agents and the simultaneous irradiation of microwaves and UV energy did not improve the efficiency of degradation in the contact time selected. The main drawback of all these treatments was the loss of the surfactant molecule.

Further investigation on these methodologies was not carried out since one of the aims of this work is to avoid surfactant degradation. The recovery and recycling of the surfactant in the synthesis of MCM-41 materials is discussed in the following section.

2.7 Recovery and re-use of CTAB: a fast and convenient Si–MCM-41 synthesis approach

Considering the reduction of time and energy demands, an innovative and eco-friendly synthesis process for the MCM-41 mesoporous materials was investigated as well. First, Si–MCM-41 was synthesized in a hydrothermal microwave assisted process. The hydrothermal time was reduced from 24 to 2 h using a coaxial applicator to introduce the microwave energy into the hydrothermal reactor. Since the hydrothermal crystallization time was significantly reduced, direct energy saving was also involved.

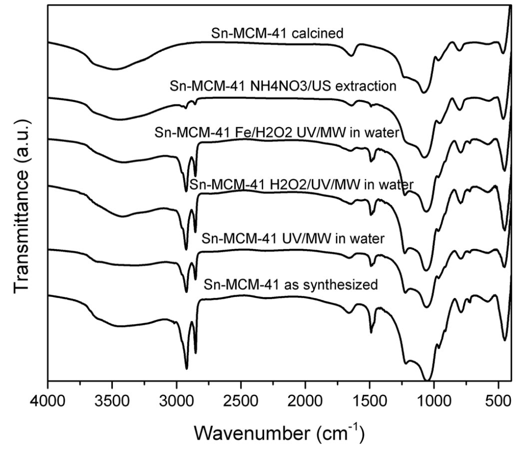

Fig. 7 FTIR spectra for Sn–MCM-41 after different treatments applied to remove the surfactant through oxidative removal.

After the microwave hydrothermal synthesis, this material was submitted to the NH_4NO_3/US/MeOH surfactant extraction explored in Section 2.2.

Finally, the CTAB was recovered and it was used to synthesize a new batch of Si–MCM-41 without the use of fresh surfactant. The FTIR spectra in Fig. 8a shows that the quality of the surfactant recovered after the detemplation step is kept, indicating that the NH_4NO_3/US/MeOH surfactant extraction does not induce significant surfactant degradation. The MCM-41 obtained from the recovered surfactant also exhibits high

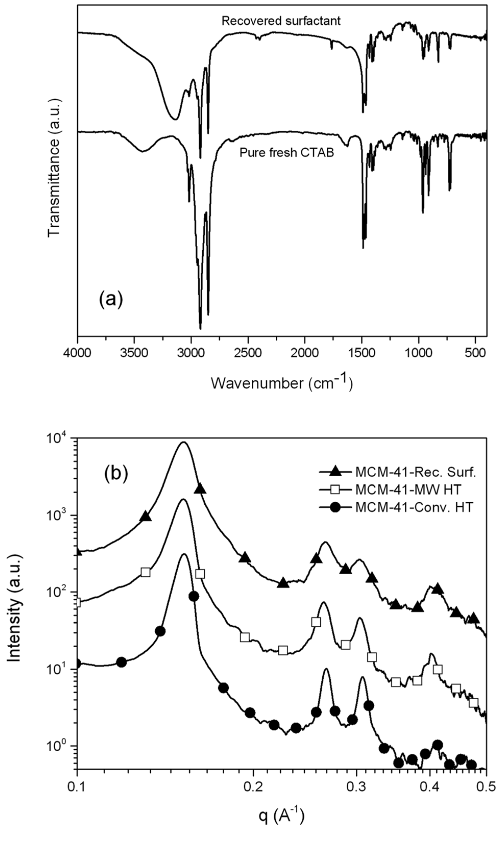

Fig. 8 (a) FTIR spectra for the CTAB recovered (dried) compared to the CTAB reagent and (b) SAXS for MCM-41-Rec.Surf. synthesized with the recovered surfactant, Si–MCM-41-MW HT obtained by microwave assisted hydrothermal synthesis and MCM-41-Conv.HT synthesized by conventional hydrothermal synthesis.

crystallinity and a hexagonal structure (see Fig. 8b). The SAXS patterns for the MCM-41 synthesized by conventional hydrothermal synthesis and microwave assisted hydrothermal synthesis (MW-HT) reveal that both materials have a hexagonal crystalline structure, exhibiting the four main diffraction peaks.

Thus, the microwave assisted hydrothermal synthesis proves to be effective and time saving. High aggregation patterns with the typical worm-like morphology and particle size (around 0.5 μm) is shown in Fig. 4d. The reuse of CTAB implies a saving of about 50% in raw material costs. Moreover, the distilled methanol can also be reused in a new extraction step. The CTAB/methanol separation process does not require too much energy in comparison with the energy needed to achieve high temperature surfactant removal by calcination.

3 Experimental

3.1 Materials

The following reagents were purchased from Sigma-Aldrich and used without further purification: colloidal silica Ludox AS-40 (SiO_2, 40 wt% suspension in water) and tetraethyl orthosilicate ($Si(OC_2H_5)_4$, TEOS, 99.0% GC) were used as silicon sources. Tetramethylammonium hydroxide ($N(CH_3)_4{}^+OH^-$, TMAOH 1 M in water) was used as the co-surfactant in the synthesis of Sn–MCM-41 and Y–MCM-41. The template molecule was hexadecyltrimethylammonium bromide ($(C_{16}H_{33})N(CH_3)_3Br$, CTAB, 99%) for all materials synthesized. The metal salts: yttrium nitrate hexahydrate ($Y(NO_3)_3\cdot 6H_2O$, 99.8%), cerium sulfate ($Ce(SO_4)_2$) and tin chloride pentahydrate ($SnCl_4\cdot 5H_2O$, 98%) were used as metal sources for the modified MCM-41 synthesis. In the surfactant removal extraction, ammonium nitrate (NH_4NO_3, 99%) and methanol (CH_3OH, 99.9%) were used as the salt cation donor and the solvent, respectively. Hydrogen peroxide (H_2O_2, solution 30% w/w in water, Carlo Erba) and iron nitrate nonahydrate ($Fe(NO_3)_3\cdot 9H_2O$, 98%) were used for the oxidative degradation experiments of the surfactant. Deionized water obtained with a Milli-Q system (Millipore, Bedford, MA, USA) was used as the solvent for all synthesis.

3.2 Synthesis of Si–MCM-41, Sn–MCM-41, Y–MCM-41 and Ce–MCM-41 mesoporous materials by a conventional hydrothermal process

Two different samples of Sn–MCM-41 were prepared by direct incorporation of the metal into the synthesis gel following the methodology described by Gaydhankar and co-workers.[10] The synthesis procedure was as follows: 25 g of colloidal silica (Ludox AS-40) were slowly added to 49.93 g of TMAOH under magnetic stirring. To synthesize materials with molar ratios Si/Sn equal to 125 and 225, the right amount of $SnCl_4\cdot 5H_2O$ was dissolved in 5 ml of water and then added dropwise to the SiO_2–TMAOH dispersion and stirred for 1 h at 300 rpm. Then, 14.66 g of CTAB dissolved in 8.62 g of water and were slowly added to this solution and the mixture was stirred for 1 h at 600 rpm and transferred into a bath with ultrasound radiation (Ultrasonic Cleaner Branson 1510) where the formed gel remained under these conditions for 60 min. The final composition of the precursor gel was:

$SiO_2 : 0.008SnO_2 : 0.24CTAB : 0.30TMAOH : 25H_2O$

To prepare the Y–MCM-41 mesoporous material, the same methodology of Sn–MCM-41 was applied but the calculations were done to obtain 20 g of the final product (dry and detemplated siliceous based powder). The final composition of the precursor gel was:

$SiO_2 : 0.004Y_2O_3 : 0.24CTAB : 0.30TMAOH : 25H_2O$

For Ce–MCM-41 materials, the molar ratios synthesized were Si/Ce equal 50 and 225. Both samples were prepared according to the methodology reported elsewhere.[11] The synthesis was carried out when 2.85 g of CTAB were dissolved in 50 ml of deionized water and 50.75 ml of NH_4OH, 20%. After having stirred for 0.5 h, a second solution containing the required amount of $Ce(NO_3)_3\cdot 6H_2O$ diluted in 12.5 ml of deionized water was added. Then, 5.7 ml of tetraethylorthosilicate were added dropwise at 40 °C. Homogeneity was increased by transferring the gel to a bath with ultrasound radiation (Ultrasonic Cleaner Branson 1510) for 2.5 h and then aged at 500 rpm for another 4 h. The final composition of the precursor gel was (where $x = 50^{-1}$ or 225^{-1}):

$SiO_2 : xCeO_2 : 0.30CTAB : 10NH_4OH : 212H_2O$

For comparative studies Si–MCM-41 was synthesized following the same procedure of Ce–MCM-41 but without the addition of metal salt to the synthesis gel. The final composition was (where $x = 125^{-1}$ or 225^{-1}):

$SiO_2 : xSnO_2 : 0.24CTAB : 0.30TMAOH : 25H_2O$

The different synthesis gel precursors were hydrothermally treated in a Teflon-lined stainless steel reactor at 110 °C for 72 h for Sn– and Y–MCM-41 materials and 100 °C for 24 h in the cases of Ce– and Si–MCM-41. The process was carried out at autogenous pressure under static conditions. Finally, the precipitate was separated by centrifugation, washed with deionized water and dried at 80 °C overnight.

3.3 Surfactant removal procedure

3.3.1 Ultrasound-assisted ion exchange extraction in methanol (NH_4NO_3/US/MeOH surfactant extraction). The surfactant removal by low temperature NH_4NO_3/US/MeOH surfactant extraction was investigated using low frequency ultrasound energy. A typical experiment was performed using a sonicator Vibra cell sonics (VCX 750) with a frequency of 20 kHz and a tip diameter of 13 mm. To explore the effect on the metal modified structures, a response surface methodology was used to find the best conditions for the surfactant removal of Y–MCM-41 and these conditions were applied to the remaining structures. The Y–MCM-41 structure was chosen due to its high Si/Y molar ratio. A three factor Box–Behnken design was chosen with the following factors: x_1 = the salt cation donor concentration (NH_4NO_3), x_2 = the ultrasound amplitude and x_3 = the contact time. Table 6 shows the boundary values for the factors involved in the NH_4NO_3/US/MeOH surfactant extraction.

A typical run was carried out as follows: 0.5 g of the Y–MCM-41 material was loaded in a glass beaker containing the corresponding quantity of NH_4NO_3 dissolved in 80 ml of methanol.

Table 6 Box–Behnken design boundary values for the ultrasound assisted ion-exchange surfactant removal from metal modified MCM-41

	Boundary values		
Parameter[a]	−1	0	+1
x_1	0	25	50
x_2	22	40	60
x_3	5	10	15

[a] $[x_1] = \text{mM}$, $[x_2] = \%$, and $[x_3] = \text{min}$.

The baker was kept under ultrasound irradiation for the appropriate time, while the mixture was magnetically stirred at 300 rpm under adiabatic temperature. The product was recovered by centrifugation, washed with cold methanol and dried at 80 °C overnight.

3.3.2 Oxidative degradation: UV/MW, H_2O_2/UV/MW and Fe^{3+}/H_2O_2/UV/MW aqueous systems using a photochemical reactor. Alternative studies to the solvent extraction were done using the Sn–MCM-41 material as a comparison. For these experiments a photochemical reactor was used. In this reactor, ultraviolet and microwave energy are simultaneously applied to a liquid sample and it resulted in a very efficient and fast degradation of the organic molecules in diluted hydrogen peroxide aqueous solutions.[32] Three different approaches were investigated: (1) electromagnetic energy (UV/MW) irradiation, (2) diluted oxidative agent (400 ppm of H_2O_2) + UV/MW and (3) an iron salt concentration of 20 ppm and 400 ppm of H_2O_2 (the photo-Fenton system) + UV/MW. The experiments were carried out by loading 0.5 g of Sn–MCM-41 in 90 ml of MilliQ into the photoreactor. Then a microwave power of 50 W at 2.45 GHz was applied and the temperature increased to the boiling point. The dispersion was kept under reflux for 60 min after that the electromagnetic energy was switch off and the powder was separated by centrifugation, washed with water and dried at 80 °C overnight.

3.3.3 Calcination. The conventional calcination process was also used to remove the surfactant from the as-synthesized samples at high temperature. The dried powders were calcined using a 1 °C min^{-1} temperature heating rate to 550 °C and then maintaining it for 6 h under air atmosphere conditions.

3.4 Recovery and re-use of CTAB in a microwave hydrothermal synthesis of Si–MCM-41

The CTAB/methanol solution obtained after the surfactant removal process described in Section 3.3.1 was distilled until a minimal quantity of methanol remained in the flask bottom at 70 °C. The distilled methanol was recovered and saved for its re-use in future extractions. The remaining solution was evaporated at 40 °C until a white dry precipitated was obtained. The white powder was FTIR analysed and it showed identical adsorption bands than the CTAB reagent from Sigma-Aldrich (see Fig. 8a). A weighed quantity of the recovered CTAB was used without any other treatment to prepare a new Si–MCM-41 synthesis gel following the methodology described in Section 3.2. The hydrothermal process was microwave assisted using a high pressure microwave reactor with a microwave coaxial applicator described in a previous work.[33] After the aging process for 6 h at 50 °C the resultant gel was transferred into the Teflon vessel and loaded in the high pressure reactor. The microwave power was applied and the synthesis gel was kept under MW irradiation for 2 h under autogenous pressure and static conditions at 100 °C. The recovery of the Si–MCM-41, CTAB and methanol was once again carried out as mentioned above.

3.5 Characterization

3.5.1 Small angle X-ray scattering (SAXS). SAXS measurements for the as-synthesized, calcined and NH_4NO_3/US/MeOH surfactant extraction treated materials were carried out with a HECUS S3-MICRO camera (Kratky-type) equipped with a position-sensitive detector (OED 50M) containing 1024 channels of width 54 μm. Cu Kα radiation of wavelength $\lambda = 1.542$ Å was provided by an ultra-brilliant point micro-focus X-ray source (GENIX-Fox 3D, Xenocs, Grenoble), operating at a maximum power of 50 W (50 kV and 1 mA). The sample-to-detector distance was 281 mm. The volume between the sample and the detector was kept under vacuum during the measurements to minimize scattering from the air. The Kratky camera was calibrated in the small angle region using silver behenate ($d = 58.34$ Å).[34] Scattering curves were obtained in the q-range between 0.01 and 0.54 Å^{-1}, assuming that q is the scattering vector, $q = 4\pi/\lambda \sin\theta$, and 2θ is the scattering angle. Powder samples were placed into a 1 mm demountable cell having Nalophan foils as windows. The temperature was set to 25 °C and was controlled by a Peltier element, with an accuracy of 0.1 °C. All scattering curves were corrected for the empty cell contribution considering the relative transmission factor. The hexagonal unit cell is given as $a_0 = 2d_{100}/\sqrt{3}$.

3.5.2 FTIR spectroscopy. FTIR spectroscopy was used to determine the relative percent removal of the surfactant from the mesoporous structures. Quantitative analysis were done by measuring the area under the absorption peaks assigned to the vibrations of a surfactant molecule, pelleting the samples with KBr. Spectra were recorded in the range 4000–400 cm^{-1} using a Spectrum 100 FTIR spectrophotometer (PerkinElmer Inc., USA). The FTIR spectra were baseline-corrected and normalized at 1095 cm^{-1}. The percentage of surfactant removed (% removal) was calculated considering the total area of the synthesized M–MCM-41 material as 100%.

3.5.3 N_2 physisorption. Nitrogen adsorption/desorption isotherms were recorded at −196 °C using a Micromeritics ASAP 2010 instrument. The specific surface area (S_{BET}) was calculated using the BET method[35] and the external surface area (ESA) was calculated with the t-plot method.[36]

3.5.4 Thermogravimetric analysis (TGA). As comparative proof of template removal thermal gravimetric analysis were carried out using a TA Instruments Thermobalance model Q5000IR. Measurements were performed at a rate of 10 °C min^{-1}, from 40 °C to 600 °C under air flow (25 ml min^{-1}). The amount of sample in each TGA measurement varied between 2 and 4 mg.

3.5.5 Scanning electron microscopy (SEM). The morphology and particle size were analyzed using a SIGMA field emission scanning microscope (Carl Zeiss Microscopy GmbH, Germany) directly on uncoated samples. The reported images were acquired using the In-Lens Secondary Electron detector. The metal loaded into the framework was determined using energy-dispersive X-ray spectroscopy (EDS) that was performed by using a 10 mm^2 silicon drift detector (X-Act) coupled with the SEM microscope operated by the INCA software (Oxford Instruments). In this second case, the operative voltage of the electron source was about 20 kV and the working distance was 8.5 mm to maximize the X-ray photon counts.

3.5.6 ^{1}H MAS, ^{29}Si HPDEC MAS NMR. Solid state NMR spectroscopy studies were recorded using a Bruker Avance II 300 spectrometer.

^{1}H MAS NMR measurements were performed at a resonance frequency of 300 MHz. A 1.3 mm ZrO_2 rotor was spun at 50 kHz. A 4 μs flip angle was used (90°), and the recycling time was 3 s using a VF CPMAS H-X BB 1.3 mm probe.

^{29}Si HPDEC MAS NMR were acquired using a CPMAS H-X BB 4 mm probe at a resonance frequency of 59 MHz, and the recycling time was 10 s. A 4 μs flip angle was used (90°) with an acquisition time of 10 ms.

4 Conclusions

A novel methodology incorporating ultrasound irradiation into an ion-exchange approach was successfully applied to remove the surfactant from various metal modified mesoporous materials. The nature and amount of metal present in the MCM-41 structure proved to have a significant effect on the quantity of surfactant removed, ranging from 90% and up to 99% after 15 min of adiabatic treatment.

This methodology does not cause considerable textural nor structural differences in the final materials and reduces the thermal shrinkage produced by the conventional calcination surfactant degradation. The hexagonal structure was kept and high areas were obtained after the extraction treatment. Moreover, the surface silanol loss produced by high temperature surfactant removal can be lessened and more silanolic sites are preserved, making the design of specific materials very feasible, depending on the hydrophobic and hydrophilic characteristics desired. These materials could be potentially used in different applications, like catalytic supports or as matrices for absorption purposes.

It was proved that the removed surfactant can be recycled in the synthesis of a new mesoporous material, with clear advantages in terms of cost and CO_2 emission. The reduction of the environmental impact can also be reached through the use of innovative methodologies, such as the microwave-assisted synthesis.

We have shown that a synthesis performed with a recycled surfactant and microwave-irradiation has structural characteristics indistinguishable from those of the mesoporous material obtained with conventional synthesis.

The existent synergy between the methodologies used (US and MW irradiation) to assist the chemistry involved in the synthesis process can lead to promising scale up projections for the industrial production and application of these modified materials, without any technological barrier.

Acknowledgements

The authors wish to acknowledge the National Council of Science and Technology (CONACYT México, project CB-2010-158193) and the Consorzio per lo Sviluppo dei Sistemi a Grande Interfase (CSGI), for providing financial support. The authors would like to thank C. Lanza (INO-CNR), F. Pardini (INO-CNR) and Marco Vera (UAM-I) for their valuable technical support.

Notes and references

1 R. M. Martín-Aranda and J. Cejka, *Top. Catal.*, 2010, **53**, 141–153.
2 S. Bhattacharyya, G. Lelong and M. L. Saboungi, *J. Exp. Nanosci.*, 2006, **3**, 375–395.
3 B. Naik and N. N. Ghosh, *Recent Pat. Nanotechnol.*, 2009, **3**, 213–224.
4 C. T. Kresge, M. E. Leonowicz, W. J. Roth, J. C. Vartuli and J. S. Beck, *Nature*, 1992, **359**, 710–712.
5 A. Corma, A. Matinez, V. Martinezsoria and J. B. Monton, *J. Catal.*, 1995, **153**, 25–31.
6 M. Popova, Á. Szegedi, Z. Cherkezova-Zheleva, I. Mitov, N. Kostova and T. Tsoncheva, *J. Hazard. Mater.*, 2009, **168**, 226–232.
7 J. Felipe Díaz and K. J. Balkus Jr, *J. Mol. Catal. B: Enzym.*, 1996, **2**, 115–126.
8 H. P. Yiu, P. A. Wright and N. P. Botting, *J. Mol. Catal. B: Enzym.*, 2001, **15**, 81–92.
9 A. Corma, *Chem. Rev.*, 1997, **97**, 2373–2419.
10 T. R. Gaydhankar, P. N. Joshi, P. Kalita and R. Kumar, *J. Mol. Catal. A: Chem.*, 2007, **265**, 306–315.
11 J. C. Guevara, J. A. Wang, L. F. Chen, M. A. Valenzuela, P. Salas, A. García-Ruiz, J. A. Toledo, M. A. Cortes-Jácome, C. Angeles-Chavez and O. Novaro, *Int. J. Hydrogen Energy*, 2010, **35**, 3509–3521.
12 G. D. Mihai, V. Meynen, E. Beyers, M. Mertens, N. Bilba, P. Cool and E. F. Vansant, *J. Porous Mater.*, 2009, **16**, 109–118.
13 J. Patarin, *Angew. Chem., Int. Ed.*, 2004, **43**, 3878–3880.
14 J. He, X. Yang, D. G. Evans and X. Duan, *Mater. Chem. Phys.*, 2002, **77**, 270–275.
15 Y. Liu, Y. Pan, Z. Wang, P. Kuai and C. Liu, *Catal. Commun.*, 2010, **11**, 551–554.
16 A. Marcilla, M. Beltran, A. Gómez-Siurana, I. Martinez and D. Berenguer, *Chem. Eng. Res. Des.*, 2011, **89**, 2330–2343.
17 B. Tian, X. Liu, C. Yu, F. Gao, Q. Luo, S. Xie, B. Tu and D. Zhao, *Chem. Commun.*, 2002, 1186–1187.
18 L. López Pérez, M. J. Ortiz-Iniesta, Z. Zhang, I. Agirrezabal-Telleria, M. Santes, H. J. Heeres and I. Melián-Cabrera, *J. Mater. Chem. A*, 2013, **1**, 4747–4753.
19 S. Hitz and R. Prins, *J. Catal.*, 1997, **168**, 194–206.
20 N. Lang and A. Tuel, *Chem. Mater.*, 2004, **16**, 1961–1966.
21 S. Jabariyan and M. A. Zanjanchi, *Ultrason. Sonochem.*, 2013, **19**, 1087–1093.

22 Z. Huang, H. Miao, J. Li, J. Wei, S. Kawi and M. W. Lai, *Sep. Purif. Technol.*, 2013, **118**, 170–178.

23 J. S. Beck, J. C. Vartuli, W. J. Roth, M. E. Leonowicz, C. T. Kresge, K. D. Schmitt, C. T. W. Chu, D. H. Olson and E. W. Sheppard, *J. Am. Chem. Soc.*, 1992, **114**(27), 10834–10843.

24 J. M. Kim, J. H. Kwak, S. Jun and R. Ryoo, *J. Phys. Chem.*, 1995, **99**, 16742–16747.

25 Z. Zhang, J. Yin, H. J. Heeres and I. Melián-Cabrera, *Microporous Mesoporous Mater.*, 2013, **176**, 103–111.

26 S. P. Brown, *Solid State Nucl. Magn. Reson.*, 2012, **41**, 1–27.

27 M. Müller, G. Harvey and R. Prins, *Microporous Mesoporous Mater.*, 2000, **34**, 281–290.

28 D. W. Sindorf and G. E. Maciel, *J. Am. Chem. Soc.*, 1983, **105**(6), 1487–1493.

29 J. Trébosc, J. W. Wiench, S. Huh, V. S.-Y. Lin and M. Pruski, *J. Am. Chem. Soc.*, 2005, **127**(9), 3057–3068.

30 B. Grünberg, T. Emmler, E. Gedat, I. Shenderovich, G. H. Findenegg, H. H. Limbach and G. Buntkowsky, *Chem.–Eur. J.*, 2004, **10**, 5689–5696.

31 J. Walia, J. Crone, J. Liang, M. Niknam, C. Lemaire, R. T. Thompson and H. Peemoeller, *Solid State Nucl. Magn. Reson.*, 2013, **49–50**, 26–32.

32 C. Ferrari, I. Longo, E. Tombari and E. Bramanti, *J. Photochem. Photobiol., A*, 2009, **204**, 115–121.

33 J. González-Rivera, I. R. Galindo-Esquivel, M. Onor, E. Bramanti, I. Longo and C. Ferrari, *Green Chem.*, 2014, **165**(3), 1417–1425.

34 T. N. Blanton, M. Rajeswaran, P. W. Stephens, D. R. Whitcomb, S. T. Misture and J. A. Kaduk, *Powder Diffr.*, 2011, **26**, 313–320.

35 S. Brunauer, P. H. Emmett and E. Teller, *J. Am. Chem. Soc.*, 1938, **60**, 309.

36 B. C. Lippens, B. G. Linsen and J. H. de Boer, *J. Catal.*, 1964, **3**, 32.